

RECONSTRUCTION OF PARAMETRIC IMAGE MAPS IN SINGLE- AND MULTIPLE-COIL
FUNCTIONAL MAGNETIC RESONANCE IMAGING

Except where reference is made to the work of others, the work described in this dissertation is my own or was done in collaboration with my advisory committee. This dissertation does not include proprietary or classified information.

Weidong Tang

Certificate of Approval:

Thomas Denney
Professor
Electrical and Computer Engineering

Stanley Reeves, Chair
Professor
Electrical and Computer Engineering

Fa Dai
Professor
Electrical and Computer Engineering

George T. Flowers
Dean
Graduate School

RECONSTRUCTION OF PARAMETRIC IMAGE MAPS IN SINGLE- AND MULTIPLE-COIL
FUNCTIONAL MAGNETIC RESONANCE IMAGING

Weidong Tang

A Dissertation

Submitted to

the Graduate Faculty of

Auburn University

in Partial Fulfillment of the

Requirements for the

Degree of

Doctor of Philosophy

Auburn, Alabama
August 10, 2009

RECONSTRUCTION OF PARAMETRIC IMAGE MAPS IN SINGLE- AND MULTIPLE-COIL
FUNCTIONAL MAGNETIC RESONANCE IMAGING

Weidong Tang

Permission is granted to Auburn University to make copies of this dissertation at its discretion, upon the request of individuals or institutions and at their expense. The author reserves all publication rights.

Signature of Author

Date of Graduation

VITA

TANG Weidong was born to TANG Gongxian (唐功先) and YU Zaihui (于在惠) in Bengbu, Anhui Province, China (中国安徽省蚌埠市) on May 6, 1967. He received his Bachelor degree from Xidian University (西安电子科技大学) in July 1988 and Master degree from Tsinghua University (清华大学) in July 1993, respectively. He was with Chinese Academy of Sciences, Hughes Network Systems, and other companies. His research interests include medical imaging and signal processing, as well as software engineering.

DISSERTATION ABSTRACT
RECONSTRUCTION OF PARAMETRIC IMAGE MAPS IN SINGLE- AND MULTIPLE-COIL
FUNCTIONAL MAGNETIC RESONANCE IMAGING

Weidong Tang

Doctor of Philosophy, August 10, 2009
(M.S., Tsinghua University, Beijing, China, 1993)
(B.S., Xidian University, Xi'an, China, 1988)

103 Typed Pages

Directed by Stanley Reeves

Functional Magnetic Resonance Imaging (fMRI) is a standard tool to measure the hemodynamic response which is related to activation patterns in the human and animal brain. In conventional anatomical MRI, the decay and precession rates are regarded as sources of artifacts, but in applications such as functional MRI (fMRI), they are physiological quantities of interest. Single-shot parameter assessment by retrieval from signal encoding (SS-PARSE) acknowledges local decay and phase evolution in MRI, so it models each datum as a sample from (k, t) -space rather than k -space. Because local decay and frequency vary continuously in space, discrete models in space can cause artifacts in the reconstructed parameters. Increasing the resolution of the reconstructed parameters can more accurately capture the spatial variations, but the resolution is limited not only by computational complexity but also by the size of the acquired data. For a limited data set used for reconstruction, simply increasing the model resolution may cause the reconstruction to become an underdetermined problem. This dissertation presents a solution to this problem based on cubic convolution interpolation. Because the local decay and frequency are exponential time functions, FFTs can not be directly applied to the reconstruction

algorithm. A polynomial expansion is proposed so that FFTs can be used to accelerate reconstruction.

The second contribution of this dissertation is a new method to optimize the nonuniform FFT (NUFFT). This work was motivated by the nonuniform k -space trajectory in SS-PARSE. With the polynomial expansion, the cost function of the reconstruction of SS-PARSE is represented by a linear combination of 2-D Fourier transforms whose inputs are uniformly distributed data and outputs are nonuniformly distributed frequency responses. The gradient of the cost function in the reconstruction is also a linear combination of 2-D Fourier transforms whose inputs are nonuniformly distributed data on the frequency domain and outputs are functions on a 2-D nonuniform grid. FFTs can be applied to neither the cost function nor the gradients function because of the nonequally spaced inputs or outputs. In this dissertation, we focused on the 1-D Fourier transforms with uniform inputs and nonuniform outputs. The basic form of the optimization of the NUFFT is a nonlinear problem. In this dissertation, this nonlinear problem was reformulated to find the least-square solution of a linear problem. The computational accuracy of the NUFFT is also improved by the new method. The results can be easily extended to 2-D or the case with nonuniform inputs and uniform outputs.

After validating and testing these ideas with a single-coil MRI system, we extended the framework to parallel MRI systems, which have multiple receiving coils. Existing reconstruction methods estimate the maps of coil sensitivities by imaging “standard” objects. These convenient methods do not account for the change of coil sensitivities caused by the imaged objects. We propose a new algorithm that concurrently reconstructs the coil sensitivities along with magnitude, decay and field map. The core of this algorithm is the fast approach and the interpolation method we developed for SS-PARSE. From the simulation results, we observed significant improvement in the reconstruction accuracy of the decay function that is of the interest in fMRI.

ACKNOWLEDGMENTS

I would like to thank Dr. Stanley J. Reeves, my research advisor, for his guidance, help and leadership during my years in Auburn. He led me into the area of medical imaging. I also enjoyed and will miss our talks on sports, religion, and other technical and non-technical topics.

I would like to appreciate my committee members, Dr. Thomas Denney and Dr. Dai Fa, for their careful review and helpful suggestions on my dissertation. I would like to thank Dr. Amnon J. Meir for serving as the outsider reader.

I would like to thanks Dr. Donald B. Twieg at the University of Alabama at Birmingham.

This work was supported in part by the National Institute of Biomedical Imaging and Bioengineering (NIH), Grant No. EB 003292.

My thanks also go to my friends in Auburn.

Finally, I would like to thank my beloved parents using an ancient Chinese poem, *such kindness as young grass receives from the warm sun cannot be repaid*. 誰言寸草心，報得三春暉。

Two things are infinite: the universe and human stupidity; and I'm not sure about the universe.

Albert Einstein

War Eagle!

Style manual or journal used *Journal of Approximation Theory* (together with the style known as “*aums*”). Bibliography follows van Leunen’s *A Handbook for Scholars*.

Computer software used *The document preparation package* $\text{T}_{\text{E}}\text{X}$ (specifically $\text{L}_{\text{A}}\text{T}_{\text{E}}\text{X}$) together with the departmental style-file `aums.sty`.

TABLE OF CONTENTS

LIST OF FIGURES		xii
1	INTRODUCTION	1
1.1	Organization of the Thesis	2
1.2	A Brief History of MRI	2
1.3	MRI Model	3
1.3.1	Basic Concepts	3
1.3.2	The 1D Imaging and the Fourier Transform	4
1.3.3	Spatial Resolution in MRI	5
1.4	Relaxation and Field Inhomogeneity	6
1.5	Functional MRI (fMRI)	8
2	RECONSTRUCTION OF SS-PARSE	10
2.1	Introduction	10
2.2	Iterative Reconstruction Method	12
2.3	Interpolation	14
2.4	Fast Algorithm	20
2.4.1	Line Search	20
2.4.2	Approximations for Exponential Time Function	21
2.4.3	Implementation	25
2.5	Analysis of Accuracy of the Fast Algorithm	27
2.5.1	Reconstruction Error Introduced by the Approximation of Time Function	27
2.5.2	Reconstruction Error Introduced by k -Space Gridding	27
2.6	Experiments	30
2.6.1	Validation of Fast Approach	30
2.6.2	Noiseless Experiments	32
2.6.3	Noisy Experiment	35
2.6.4	Phantom and Animal Experiment	35
2.7	Conclusion	37
3	NONUNIFORM FAST FOURIER TRANSFORM (NUFFT)	42
3.1	Theory of NUFFT	42
3.1.1	Problem Statement	42
3.1.2	Basic Concepts	43
3.2	Least-Squares Optimization	45
3.3	Interpolations	48

3.4	Error Analysis of the Interpolation	53
3.5	Inverse Fourier Transform	53
3.6	Discussion	56
4	RECONSTRUCTION OF PARALLEL MRI	59
4.1	Introduction	59
4.2	Reconstruction	60
4.2.1	Extension of SS-PARSE	60
4.2.2	Initialization	61
4.2.3	Regularization	63
4.3	Simulation	64
4.3.1	Interpolation of Coil Sensitivity	64
4.3.2	Regularized Reconstruction	67
4.4	Human Experiment	71
4.5	Conclusion	75
5	CONCLUSION	80
5.1	Summary of the Contributions of this Thesis	80
5.2	Future Works	81
	BIBLIOGRAPHY	83
	APPENDIX A DERIVATION OF NRMSE OF NUFFT WITH LINEAR INTERPOLATION	87

LIST OF FIGURES

1.1	Two MRI trajectories.	5
1.2	Magnitude - Free induction decay (FID)	7
1.3	Spin Echo RF Sequence	8
1.4	Single-Shot MRI RF Sequence	8
2.1	Reconstructed $R_2^*(\text{sec}^{-1})$ from different methods. All images have 128×128 resolution 80-iteration reconstruction. For (a) and (b), interpolation factors are both 2, so the interpolation coefficients are 64×64 ; (c) is from a reconstruction with 128×128 resolution.	16
2.2	FWHM of cubic convolution and cubic spline. $\mathcal{C}(iC_{\text{conv}} - C_{\text{conv}})$ and $\mathcal{S}(iC_{\text{spline}} - C_{\text{spline}})$ were normalized to 1. The FWHM of cubic convolution is about 0.25cm and that of cubic spline is about 0.40cm. The results were from reconstructions with 80 iterations.	17
2.3	Cubic convolution interpolation function	18
2.4	Frequency responses of cubic convolution and spline interpolation	18
2.5	2-D cubic convolution interpolation function	19
2.6	Quadratic approximation of line search	22
2.7	Polynomial approximations of exponential time function for a pair of R and ω	24
2.8	Approximations of exponential time function.	25
2.9	Errors in Eq. (2.4) by approximation of time function	28
2.10	Errors in reconstructed images by approximation of time function	28
2.11	Errors in Eq. (2.4) by FFTs rounding	29
2.12	Errors in reconstructed images by FFTs rounding	29

2.13	A rosette trajectory	31
2.14	True and Reconstructed Images from Noiseless Experiments. All images are displayed with 128×128 resolution. We only reconstructed the pixels within the inscribed circle of the square. (a)(c)(e) are true images; (b)(d)(f) are from 64×64 reconstruction without interpolation, then interpolated to 128×128 images for display.	33
2.15	Reconstructed images from noiseless experiments. All images are displayed with 128×128 resolution. (a)(c)(e) are from 128×128 reconstruction without interpolation, (b)(d)(f) are images reconstructed from $2 \times$ cubic convolution interpolation, so the interpolation coefficients are 64×64	34
2.16	Images reconstructed from noisy signals. SNR is 40dB. All images have 128×128 resolution. (a)-(c) are from 64×64 reconstruction without interpolation, then interpolated to 128×128 images for display; (d)-(f) are from 128×128 reconstruction without interpolation, (g)-(i) are images reconstructed from $2 \times$ cubic convolution interpolation, so the interpolation coefficients are 64×64	36
2.17	Images reconstructed from phantom experiment. All images have 128×128 resolution and are masked to remove exterior artifactual features. (a)(c)(e) are from 64×64 reconstruction without interpolation, then interpolated to 128×128 images for display; (b)(d)(f) are images reconstructed from $2 \times$ cubic convolution interpolation, so the interpolation coefficients are 64×64	38
2.18	Images reconstructed from phantom experiment with larger frequency offset. All images have 128×128 resolution. (a)(c)(e) are from 64×64 reconstruction without interpolation, then interpolated to 128×128 images for display; (b)(d)(f) are images reconstructed from $2 \times$ cubic convolution interpolation, so the interpolation coefficients are 64×64 . Only the frequency map of the imaged object is shown in (e) and (f). The deliberately added frequency map is removed from these two figures. The artifactual features between the reconstruction mask (the inscribed circle of the square) and the imaged object remain, but they are not of interest.	39
2.19	Images reconstructed from monkey experiment. All images have 128×128 resolution. (a)(c)(e) are from 64×64 reconstruction without interpolation, then interpolated to 128×128 images for display; (b)(d)(f) are images reconstructed from $2 \times$ cubic convolution interpolation, so the interpolation coefficients are 64×64 . The R_2^* map in (c) was plotted with saturation of the values to maintain the same scale as (d) and so that the details of (d) would be visible.	40
3.1	Maximum Error	48
3.2	NRMS Error	49

3.3	Maximum Error	50
3.4	Linear Interpolation Kernel	51
3.5	Cubic Convolution Interpolation Kernel	52
3.6	NRMSE for different J and the number of precomputed frequencies for linear interpolation. In this figure, NRMSEs are plotted as the functions of J 's for different numbers of the precomputed frequencies. The "Exact" is the NRMSE for the precomputed frequencies. The "Exact" is the accuracy limit of the method stated in this chapter.	54
3.7	NRMSE for different J and the number of precomputed frequencies for linear interpolation. In this figure, NRMSEs are plotted as the functions of the numbers of the precomputed frequencies for different J 's.	55
3.8	NRMSE for different J and the number of precomputed frequencies for cubic convolution interpolation. In this figure, NRMSEs are plotted as the functions of J 's for different numbers of the precomputed frequencies. The "Exact" is the NRMSE for the precomputed frequencies. The "Exact" is the accuracy limit of the method stated in this chapter.	56
3.9	NRMSE for different J and the number of precomputed frequencies for cubic convolution interpolation. In this figure, NRMSEs are plotted as the functions of the numbers of the precomputed frequencies for different J 's.	57
3.10	Comparison of the performance of linear and cubic convolution interpolations. The "Exact" is the accuracy limit of the method stated in this chapter.	57
4.1	The magnitude, decay and field map used to synthesize simulation data. All images are displayed with 256×256 resolution. M_0 is normalized to 1.	65
4.2	The coil sensitivity maps used to synthesize simulation data. All images are displayed with 256×256 resolution. The unconstrained area in which M_0 is zero are displayed with zero. All maps are normalized to 1.	66
4.3	The coil sensitivity C_1 reconstructed from different interpolation factors. All images are displayed with 128×128 resolution. The artifacts in the unconstrained area in which M_0 is zero are removed. All maps are normalized to 1. No regularization is used.	68
4.4	The magnitude, decay and field map reconstructed from signals with 30dB SNR. All images are displayed with 128×128 resolution. The artifacts in the unconstrained area in which M_0 is zero are removed. M_0 is normalized to 1. No regularization is used.	69

4.5	The coil sensitivity maps reconstructed from signals with 30dB SNR. All images are displayed with 128×128 resolution. The artifacts in the unconstrained area in which M_0 is zero are removed. All maps are normalized to 1. No regularization is used.	70
4.6	The magnitude, decay and field map reconstructed from signals with 30dB SNR. The regularization parameters $\alpha = 5.5 \times 10^7$, $\gamma_R = 1.75 \times 10^8$ and $\gamma_I = 0$. All images are displayed with 128×128 resolution. The artifacts in the unconstrained area in which M_0 is zero are removed. M_0 is normalized to 1.	72
4.7	The coil sensitivity maps reconstructed from signals with 30dB SNR. The regularization parameters $\alpha = 1.09 \times 10^6$. All images are displayed with 128×128 resolution. The artifacts in the unconstrained area in which M_0 is zero are removed. All maps are normalized to 1.	73
4.8	Rosette trajectory used in human experiment. Only the first half of the trajectory is plotted.	74
4.9	The magnitude, decay and field map reconstructed from the human brain experiment. Cubic convolution interpolation was used to model the coil sensitivity. All images are displayed with 128×128 resolution. (a) (c) (e) are from $4\times$ interpolation for coil sensitivity. (b) (d) (f) are from $8\times$ interpolation for coil sensitivity. M_0 is normalized to 1. Most of the artifacts outside of the head were removed. No regularization was used.	76
4.10	The coil sensitivity maps reconstructed from the human brain experiment. Cubic convolution interpolation was used to model the coil sensitivity. All images are displayed with 128×128 resolution. (a) (c) are from $4\times$ interpolation. (b) (d) are from $8\times$ interpolation. Most of the artifacts outside of the head are removed. All maps are normalized to 1. No regularization was used.	77
4.11	The magnitude, decay and field map reconstructed from the human brain experiment. Cubic spline interpolation was used to model the coil sensitivity. All images are displayed with 128×128 resolution. (a) (c) (e) are from $4\times$ interpolation for coil sensitivity. (b) (d) (f) are from $8\times$ interpolation for coil sensitivity. Most of the artifacts outside of the head were removed. M_0 is normalized to 1. No regularization was used.	78
4.12	The coil sensitivity maps reconstructed from the human brain experiment. Cubic spline interpolation was used to model the coil sensitivity. All images are displayed with 128×128 resolution. (a) (c) are from $4\times$ interpolation. (b) (d) are from $8\times$ interpolation. Most of the artifacts outside of the head were removed. All maps are normalized to 1. No regularization was used.	79

CHAPTER 1

INTRODUCTION

Magnetic resonance imaging (MRI), which is also called nuclear magnetic resonance imaging (NRMI) or spin imaging, is an important application of the theory of nuclear magnetic resonance (NMR). MRI may also be the most important development of the medical diagnostic imaging since Wilhelm Röntgen's X-ray. Its medical applications have revolutionized clinical diagnosis. In the last several decades, six scientists were awarded Nobel Prizes in three different disciplines (physics, chemistry, and physiology or medicine) for their works related to MRI.

In an MRI experiment, the nuclear magnetization of hydrogen atoms in water in human or animal body are aligned by a powerful external magnetic field. After the aligned magnetization of the hydrogen nuclei is tipped by a radiofrequency (RF) wave, a gyromagnetic field is generated. The gyromagnetic field is captured by the signal receiving coils. The received signal is interpreted as the spatial-frequency response of the imaged object, so Fourier analysis is a fundamental tool in image reconstruction.

MRI is non-invasive and non-ionizing. MRI is superior to computerized tomography (CT) in soft-tissue imaging, such as neurological (brain), musculoskeletal, cardiovascular, and oncological imaging. Abundant diagnostic information is provided by changing the parameters of a MRI system.

With the development of hardware and computing technologies, functional magnetic resonance imaging (fMRI) is becoming a standard procedure with useful applications in patients management [1]. fMRI is interested in hemodynamic responses, which reflect the neural activities in the brains or spinal cords of humans or animals.

Blood Oxygenation Level Dependent (BOLD) fMRI was introduced by Ogawa [2] and Kwong [3]. The change of neural activity in a region of the brain causes the changes in

blood oxygenation. The changes, called the BOLD effect, can be detected by magnetic resonance imaging (MRI). The BOLD effect is the basis for almost all fMRI experiments to map patterns of activation in the working human brain [1].

Because the BOLD produces some physical effects that are omitted in conventional MRI models, the classical reconstruction methods based on Fourier transforms must be changed to accommodate aspects of fMRI, such as long readout time and nonuniform k -space trajectories.

1.1 Organization of the Thesis

In this chapter, we briefly review the history and basic principles of MR imaging.

In Chapter 2, we detail the major problem — the reconstruction of single-shot parameter assessment by retrieval from signal encoding (SS-PARSE). A new iterative reconstruction methods based on a more accurate physical model is developed. After reviewing some similar works, we focus on two issues: quality improvement and a fast algorithm.

In Chapter 3, implementation of an FFT with nonuniform sampling, in the reconstruction is investigated.

In Chapter 4, we extend concepts stated in Chapters 2 and 3 to parallel imaging.

Chapter 5 concludes the thesis. The innovative ideas are summarized, and possible future work is discussed.

1.2 A Brief History of MRI

In the 1930's, Isidor Rabi investigated the relationship between nuclei, magnetic field and external RF. In 1944, his work was awarded the Nobel Prize in physics “for his resonance method for recording the magnetic properties of atomic nuclei”.

In 1946, Felix Bloch [4] and Edward Purcell [5] laid the physical foundation of MRI. They independently observed the phenomenon of NMR. They also theoretically explained the experiments. They were awarded the Nobel Prize “for their development of new methods

for nuclear magnetic precision measurements and discoveries in connection therewith” in 1952.

From 1950 to 1970, the major developments of NMR were in chemical and physical molecular analysis.

In 1971, Raymond Damadian [6] successfully used NMR to discriminate malignant tissue from normal tissue in a rat by measuring relaxation times of the different tissues.

In 1973, in a paper that almost was not published [7], Paul Lauterbur illustrated the internal structure of a clam acquired by MRI. The door to medical applications of MRI was opened. In the same decade, Peter Mansfield mathematically analyzed the RF signals of MRI and developed a method for fast imaging. Lauterbur and Mansfield shared the 2003 Nobel Prize in physiology or medicine “for their discoveries concerning magnetic resonance imaging”.

1.3 MRI Model

1.3.1 Basic Concepts

Spin, a quantum mechanical property, can interact with an external magnetic field \mathbf{B}_0 . The nuclei, which have an odd number of protons or neutrons, have a non-zero spin or magnetic moment. Without an external magnetic field, the randomly oriented spin angular momentum cannot be detected. When an external magnetic field B_0 is applied, M_0 , the magnetic moment along the external field direction, is generated [8]:

$$M_0 = \frac{\rho_0 \gamma^2 \hbar^2}{4kT} B_0 \quad (1.1)$$

where ρ_0 is the spin density, γ is a constant called the gyromagnetic ratio, $\hbar \triangleq h/(2\pi)$ in terms of Planck’s quantum constant h , k is the Boltzmann constant, and T is the absolute temperature. This magnetic moment vector precesses around the external field direction

with an angular frequency called the Larmor frequency given by

$$\omega_0 = \gamma B_0 \quad (1.2)$$

1.3.2 The 1D Imaging and the Fourier Transform

In order to have a detectable signal, a radio-frequency (RF) magnetic field is applied for a short time to make the magnetic field that is produced by the aggregate proton spins precess along with the magnetization. This precession generates a changing flux in a nearby coil. The changing flux is a signal modulated at the Larmor frequency ω_0 . After demodulation, the received signal is given by [8]

$$s(t) = \int \rho(x) e^{i\phi_G(x,t)} dx \quad (1.3)$$

where $\phi_G(x,t) = -\gamma x \int_0^t G(\tau) d\tau$, and the $G(t)$ is the gradient in the z -direction. This signal is called *free induction decay* (FID).

Let

$$k(t) = \frac{\gamma}{2\pi} \int_0^t G(\tau) d\tau \quad (1.4)$$

where $k(t)$ is called the k -trajectory [9], which samples the spatial-frequency domain. Then (1.3) can be written as

$$s(t) = \int \rho(x) e^{-i2\pi k(t)x} dx \quad (1.5)$$

(1.5) shows that the signal $s(t)$ is related to the spin density of the sample $\rho(x)$ by a Fourier transform. This is the foundation of the reconstruction of conventional MRI. Two k -space trajectories are illustrated in Figure 1.1.

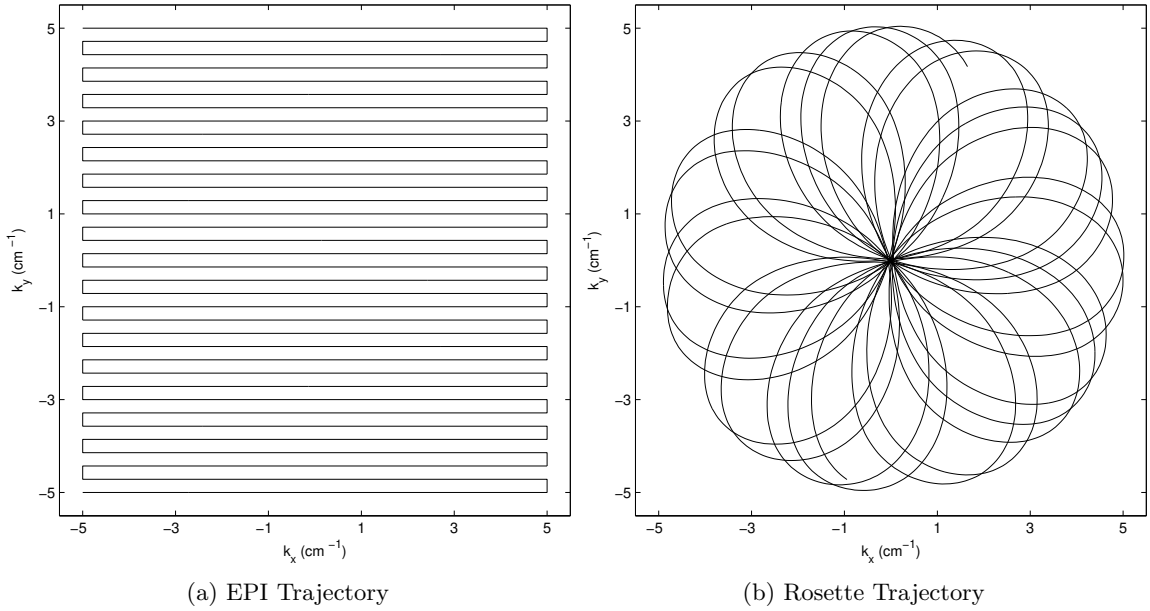


Figure 1.1: Two MRI trajectories.

The concept of 1D imaging can be extended to multi-dimensional Fourier imaging.

$$s(t) = \int \rho(\mathbf{r}) e^{-i2\pi\mathbf{k}(t)\cdot\mathbf{r}} d\mathbf{r} \quad (1.6)$$

where \mathbf{r} is a multi-dimensional vector. In this case, t controls the values of the vector of $\mathbf{k}(t)$, which correspond to the frequency-domain coordinates of the Fourier transform. Thus, the signal $s(t)$ can be interpreted as a sample of the Fourier transform of $\rho(\mathbf{r})$ at the frequency coordinate $\mathbf{k}(t)$. In this way, a one-dimensional signal can sweep through an n -dimensional space.

1.3.3 Spatial Resolution in MRI

Limited readout time in MRI applications restricts the number of collected samples, the number of phase encodings and the coverage of k -space. The inversion problem based on partially covered k -space is called a *limited-Fourier inversion* problem [8]. In the discrete

case, the 1D image $\rho(x)$ is reconstructed by

$$\rho(x) = \Delta k \sum_{n=0}^{N-1} s(n) e^{-i2\pi n \Delta k x} \quad (1.7)$$

where Δk is the k -space sampling interval. The total width of k -space coverage is $W = N\Delta k$. Let L be the size of the field of view (FOV). To avoid aliasing, the Nyquist criterion must be met

$$\Delta k = \frac{1}{L} \leq \frac{1}{A} \quad (1.8)$$

where A is the physical size of the original image.

From (1.7), we have

$$s(n) = \sum_{k=0}^{N-1} \rho(k) e^{-i2\pi n k \Delta x} \quad (1.9)$$

where Δx is the spatial resolution, the smallest size that can be measured for a given object:

$$\Delta x = \frac{L}{N} = \frac{1}{N\Delta k} = \frac{1}{W} \quad (1.10)$$

1.4 Relaxation and Field Inhomogeneity

In an MRI experiment, after the RF pulse is turned off, the longitudinal magnetization field begins to exponentially recover with a time constant T_1 , the *longitudinal relaxation time*. T_1 is also called *thermal* or *spin-lattice relaxation time*.

T_2 is the exponential decay rate of the FID for an ideal MR experiment. T_2 is also known as *transverse relaxation*. Because of static magnetic field inhomogeneities, an observed FID decays with an exponential constant T_2^* that is smaller than T_2 .

In soft tissues, the typical T_1 is about 1 second. T_2 and T_2^* are at the level of milliseconds. For most biological tissues, T_1 values are typically 5 to 10 times longer than T_2 values [10].

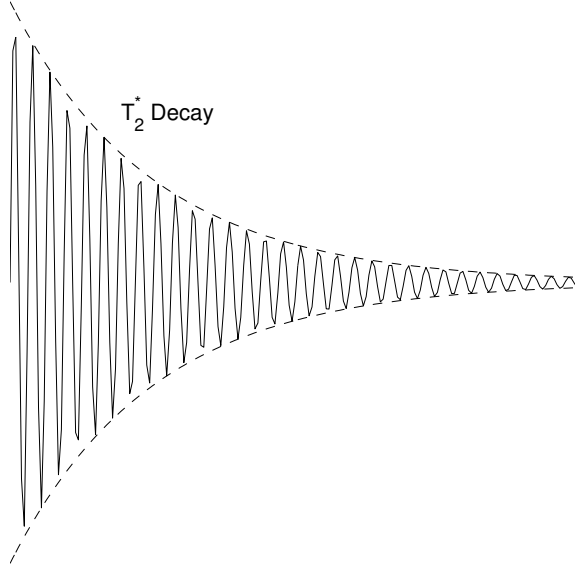


Figure 1.2: Magnitude - Free induction decay (FID)

The spin density and T_1 and T_2^* among different tissues are the basis of the MRI contrast mechanism. Because the T_2^* relaxation rate of blood depends on whether or not the hemoglobin is bound with oxygen, the T_2^* map as a function of space is of interest in fMRI. The BOLD contrast is also described by R_2^* , the reciprocal of T_2^* .

The magnetic field inhomogeneity also causes phase changes in the observed signal. In Chapter 2, we will model the relaxation and field inhomogeneity by revising the (1.6) [11]:

$$s(t) = \int \rho(\mathbf{r}) e^{-(R_2^*(\mathbf{r}) + i\omega(\mathbf{r}))t} e^{-i2\pi\mathbf{k}(t)\cdot\mathbf{r}} d\mathbf{r} \quad (1.11)$$

Conventional methods to estimate R_2^* and ω are all based on multi-shot MRI. In traditional MRI, R_2^* and ω can also be compensated by manipulating the RF sequence (see Figure 1.3). Since the readout time is short, it is not necessary to model R_2^* and ω . Single-shot MRI needs a long readout time (see Figure 1.4), so the decay and phase precession can not be omitted any more. [11] suggested an iterative method for single-shot MRI. We will review this method in Chapter 2.

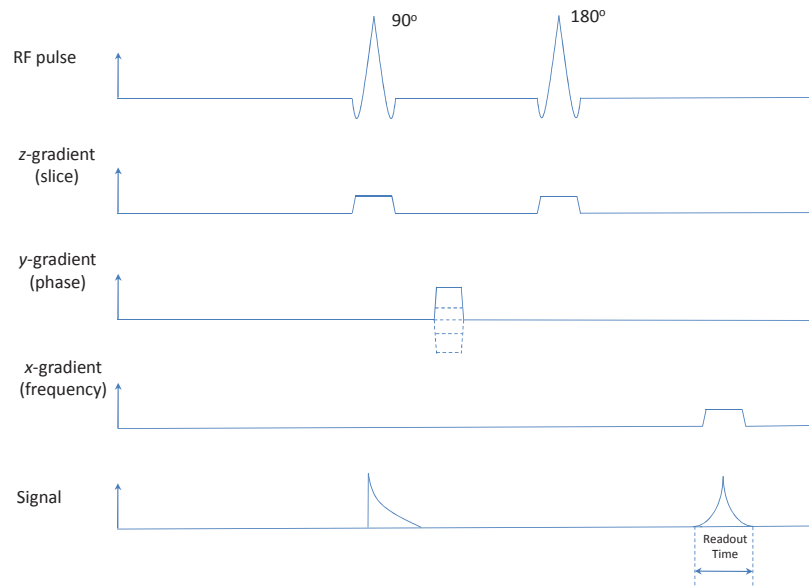


Figure 1.3: Spin Echo RF Sequence

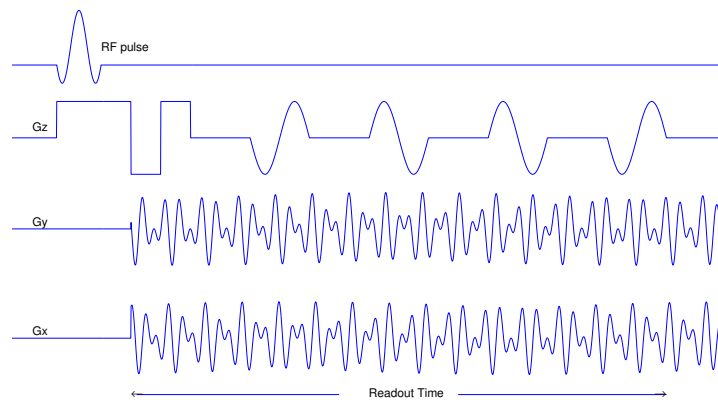


Figure 1.4: Single-Shot MRI RF Sequence

1.5 Functional MRI (fMRI)

For many years, it has been known that the functions of the human brain are controlled by different areas of the cerebral cortex. Several modalities are successful in mapping brain functions onto related laminae. Positron emission tomography (PET) detects brain activities by measuring regional cerebral blood flow (rCBF). Magnetoencephalography (MEG)

and electroencephalography (EEG) detect the magnetic or electronic signal generated by the activated brain, but they can hardly locate which areas the signal is from. fMRI is a noninvasive modality that efficiently maps brain function.

Before the late 1980's, the imperfections caused by T_2^* were regarded as a negative factor in MRI. The technique of spin echo can be used to refocus the RF pulse and compensate T_2^* relaxation. Another method is to shorten the interval between the excitation RF pulse and the signal sampling.

Later, it was recognized that the paramagnetic material in blood can be used to mark blood vessels and generate effective contrast. Because deoxyhemoglobin is more paramagnetic than oxyhemoglobin (oxyhemoglobin is more diamagnetic than deoxyhemoglobin), deoxyhemoglobin is magnetically susceptible. This means that an oxygen intensity change can cause a change in the MRI signal, making deoxyhemoglobin a natural contrast agent.

Because the consumption of oxygen reflects brain activities, one can map brain function by analyzing an MRI signal. The goal of fMRI is to detect brain activation with sensory, motor and cognitive processes.

CHAPTER 2

RECONSTRUCTION OF SS-PARSE

Single-shot parameter assessment by retrieval from signal encoding (SS-PARSE) acknowledges local decay and phase evolution in MRI, so it models each datum as a sample from (k, t) -space rather than k -space. Because local decay and frequency vary continuously in space, discrete models in space can cause artifacts in the reconstructed parameters. Increasing the resolution of the reconstructed parameters can more accurately capture the spatial variations, but the resolution is limited not only by computational complexity but also by the size of the acquired data. For a limited data set used for reconstruction, simply increasing the model resolution may cause the reconstruction to become an underdetermined problem. In this chapter, we present a solution to this problem based on cubic convolution interpolation. Because the local decay and frequency are exponential time functions, FFTs can not be directly applied to the reconstruction algorithm. A polynomial expansion is proposed so that FFTs can be used to accelerate reconstruction. Results on simulated data and phantoms demonstrate reduced computation time and improved quality.

2.1 Introduction

Twieg [9] and Ljunggren [12] introduced the k -space formalism to unify different MRI techniques. Based on this formalism, the observed MRI signal $s(t)$ is the Fourier transform of local transverse magnetization $M(\mathbf{x})$:

$$s(t) = \int M(\mathbf{x})e^{i\mathbf{k}(t)\cdot\mathbf{x}}d\mathbf{x} + \varepsilon(t) \quad (2.1)$$

where $s(t)$ is the observed MRI signal, i is $\sqrt{-1}$, $M(\mathbf{x})$ is local transverse magnetization at location \mathbf{x} , and $\varepsilon(t)$ is white complex Gaussian noise. The last factor in the integrand

represents the spatial phase modulation imposed by the imaging gradients at time t :

$$\mathbf{k}(t) = \gamma \int_0^t \mathbf{G}(t') dt' \quad (2.2)$$

The advantage of this model is that $M(\mathbf{x})$ can be reconstructed from $s(t)$ by a Fourier transform when $s(t)$ is appropriately rearranged, but it is physically inaccurate, especially for long readout MRI. The premise of this model is that local decay and phase evolution are insignificant; that is, local transverse magnetization does not change during the signal acquisition. For long readout time, magnitude, decay and phase-angle precession of local transverse magnetization is inevitable.

In conventional anatomical MRI, the decay and precession rates are regarded as sources of contrast, but in applications such as functional MRI (fMRI), they are physiological quantities of interest [13, 14]. fMRI measures signal changes caused by neural activity in the brain or spinal cord of humans or other animals. So fMRI is interested in a series of images or — more precisely — a single evolving image, not a single *static* image as in conventional MRI methodology. SS-PARSE recognizes this reality and uses a more accurate model [11]:

$$s(t) = \int M_0(\mathbf{x}) e^{-[R_2^*(\mathbf{x}) + i\omega(\mathbf{x})]t} e^{i\mathbf{k}(t) \cdot \mathbf{x}} d\mathbf{x} + \varepsilon(t) \quad (2.3)$$

where $M_0(\mathbf{x})$ is the local transverse magnetization immediately following excitation, $R_2^*(\mathbf{x})$ is the local net relaxation rate, and $\omega(\mathbf{x})$ is the local frequency offset.

Many methods to acquire proper signals to reconstruct some combination of M_0 , R_2^* and ω have been proposed [15–20]. [21, 22] suggested time-segmentation and frequency-segmentation to accelerate the reconstruction of local magnitude in the presence of frequency offset; [23] estimated ω from multi-scan MRI; [24, 25] jointly reconstructed R_2^* and ω ; [26] recovered M_0 and ω_0 in the presence of R_2^* . All of these methods require multiple scans or echoes and none of them jointly estimate all three terms of M_0 , R_2^* and ω .

In this chapter, we address the following three issues in the reconstruction algorithm of SS-PARSE after reviewing the iterative reconstruction method.

- how to implement a higher-resolution reconstruction.
- how to do an efficient line search in the iterative reconstruction algorithm.
- how to interpret this nonlinear problem of SS-PARSE in terms of Fourier transforms.

2.2 Iterative Reconstruction Method

The discrete version of (2.3) on the spatial (x, y) grid indexed by i is given by

$$s_n = \underbrace{\sum_i M_{0i} e^{nW_i} e^{i\mathbf{k}_n \cdot \mathbf{x}_i}}_{\hat{s}_n(\mathbf{M}_0, \mathbf{W})} + \varepsilon_n \quad (2.4)$$

where $W_i = -[R_{2i}^* + i\omega_i] \Delta t$, $\mathbf{k}_n = \mathbf{k}(n\Delta t)$, and Δt is the sampling interval. Our goal is to reconstruct \mathbf{M}_0 , \mathbf{W} from the observed signal \mathbf{s} by solving (2.4).

For traditional MRI, local transverse magnetization in (2.1) can be reconstructed by taking the inverse Fourier transform of an appropriately formatted version of $s(t)$ because the trajectory $\mathbf{k}(t)$ samples the frequency domain of *one image* $M(\mathbf{x})$. SS-PARSE is different; its trajectory samples the frequency domains of *different images* that are related by an exponential time function $e^{n\mathbf{W}}$. Because the problem is now nonlinear and does not have the structure of an FFT, one must use an iterative method to solve this problem [27]. We propose to use an iterative conjugate-gradients (CG) algorithm to minimize the cost function:

$$J(\mathbf{z}) = \sum_n |s_n - \hat{s}_n(\mathbf{z})|^2 + R(\mathbf{z}) \quad (2.5)$$

with respect to \mathbf{z} , where $\mathbf{z} = \{\mathbf{M}_0, \mathbf{W}\}$, and $R(\mathbf{z})$ is a regularization term. In the following discussion, we omit the regularization term for simplicity, though the method easily incorporates such a term if desired.

The CG algorithm used to reconstruct \mathbf{z} is initialized as follows [28]:

Initialization

- Set $\mathbf{z} = \mathbf{z}_0$
- Steepest descent: $\Delta\mathbf{z}_0 = -\nabla_{\mathbf{z}}J(\mathbf{z}_0)$
- Line search: $\alpha_0 = \underset{\alpha \geq 0}{\operatorname{argmin}}J(\mathbf{z} + \alpha\Delta\mathbf{z}_0)$
- $\mathbf{z}_1 = \mathbf{z}_0 + \alpha\Delta\mathbf{z}_0$

After the first iteration, the following steps constitute one iteration of moving along subsequent conjugate direction $\wedge\mathbf{z}_n$, where $\wedge\mathbf{z}_0 = \Delta\mathbf{z}_0$:

1. $\Delta\mathbf{z}_n = -\nabla_{\mathbf{z}}J(\mathbf{z}_n)$
2. $\beta_n = (\Delta\mathbf{z}_n^T \Delta\mathbf{z}_n) / (\Delta\mathbf{z}_{n-1}^T \Delta\mathbf{z}_{n-1})$
3. $\wedge\mathbf{z}_n = \mathbf{z}_n + \beta_n \wedge\mathbf{z}_{n-1}$
4. $\alpha_n = \underset{\alpha \geq 0}{\operatorname{argmin}}J(\mathbf{z}_n + \alpha \wedge\mathbf{z}_n)$
5. $\mathbf{z}_{n+1} = \mathbf{z}_n + \alpha_n \wedge\mathbf{z}_n$

The gradients $\nabla_{\mathbf{z}}J$ computations include two parts:

$$\frac{\partial J}{\partial \mathbf{M}_0} = \sum_{n=1}^N f_n e^{n\mathbf{W}} e^{j\mathbf{k}_n \cdot \mathbf{x}} \quad (2.6)$$

$$\frac{\partial J}{\partial \mathbf{W}} = \mathbf{M}_0 \sum_{n=1}^N n f_n e^{n\mathbf{W}} e^{j\mathbf{k}_n \cdot \mathbf{x}} \quad (2.7)$$

where $f_n = [\hat{s}_n - s_n]^*$ and N denotes the length of s_n .

There are three problems with this method:

- Because local decay and frequency vary continuously in space, discrete models in space can cause artifacts in the reconstructed parameters. Increasing the resolution of the reconstructed parameters can more accurately capture the spatial variations, but the resolution is limited not only by computational complexity but also by the size of the acquired data. For a limited data set used for reconstruction, simply increasing the resolution may cause the reconstruction to become an underdetermined problem.

- Directly evaluating $J(\mathbf{z})$ and $\nabla_{\mathbf{z}}J(\mathbf{z})$ is computationally intensive.
- An accurate line search requires several evaluations of $J(\mathbf{z})$.

2.3 Interpolation

The iterative reconstruction method cannot be used to reconstruct images with arbitrary resolution. The degrees of freedom of this reconstruction depends on the resolution of \mathbf{z} , so limited acquired data limits the resolution of the reconstruction. We propose a solution based on cubic convolution interpolation. Instead of estimating images, this algorithm computes interpolation coefficients that are used to generate images on a higher-resolution grid, so the reconstruction algorithm is still a fully determined or overdetermined problem.

Interpolation is an efficient bridge between different resolutions in a discrete representation. In order to reconstruct images on a high-resolution grid while keeping the reconstruction algorithm determined or over-determined, we estimate interpolation coefficients rather than parameter set \mathbf{z} , the parameter images to be reconstructed.

There are several candidates for the interpolation. Cubic splines are very popular in applications because of their minimum curvature property [29]. When we applied cubic splines to this problem, however, we observed residual blurring in local decay and frequency. To explain this behavior, we resort to a simplified linearized model. By using splines, we are actually solving a problem corresponding to something like $\mathbf{y} = A\mathbf{x}$, where A is a lowpass filter. The character of A makes the reconstruction problem harder, because A is not well conditioned. Conjugate-gradients has no problem with this in the linear case. The conjugate directions can still cover the space quickly and reconstruct the unknown \mathbf{x} . In the nonlinear case, the presence of the A matrix exaggerates the effect of nonlinearity. In a nonlinear problem, A changes from iteration to iteration, which changes the relationship of the conjugate directions from iteration to iteration. Thus, the nonlinear local decay/frequency term will converge more slowly than the linear magnitude term. Without an inordinate number of iterations, the estimated decay/frequency parameters would be blurred in comparison to

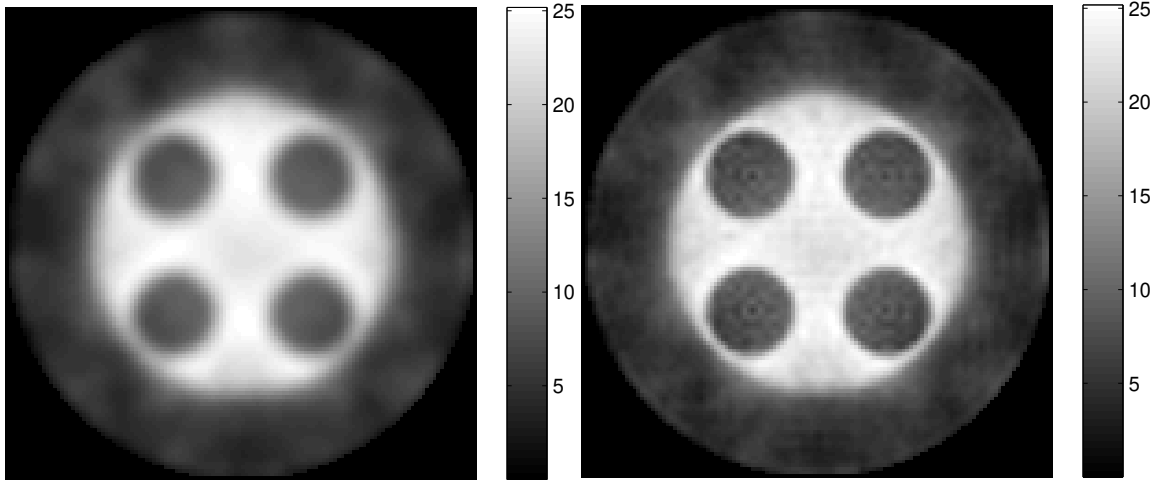
the magnitude term. The cubic convolution interpolator is different from the cubic splines interpolator [30]. It passes through zero at neighboring sample locations, so it does not have to invert a system of equations to match the sample values to the coefficients. We found that this interpolator yields significantly less blurred results with the same number of iterations. This difference is illustrated in Figure 2.1, where we compared the R_2^* reconstructed from cubic spline interpolation, cubic convolution spline, and non-interpolation.

In order to quantify the different blurring of cubic convolution and cubic spline interpolations and to further justify our choice of cubic convolution, we designed a special experiment to approximate the point-spread function (PSF) for this nonlinear problem. First, we noiselessly synthesized $s(t)$ of (2.3) with constant M_0 , R_2^* and ω . Then we reconstructed the three parameter sets with cubic convolution and cubic splines with 80 iterations. Because of the interpolations, we actually estimated the interpolation coefficients rather than M_0 , R_2^* and ω . The reconstructed coefficients for R_2^* by cubic convolution and cubic spline are denoted by C_{conv} and C_{spline} . The value of R_2^* within a small circle (diameter 1/128 of FOV, which is $12.8 \times 12.8\text{cm}^2$) at the origin was changed to a different constant value, and then a new $s(t)$ was noiselessly synthesized based on the changed parameter sets. The reconstructed coefficients for R_2^* from the new $s(t)$ by cubic convolution and cubic splines are denoted by iC_{conv} and iC_{spline} . Let \mathcal{C} be the cubic convolution interpolation operator and \mathcal{S} be the cubic spline interpolation operator. The central lines of $\mathcal{C}(iC_{\text{conv}} - C_{\text{conv}})$ and $\mathcal{S}(iC_{\text{spline}} - C_{\text{spline}})$ are shown in Figure 2.2. The FWHM is noticeably smaller for cubic convolution interpolation.

If sampled data are equally spaced, interpolation functions can be written as:

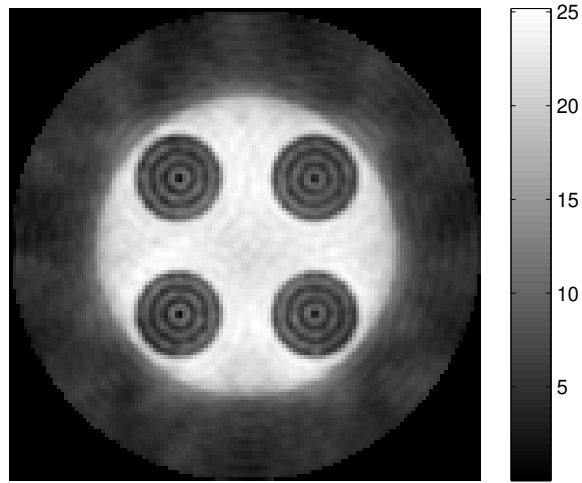
$$g(x) = \sum_k c_k u\left(\frac{x - x_k}{h}\right) \quad (2.8)$$

where c_k is an interpolation coefficient that is a function of the sampled data, x_k is the k th interpolation node, h is the sampling interval, and $u(x)$ is an interpolation kernel. The sampled function $f(x)$ agrees with $g(x)$ at every x_k . Cubic convolution interpolation



(a) Cubic Spline

(b) Cubic Convolution



(c) Non-Interpolation

Figure 2.1: Reconstructed $R_2^*(\text{sec}^{-1})$ from different methods. All images have 128×128 resolution 80-iteration reconstruction. For (a) and (b), interpolation factors are both 2, so the interpolation coefficients are 64×64 ; (c) is from a reconstruction with 128×128 resolution.

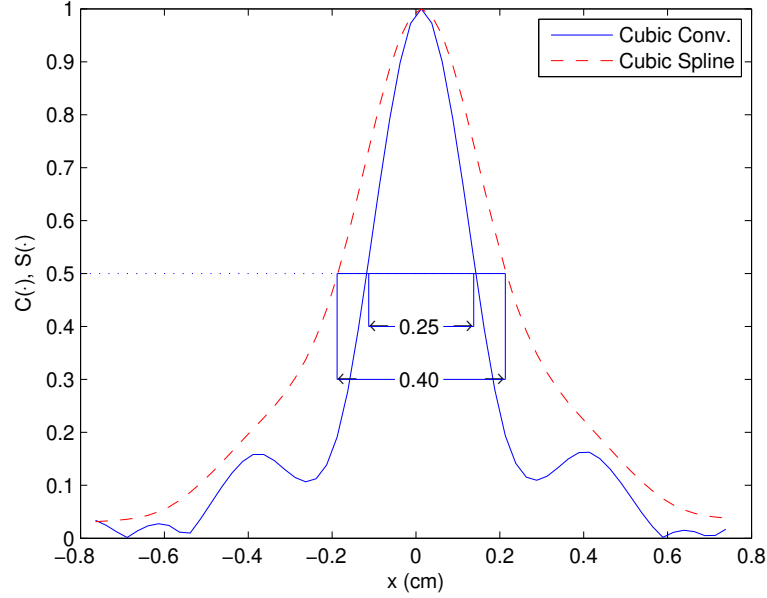


Figure 2.2: FWHM of cubic convolution and cubic spline. $\mathcal{C}(iC_{\text{conv}} - C_{\text{conv}})$ and $\mathcal{S}(iC_{\text{spline}} - C_{\text{spline}})$ were normalized to 1. The FWHM of cubic convolution is about 0.25cm and that of cubic spline is about 0.40cm. The results were from reconstructions with 80 iterations.

assumes that $g(x)$ agrees with $f(x)$ for the first four terms of the Taylor series expansion.

The 1-D continuous interpolation kernel function is written as:

$$u(x) = \begin{cases} \frac{4}{3}|x|^3 - \frac{7}{3}|x|^2 + 1 & 0 \leq |x| < 1 \\ -\frac{7}{12}|x|^3 + 3|x|^2 - \frac{59}{12}|x| + \frac{5}{2} & 1 \leq |x| < 2 \\ \frac{1}{12}|x|^3 - \frac{2}{3}|x|^2 + \frac{7}{4}|x| - \frac{3}{2} & 2 \leq |x| < 3 \\ 0 & 3 \leq |x| \end{cases} \quad (2.9)$$

This function is shown in Figure 2.3. If the sampling interval $h = 1/2$, the vector form of $u(x)$ is $\mathbf{u} = \{1/96, 0, -3/32, 0, 7/32, 1, 7/32, 0, -3/32, 0, 1/96\}$.

The comparison of the frequency response of the cubic convolution interpolator and the cubic splines interpolator is shown in Figure 2.4. The high-frequency response of the cubic convolution interpolation is higher than that of the cubic splines interpolation. This helps explain why the former one gives less blurred results.

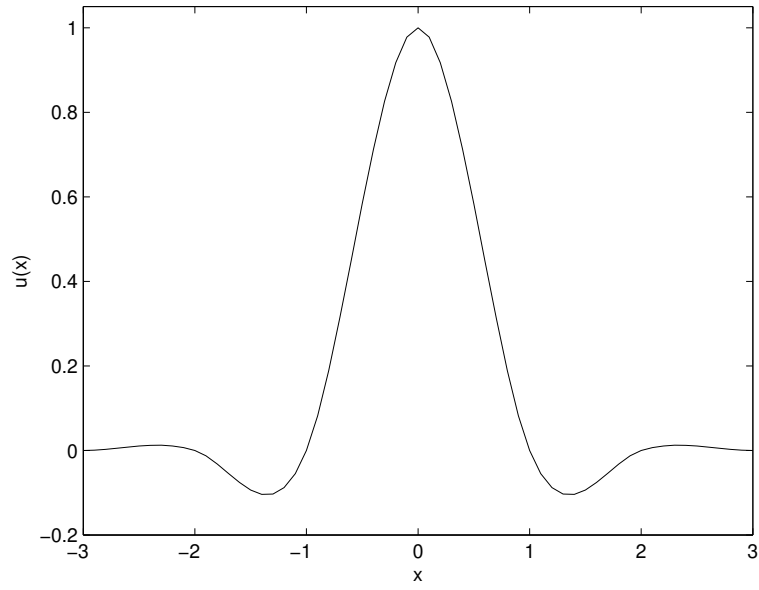


Figure 2.3: Cubic convolution interpolation function

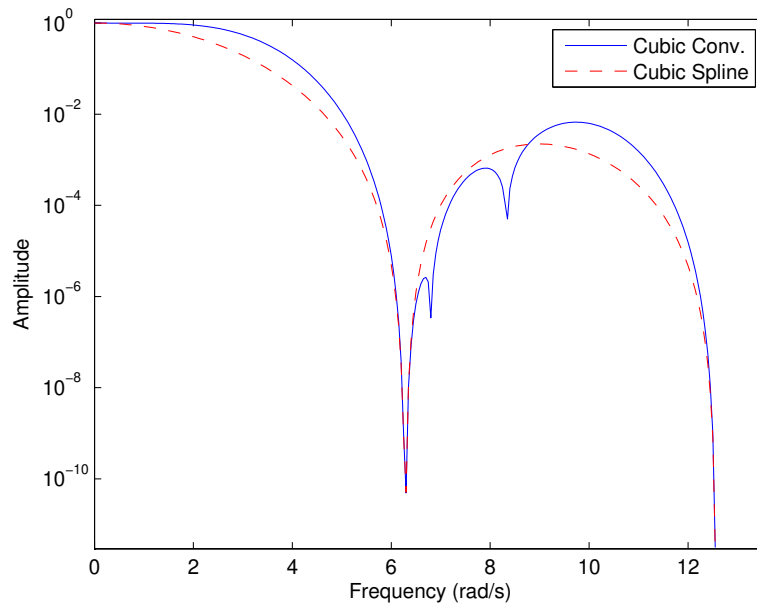


Figure 2.4: Frequency responses of cubic convolution and spline interpolation

For the reconstruction of SS-PARSE, we use 2-D interpolation. The continuous 2-D interpolation function is shown in Figure 2.5. For 2-D interpolation, we first apply

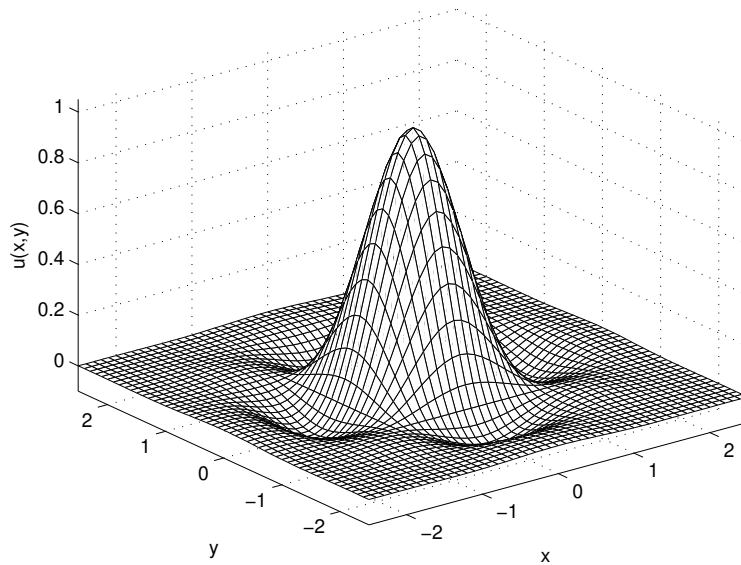


Figure 2.5: 2-D cubic convolution interpolation function

interpolation for all rows in a 2-D matrix. Then we apply the same procedure to the columns of the interpolated matrix. This process can be written with matrix multiplications:

$$\mathbf{z} = \mathbf{A}^T \mathbf{C} \mathbf{A} \quad (2.10)$$

where \mathbf{C} is the coefficient matrix formatted as an image array, \mathbf{z} is an $NM \times NM$ matrix, M is an integer not less than 2, and \mathbf{A} is an $N \times NM$ sparse matrix constructed from $u(x)$. The element a_{mn} in \mathbf{A} is computed by

$$a_{mn} = u \left(1 + \frac{n-1}{M} - m \right) \quad (2.11)$$

for the interpolation kernel in (2.9).

The key step to compute cost function (2.5) is the evaluation of (2.4). For the interpolation method, this step is straightforward. First, we compute \mathbf{z} using (2.10). Then we compute the cost function. The computation of gradient matrix $\partial J / \partial \mathbf{C}$ includes two parts.

One is the computation of $\partial J/\partial \mathbf{z}$, and the other is the computation of $\partial \mathbf{z}/\partial \mathbf{C}$:

$$\begin{aligned}\nabla_{\mathbf{C}} J &= \nabla_{\mathbf{z}} J \cdot \frac{\partial \mathbf{z}}{\partial \mathbf{C}} = \nabla_{\mathbf{z}} J \cdot (\mathbf{A}^T \mathbf{A}) \\ &= \nabla_{\mathbf{z}} J * (\mathbf{u}^T \mathbf{u})\end{aligned}\tag{2.12}$$

where $\mathbf{u} = [u(-3+h) \ u(-3+2h) \ \dots \ u(3-h)]$. Since $\mathbf{u}^T \mathbf{u}$ is a small matrix, we directly compute this convolution.

2.4 Fast Algorithm

We implemented the previously discussed algorithm with MATLAB on a Linux workstation. The non-interpolation version took about 160 seconds to reach a given accuracy with 64×64 resolution. The interpolation method was also tested. The interpolation factor is 2, so the computational complexity of the interpolation is more than four times that of the non-interpolation algorithm, taking about 900 seconds. The approximation of the line search described below has already been incorporated into the algorithm. So further speedups are highly desired. We propose an efficient line search approximation and then an acceleration based on FFT-based approximation.

2.4.1 Line Search

Line search is critical to the speed and accuracy of the CG algorithm; an efficient method is suggested to address this problem.

To invert a non-quadratic function using the CG algorithm, line search is used to compute α , the adjustable step length. The line search is computationally intensive for this reconstruction algorithm because each line search evaluates (2.4) several times. We numerically analyzed the function of $J(\alpha)$ and found that the quadratic approximation can be used to reduce the computational complexity of the line search [31]. The method of

quadratic approximation is described as follows.

$$J(\mathbf{z} + \alpha \nabla J) \approx J''(0)\alpha^2 + J'(0)\alpha + J(\mathbf{z}) \quad (2.13)$$

$$\alpha_{\min} = -\frac{J'(0)}{2J''(0)} \quad (2.14)$$

where

$$J'(0) \approx \frac{J(\mathbf{z} + \delta \nabla J) - J(\mathbf{z} - \delta \nabla J)}{2\delta} \quad (2.15)$$

$$J'(\pm\delta/2) \approx \frac{J(\mathbf{z} \pm \delta \nabla J) - J(\mathbf{z})}{\pm\delta} \quad (2.16)$$

$$J''(0) \approx \frac{J'(\delta/2) - J'(-\delta/2)}{\delta} \quad (2.17)$$

where δ is a small positive scalar. Since $J(\mathbf{z})$ has been computed in the previous iteration, one only needs to evaluate $J(\mathbf{z} + \delta \nabla J)$ and $J(\mathbf{z} - \delta \nabla J)$ to minimize $J(\mathbf{z} + \alpha \nabla J)$ with respect to α . From Figure 2.6, we can see $J(\alpha)$ is consistently very close to a quadratic function over the range of interest. As a fail-safe, the value of $J(\mathbf{z} + \alpha_{\min} \nabla J)$ can be compared to $J(\mathbf{z})$. If the value of $J(\mathbf{z} + \alpha_{\min} \nabla J) > J(\mathbf{z})$, this indicates a nonquadratic cost in the current step. In those unusual cases, a full line search can then be performed to find the minimizer. If that happens, the conjugate direction needs to be reinitialized to the negative gradient, since this indicates a nonquadratic region.

2.4.2 Approximations for Exponential Time Function

Conventional MRI samples the frequency domain of an image assumed to be static, so FFTs can be directly used to reconstruct the image. Because of the exponential time function $e^{n\mathbf{W}}$, SS-PARSE samples the frequency domains of *different* images that are related by the exponential discrete time function. In order to use FFTs, we must separate the time variable n from local decay and frequency \mathbf{W} .

Frequency and time segmentations were proposed in [22] to address the problematic exponential time function so that FFTs can be used to accelerate the reconstruction process.

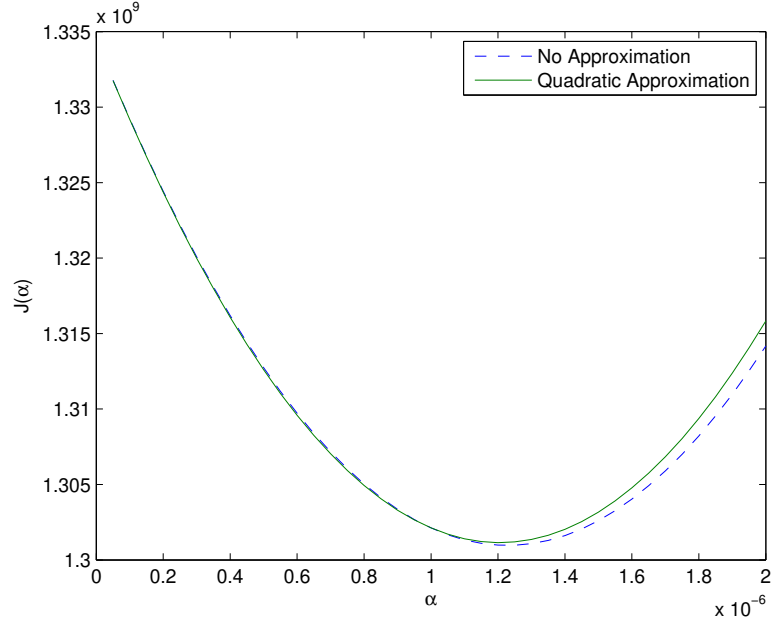


Figure 2.6: Quadratic approximation of line search

However, this method is inconvenient for simultaneous estimation of magnitude, decay and frequency. We use a polynomial approximation of the exponential time function to reduce computation time [31].

According to [22], all of the known approximations are special cases of the following general form:

$$e^{n\mathbf{W}} \approx \sum_{l=0}^{L-1} a_l(n) C_l(\mathbf{W}) \quad n = 1, \dots, N \quad (2.18)$$

where C_l denotes basis functions, and a_l denotes coefficients. The authors of [22] suggested the approximations of time segmentation and frequency segmentation. Both segmentations are efficient in the absence of decay ($\text{Re}\{\mathbf{W}\} = \mathbf{0}$), and the coefficients are only determined by the histogram of $\text{Im}\{\mathbf{W}\}$. Unfortunately, neither requirement is satisfied in SS-PARSE reconstruction. Coefficients of an efficient approximation should not be changed, since updating the coefficients requires intensive computations. Assuming $\text{Re}\{\mathbf{W}\} = \mathbf{0}$ and

the values of \mathbf{W} are histogrammed into K bins, the computation of a_l with LS time-segmentation approach is $O(LK(N + L) + L^3N)$ [22] in addition to the histogramming computation. Since $\text{Re}\{\mathbf{W}\} \neq \mathbf{0}$ in SS-PARSE, the computation is more complicated.

A reasonable assumption is that \mathbf{R} and $\boldsymbol{\omega}$ are bounded within a known range. Based on this assumption, one can approximate the exponential time function with polynomials whose coefficients will not be changed through the estimation process. Using the polynomial approximation, (2.18) is written as:

$$e^{n\mathbf{W}} \approx \sum_{l=0}^{L-1} a_l n^l \mathbf{W}^l \quad n = 1, \dots, N \quad (2.19)$$

The advantage of polynomial functions is that the functions of \mathbf{n} used to separate \mathbf{n} from \mathbf{W} are analytically defined and easily evaluated. Experiments show that the minimum value of L necessary for a good approximation is determined by $N|\omega|_{\max}\Delta t$, since local decays are relatively small compared to frequencies. Because of this feature, the maximum frequency range dominates the error and should be made as small as possible. Thus, polynomial approximations can be defined to cover half of the range of frequency. Let:

$$\omega_0 = \frac{1}{2}(\omega_{\max} + \omega_{\min}) \Delta t \quad (2.20)$$

$$\mathbf{Z}(l) = \begin{cases} a_l (\mathbf{W} - i\omega_0)^l, & \text{Im}\{\mathbf{W} - i\omega_0\} \geq 0 \\ a_l^* (\mathbf{W} + i\omega_0)^l, & \text{Im}\{\mathbf{W} - i\omega_0\} < 0 \end{cases} \quad (2.21)$$

(2.19) can then be rewritten as:

$$e^{n\mathbf{W}} \approx e^{in\omega_0} \sum_{l=0}^{L-1} n^l \mathbf{Z}(l) \quad (2.22)$$

The direct choice of the coefficients a_l of this approximation is a Taylor series, but the convergence speed of the Taylor expansion is too slow. We used an LS method to choose a_l . This optimization process can be written in matrix form. \mathbf{x} is an $M \times 1$ vector

with $\text{Im}\{\mathbf{x}\} \in [0, N|\omega|_{max}\Delta t]$ and $\text{Re}\{\mathbf{x}\}$ less than some real number; \mathbf{a} is an $L \times 1$ vector composed of a_i ; \mathbf{X} is an $M \times L$ matrix whose i th column is \mathbf{x}^{i-1} . We consider the real and imaginary parts of \mathbf{x} to be uniformly likely over their assumed range and choose \mathbf{X} to represent this uniform weighting. As long as the number of samples (rows of \mathbf{X}) is relatively large compared to the polynomial order, the exact sample spacing and density have negligible impact on the solution. \mathbf{a} is solved by:

$$\underset{\mathbf{a}}{\text{argmin}} \frac{1}{2} \|e^{\mathbf{x}} - \mathbf{X}\mathbf{a}\|_2^2 \quad (2.23)$$

Figure 2.7 shows the precision of the real parts of the polynomial approximation for a specific pair of R and ω . The normalized root mean square error (NRMSE) ε of this

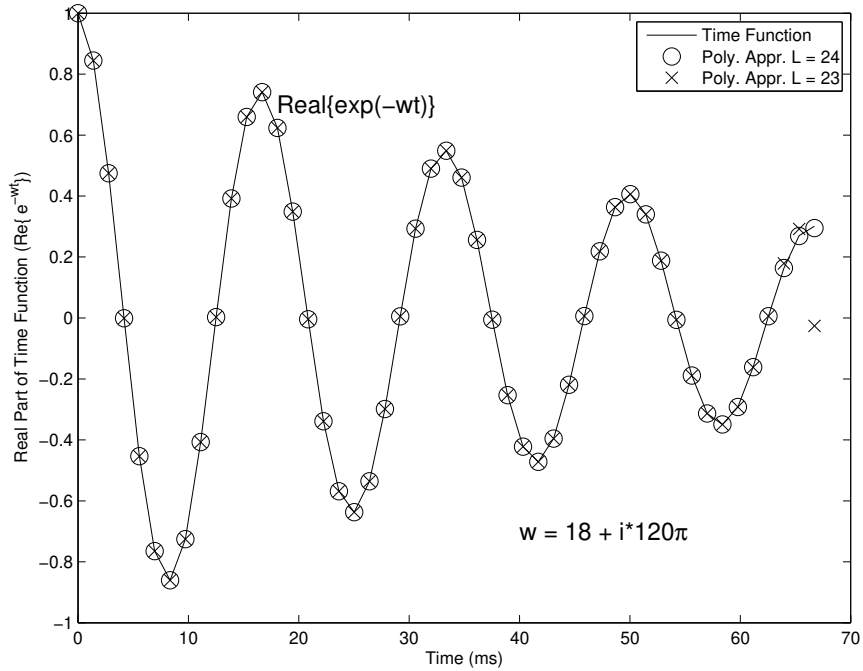


Figure 2.7: Polynomial approximations of exponential time function for a pair of R and ω

approximation is defined as:

$$\varepsilon = \sqrt{\frac{A+B}{C}} \quad (2.24)$$

where

$$A = \int_0^{y_{\max}} \int_0^{x_{\max}} \left| e^{-x-iy} - \sum_{l=0}^{L-1} a_l (x + iy)^l \right|^2 dx dy$$

$$B = \int_{y_{\min}}^0 \int_0^{x_{\max}} \left| e^{-x-iy} - \sum_{l=0}^{L-1} a_l^* (x + iy)^l \right|^2 dx dy$$

$$C = \int_{y_{\min}}^{y_{\max}} \int_0^{x_{\max}} |e^{-x-iy}|^2 dx dy$$

The NRMSE is shown in Figure 2.8.

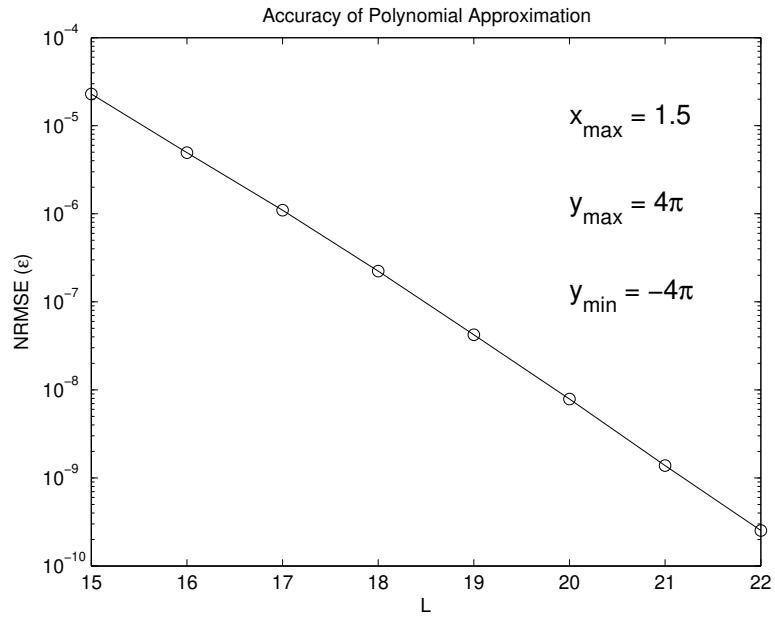


Figure 2.8: Approximations of exponential time function.

2.4.3 Implementation

Polynomial approximation allows us to separate the time variables from the variables of local decay and frequency in the exponential time function. Inserting (2.22) into (2.4)

leads to:

$$\hat{s}_n \approx e^{m\omega_0} \sum_{l=0}^{L-1} n^l \sum_{i=1}^K M_{0i} Z_i(l) e^{i\mathbf{k}_n \cdot \mathbf{x}(i)} \quad (2.25)$$

By discretizing \mathbf{k}_n into an integer grid, we can compute the inside summation of (2.25) with an FFT, and \mathbf{s} is approximated with a linear combination of a relatively small number of FFTs.

There are two ways to compute $\nabla_{\mathbf{z}} J$. One is to compute the derivatives and then apply an approximation. The other one is to apply an approximation and then compute the derivatives. Both methods lead to identical formulas in this case.

$$\frac{\partial J}{\partial \mathbf{M}_0} \approx \sum_{l=0}^{L-1} \mathbf{Z}(l) \sum_{n=1}^N f_n e^{m\omega_0} n^l e^{i\mathbf{k}_n \cdot \mathbf{x}} \quad (2.26)$$

$$\frac{\partial J}{\partial \mathbf{W}} \approx \mathbf{M}_0 \sum_{l=1}^L \mathbf{Z}(l) \sum_{n=1}^N f_n e^{m\omega_0} n^l e^{i\mathbf{k}_n \cdot \mathbf{x}} \quad (2.27)$$

where $f_n = (\hat{s}_n - s_n)^*$ and N denotes the length of $s(n)$. The inside summations of (2.26) and (2.27) can also be evaluated by FFTs.

If the sizes of reconstructed M_0 and W are all $K \times K$, direct evaluations of (2.4), (2.6) and (2.7) require $O(NK^2)$ arithmetic operations. If \mathbf{k}_n is discretized into a grid of $mK \times mK$, it requires $O(Lm^2K^2 \log_2 m^2K^2)$ arithmetic operations.

Even a small deviation in the approximated gradient relative to the actual gradient could theoretically have a huge impact on the final results. It is hard to analytically characterize this effect. We numerically analyzed this deviation in Section 2.6.1 and the results show that the errors in the final results caused by approximations have a negligible impact on the estimation results.

2.5 Analysis of Accuracy of the Fast Algorithm

There are two sources of errors introduced by our algorithm. One is the approximation of the time function; the other is the k -space gridding, rounding the non-equispaced trajectory into an equispaced grid. We use normalized root mean square (*NRMS*) to describe the accuracy. If $\hat{\mathbf{x}}$ is the estimation of a row vector \mathbf{x} , the *NRMS* is defined as:

$$NRMS = \left[\frac{(\hat{\mathbf{x}} - \mathbf{x})(\hat{\mathbf{x}} - \mathbf{x})'}{\mathbf{x}\mathbf{x}'} \right]^{1/2} \quad (2.28)$$

2.5.1 Reconstruction Error Introduced by the Approximation of Time Function

Another error in the fast algorithm is from the approximation of the exponential time function. In order to find the error caused only by polynomial approximation, we do not round the non-equally spaced k -space trajectory into an integer grid. We compare the results of polynomial approximation with the results of the non-approximation method using the standard conjugate gradient algorithm. Figure 2.10 shows the NRMS error of the FID. In the NRMS computations, \mathbf{x} is the estimated FID from the non-approximated algorithm, and $\hat{\mathbf{x}}$ is the estimated FID from the polynomial approximation method. We also computed the NRMS errors of reconstructed images. In the computations, \mathbf{x} is the image reconstructed by the non-approximated method, and the $\hat{\mathbf{x}}$ is the image reconstructed from the polynomial approximation.

2.5.2 Reconstruction Error Introduced by k -Space Gridding

In order to use FFTs, one approach is to round the non-equally spaced k -space trajectory to an equally spaced grid. This will cause errors in reconstruction. We first study the error in (2.4). We compare the results by mapping the k -space trajectory into equally spaced grids with that of directly computing (2.4). The result is shown in Figure 2.11. The reconstruction used 64×64 resolution. If the FFT factor is m , the k -space trajectory is

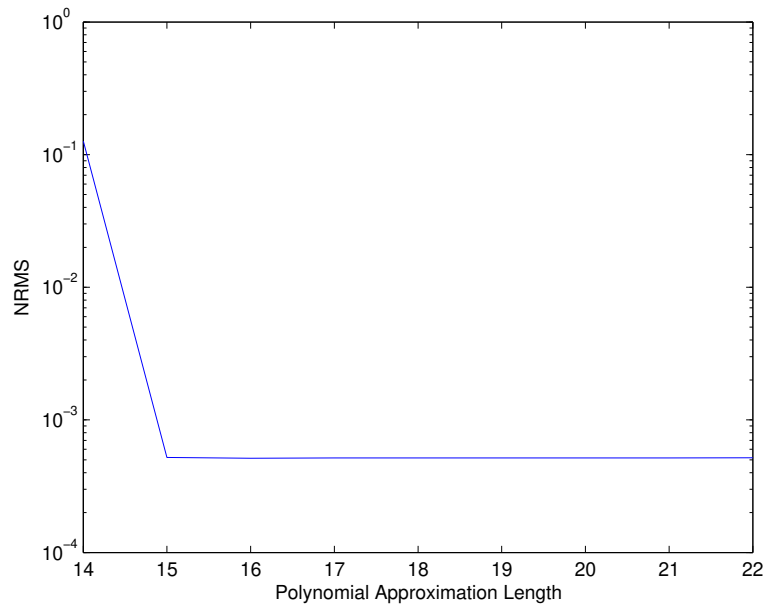


Figure 2.9: Errors in Eq. (2.4) by approximation of time function

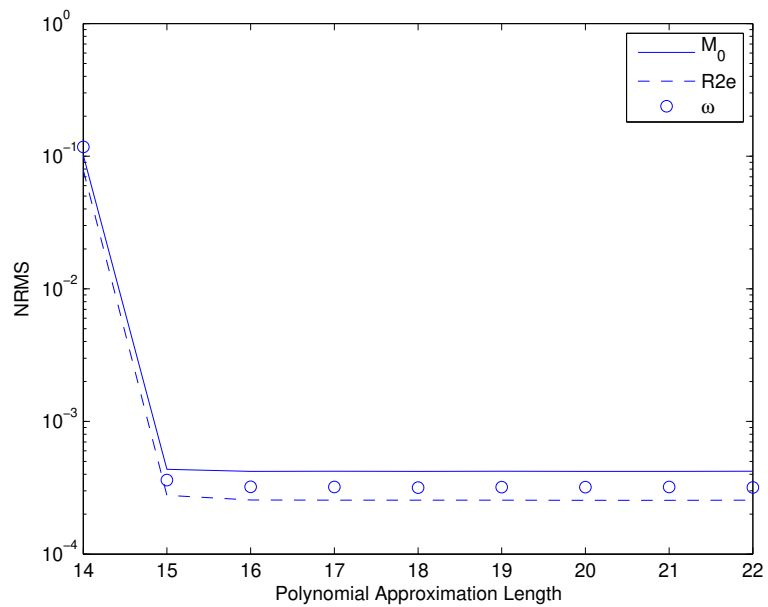


Figure 2.10: Errors in reconstructed images by approximation of time function

mapped into a $64m \times 64m$ equally spaced grid. The errors in the reconstructed images are shown in Figure 2.12.

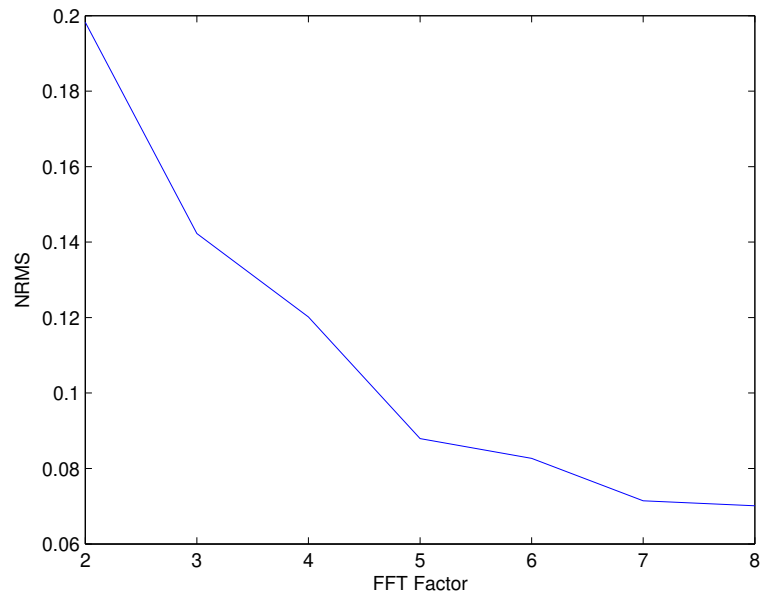


Figure 2.11: Errors in Eq. (2.4) by FFTs rounding

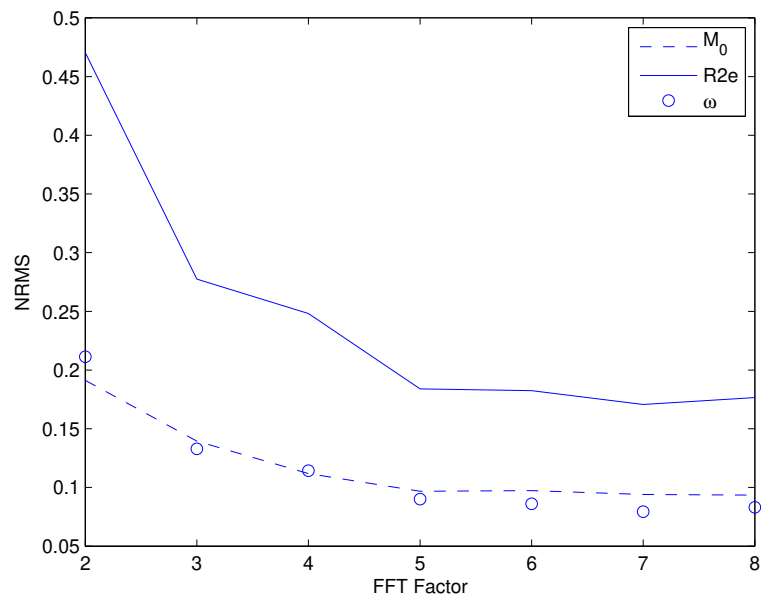


Figure 2.12: Errors in reconstructed images by FFTs rounding

Because the error caused by k -space gridding is the dominant part of the approximation error, we propose to use the nonuniform FFT (NUFFT) instead of k -space gridding. The NUFFT will be detailed in the next chapter.

2.6 Experiments

In this section, we validated the fast approach and the cubic convolution reconstruction algorithm using synthetic data. A rosette trajectory was used to synthesize data. The readout time was 66.7ms, and the FOV was 12.8cm. The sampling interval was $5.56\mu\text{s}$, so the length of $s(n)$ in (2.4) was 12,000 samples. To simulate a continuous spatial domain, the data was synthesized from images with resolution 1024×1024 . We used analytical functions of $M_0(\mathbf{x})$, $R_0^*(\mathbf{x})$ and $\omega(\mathbf{x})$ to generate the 1024×1024 images that were used to approximate a continuous spatial domain. All the reconstructed images in this paper have 64×64 or 128×128 resolution. In order to compare the reconstructed images with the “true” images, we used the same analytical functions to generate “true” images with 64×64 or 128×128 images.

According to [32], the rosette trajectories can be modeled by:

$$\mathbf{k}(t) = k_{\max} \cos(\omega_1 t) e^{i\omega_2 t} \quad (2.29)$$

where $\mathbf{k}(t) = k_x(t) + jk_y(t)$. A rosette trajectory with $k_{\max} = 2.819$, $\omega_1 = 5171.4\text{s}^{-1}$ and $\omega_2 = -3334.8\text{s}^{-1}$ is shown in Figure 2.13.

2.6.1 Validation of Fast Approach

The SS-PARSE reconstruction was implemented in MATLAB on a Dell Optiplex 745 equipped with a 2.66GHz Core 2 CPU and 3GB RAM, and Windows XP. We compared two cases: 1) 64×64 resolution and 2) 64×64 interpolation coefficients with $2 \times$ cubic convolution interpolation (computational complexity roughly equivalent to 128×128 resolution). For each case, the length of $s(t)$ was 12,000. The computation times per iteration are given in Table 2.1.

We have shown that polynomial expansion of the time function along with the NUFFT can greatly speed up the reconstruction. Since this approach involves approximations, we need to demonstrate that the reconstructions from the fast approach have no significant

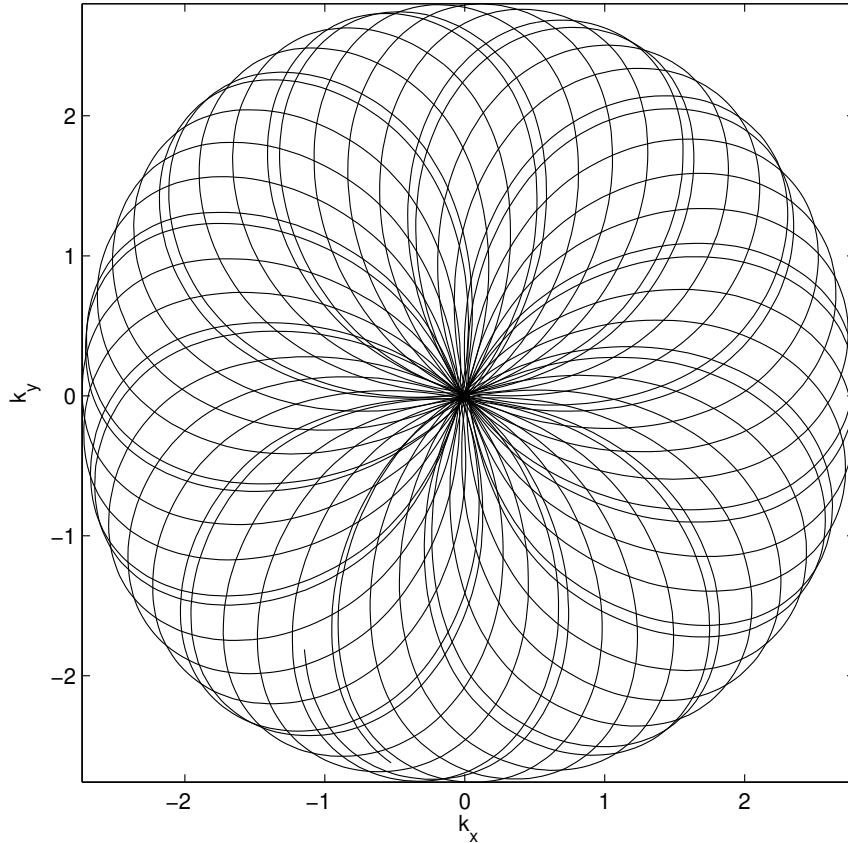


Figure 2.13: A rosette trajectory

Table 2.1: Computer Times (in seconds per iteration)

Reso.	Fast	
	NO	YES
64	5.37	0.64
2x	20.56	1.18

differences from that of the unaccelerated method. We used noiseless free induction decay (FID) signals to compare the results. Three cases were studied: 1) a 64×64 resolution reconstruction, 2) a 128×128 resolution reconstruction, and 3) $2\times$ interpolation. These three methods are referred to as 64 , 128 and $2\times$ in Table 2.2. We ran 200 iterations of the CG reconstruction algorithm for each case.

Table 2.2: NRMSE (%) Difference between Unaccelerated and Fast Approach

Reso.	M_0	R_2^*	ω
64	0.8	0.4	0.5
128	1.4	0.3	0.3
2x	0.5	0.5	0.3

Table 2.3: NRMSE (%) of Noiseless Reconstruction

Reso.	Fast			Unaccelerated		
	M_0	R_2^*	ω	M_0	R_2^*	ω
64	21.3	20.5	20.4	21.1	20.4	20.3
128	44.3	23.6	23.9	44.4	23.6	24.0
2x	15.3	15.4	16.3	15.3	15.4	16.3

These results indicate that the error introduced by the approximations in the fast approach is quite small — quite a bit smaller than the typical error one would expect due to noise in the signal.

2.6.2 Noiseless Experiments

We evaluated the performance of the reconstruction algorithm for a noiseless signal. The true images used to synthesize the FID and the reconstructed images are shown in Figure 2.14 and 2.15. We also computed the NRMS of these three methods compared to the true images in Table 2.3. After 76 iterations, the reduction rate of the cost function is less than 1% for cubic convolution reconstruction. For direct 64×64 reconstruction, this number is 118.

Because the simulation signal was generated from 1024×1024 images and the reconstruction algorithms are based on 64×64 or 128×128 resolution, this mismatching leads the reconstruction algorithm to converge to a solution that is not perfectly accurate.

The results of this experiment indicate that the approximation error due to the polynomial model leading to algorithm acceleration is far less than the discrete modeling error caused by the limited spatial resolution of the parameter maps.

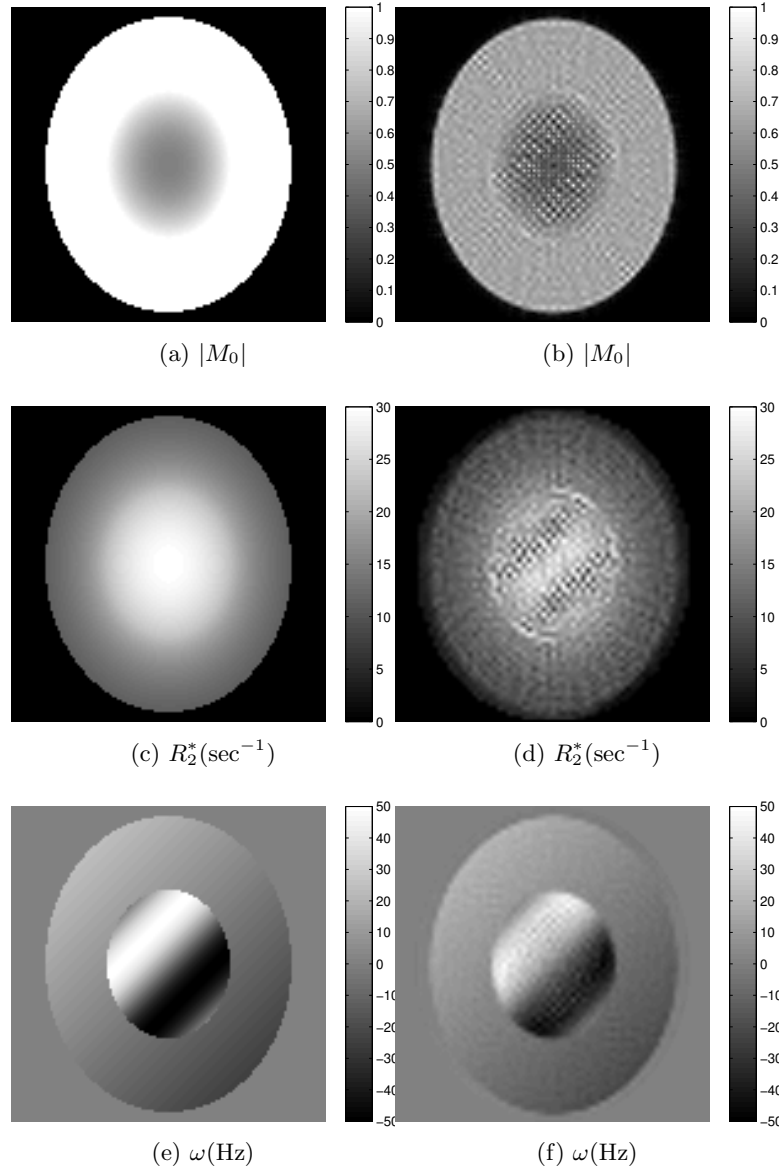


Figure 2.14: True and Reconstructed Images from Noiseless Experiments. All images are displayed with 128×128 resolution. We only reconstructed the pixels within the inscribed circle of the square. (a)(c)(e) are true images; (b)(d)(f) are from 64×64 reconstruction without interpolation, then interpolated to 128×128 images for display.

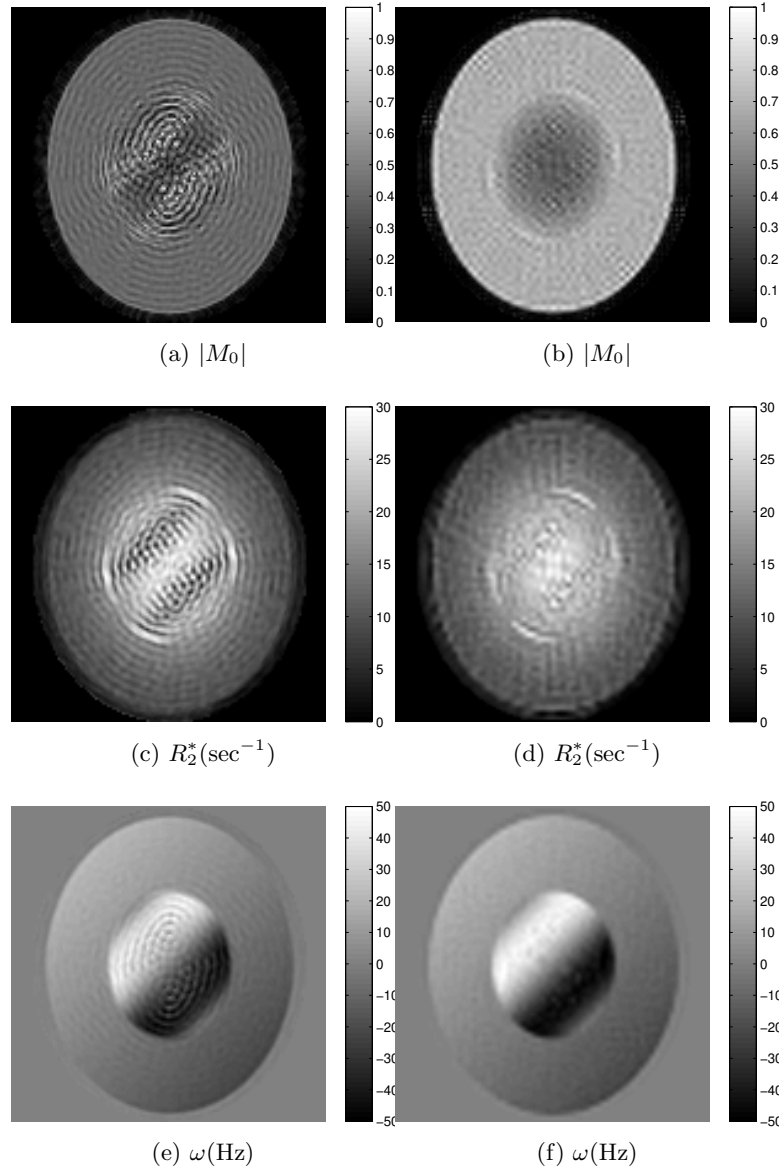


Figure 2.15: Reconstructed images from noiseless experiments. All images are displayed with 128×128 resolution. (a)(c)(e) are from 128×128 reconstruction without interpolation, (b)(d)(f) are images reconstructed from $2 \times$ cubic convolution interpolation, so the interpolation coefficients are 64×64 .

2.6.3 Noisy Experiment

We added white Gaussian noise to the synthesized signal and reconstructed the images from the noisy signal. The SNR is defined by:

$$\text{SNR} = \frac{\|\mathbf{s}\|^2}{N\sigma^2} \tag{2.30}$$

where σ^2 is the noise variance.

The images reconstructed from a noisy signal with 40 dB SNR are shown in Figure 2.16. The NRMSE of the reconstructed images at different SNRs is listed in Table 2.4.

Table 2.4: NRMSE (%) of Noisy Reconstruction

	Reso.	M_0	R_2^*	ω
30dB	64	30.4	31.1	31.1
	128	82.3	36.9	35.5
	2x	28.0	29.7	27.4
40dB	64	23.1	22.6	23.0
	128	48.5	25.8	26.2
	2x	17.2	18.9	18.0
50dB	64	23.1	21.0	21.7
	128	45.1	24.3	24.7
	2x	15.4	16.7	16.6

We observe that the noise even for 30 dB is on the same order as the error due to the spatial-domain modeling error. Furthermore, the estimates degrade gracefully with decreasing SNR.

2.6.4 Phantom and Animal Experiment

We applied this method to data collected from two phantom experiments using a 4.7T 60cm-vertical-bore Varian primate MRI system along with a stripline resonator quadrature head coil. We used transverse cross-sectional rosette trajectories with a slice thickness of

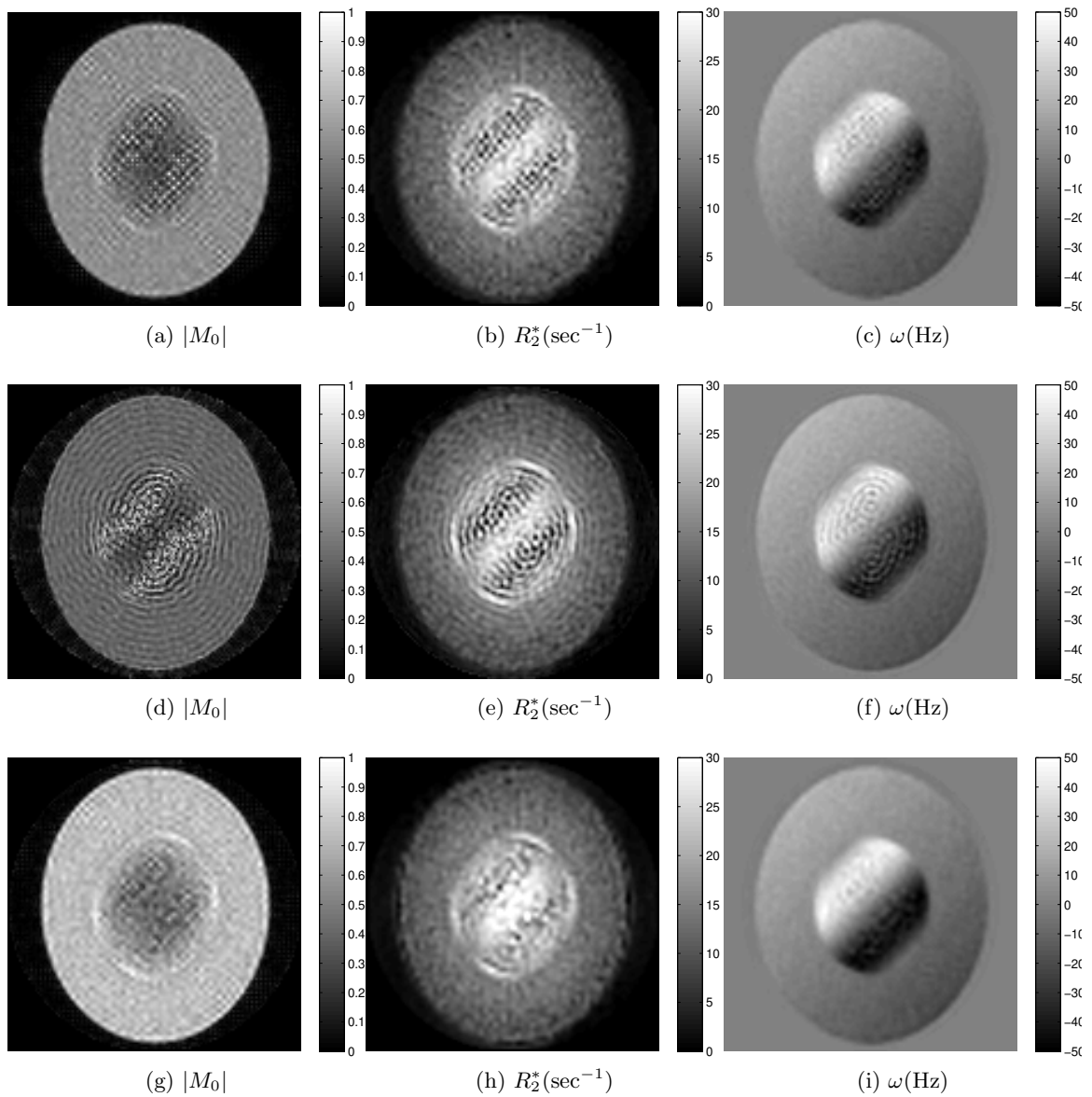


Figure 2.16: Images reconstructed from noisy signals. SNR is 40dB. All images have 128×128 resolution. (a)-(c) are from 64×64 reconstruction without interpolation, then interpolated to 128×128 images for display; (d)-(f) are from 128×128 reconstruction without interpolation, (g)-(i) are images reconstructed from $2 \times$ cubic convolution interpolation, so the interpolation coefficients are 64×64 .

2mm. The phantom was constructed from an 8cm-diameter beaker containing four 1.6cm-diameter tubes. The tubes were filled with agarose gel and various concentrations of either CuSO_4 or Sephadex beads to obtain different R_2^* values.

The results of the first experiment are compared in Figure 2.17. The interpolation method yields both sharper edges and smoother regions inside the circles. For the R_2^* parameter map in which fMRI is interested, the interpolation method gives better results. In (e), the small circles are clearer than in (b), especially the two circles in the lower part. The artifacts are also less visible in (e).

We also did an experiment with a much larger frequency offset using the same type of phantom. The object was deliberately deshimmmed to show the robustness of the interpolated method. The results are shown in Figure 2.18. We can see more obvious improvements in the reconstruction of R_2^* .

The results of a monkey experiment are shown in Figure 2.19. Image data of a macaque monkey brain were obtained using the Varian system with a rosette trajectory. The sampling interval was $4.59\mu s$, and the acquisition duration was $55.0ms$. Images were reconstructed using the proposed algorithm. In the interpolated image, the anatomic features are clearly visible. The frequency tends to be more homogeneous inside the brain and has rises or dips near the edges as is often the case. The cerebral ventricles, which have a butterfly-like shape in this slice, can be seen in the frequency map. The interpolated image shows more high-frequency detail than the non-interpolated 64×64 image even though it does not require the estimation of more free parameters.

In all experiments, the images of M_0 are normalized to 1.

2.7 Conclusion

This paper presents a new method to reconstruct local magnitude, decay and frequency at higher resolution from limited data of a single-shot MRI signal. Using interpolation, the reconstruction algorithm is well constrained since it allows us to avoid overparameterizing the solution. Simulated data shows that the interpolation method also gives a numerically

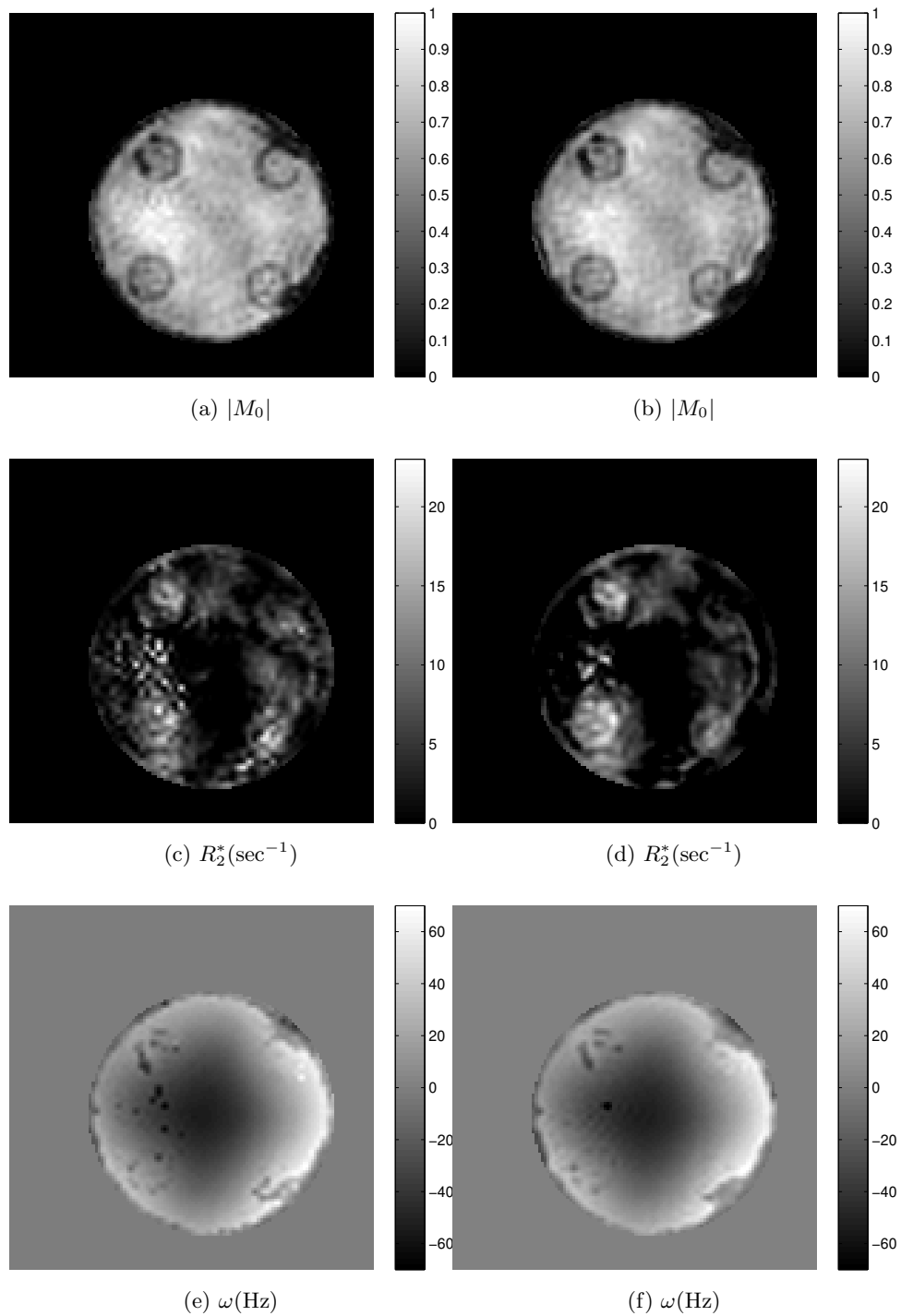


Figure 2.17: Images reconstructed from phantom experiment. All images have 128×128 resolution and are masked to remove exterior artifactual features. (a)(c)(e) are from 64×64 reconstruction without interpolation, then interpolated to 128×128 images for display; (b)(d)(f) are images reconstructed from $2 \times$ cubic convolution interpolation, so the interpolation coefficients are 64×64 .

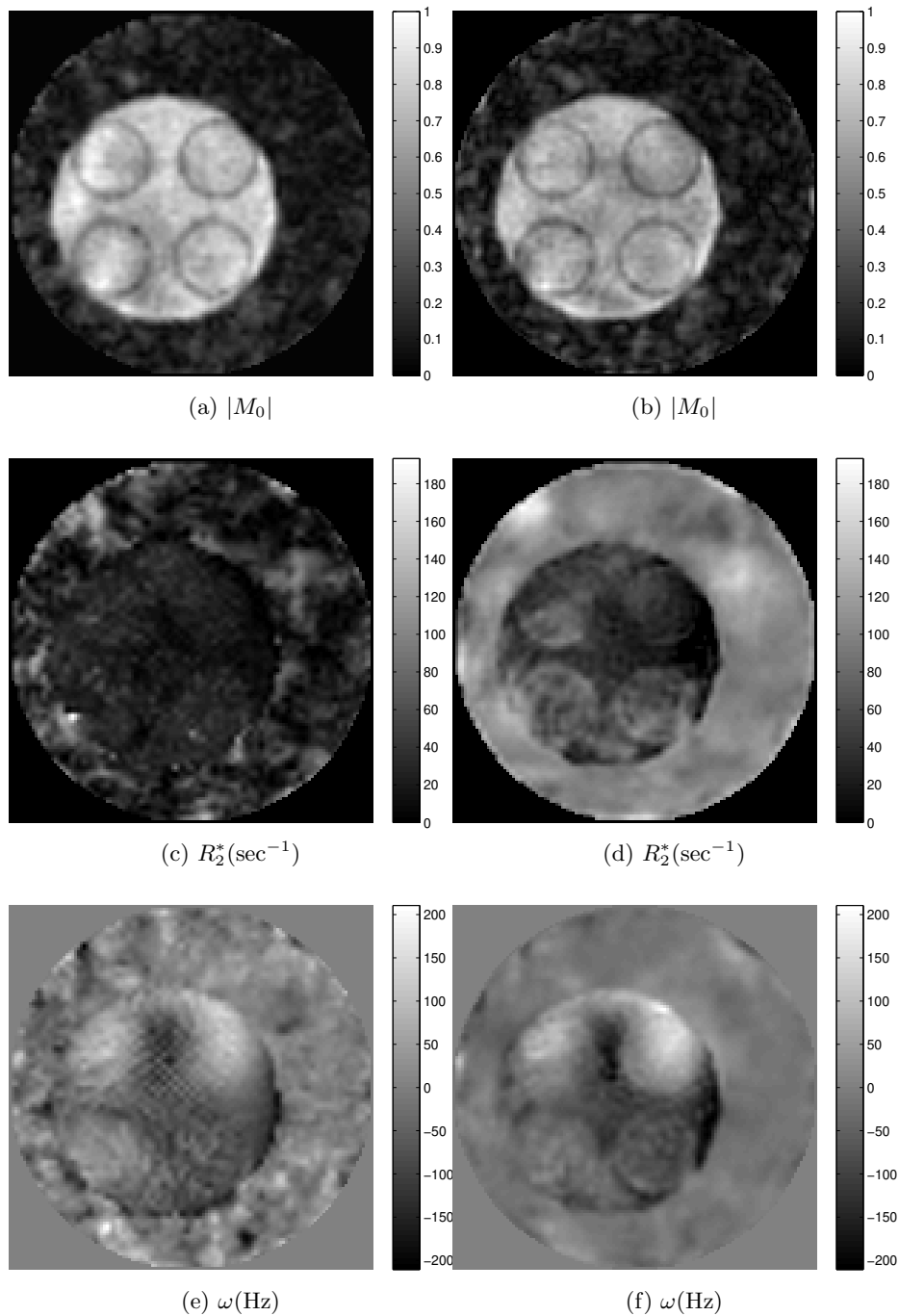


Figure 2.18: Images reconstructed from phantom experiment with larger frequency offset. All images have 128×128 resolution. (a)(c)(e) are from 64×64 reconstruction without interpolation, then interpolated to 128×128 images for display; (b)(d)(f) are images reconstructed from $2 \times$ cubic convolution interpolation, so the interpolation coefficients are 64×64 . Only the frequency map of the imaged object is shown in (e) and (f). The deliberately added frequency map is removed from these two figures. The artifactual features between the reconstruction mask (the inscribed circle of the square) and the imaged object remain, but they are not of interest.

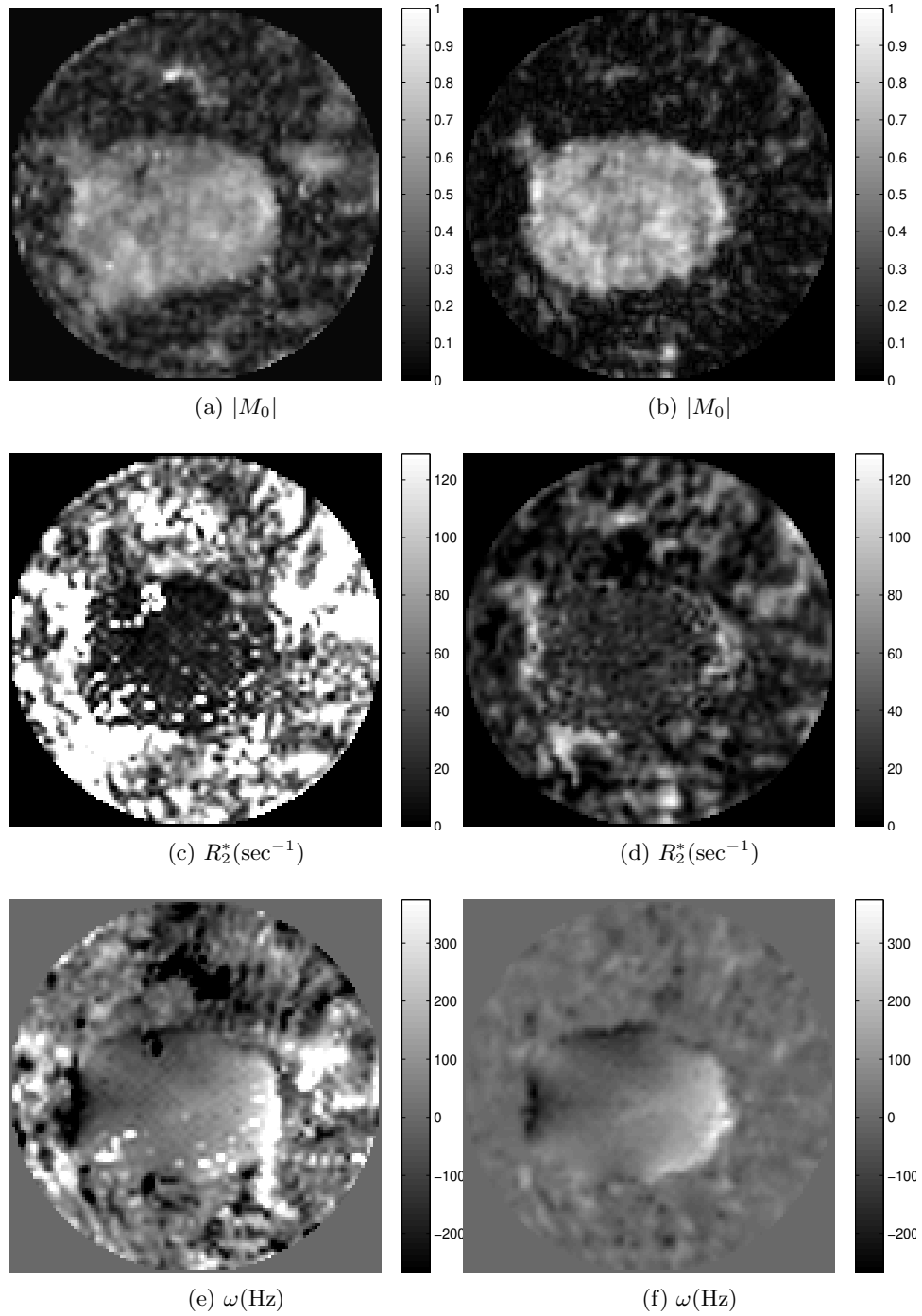


Figure 2.19: Images reconstructed from monkey experiment. All images have 128×128 resolution. (a)(c)(e) are from 64×64 reconstruction without interpolation, then interpolated to 128×128 images for display; (b)(d)(f) are images reconstructed from $2 \times$ cubic convolution interpolation, so the interpolation coefficients are 64×64 . The R_2^* map in (c) was plotted with saturation of the values to maintain the same scale as (d) and so that the details of (d) would be visible.

better result in reconstructing magnitude, decay and frequency. From our experimental data, we can also observe the visual improvement due to the interpolation method. We applied a polynomial approximation of the time exponential function to this method to reduce computational complexity. Computer simulation shows that there is no significant difference between the accelerated and the unaccelerated methods.

CHAPTER 3

NONUNIFORM FAST FOURIER TRANSFORM (NUFFT)

Unlike classical MRI sampling methods that uniformly sample the spatial frequency domain, SS-PARSE nonuniformly samples k -space. One approach that allows FFTs to be used in the reconstruction algorithm is to round a non-equally spaced frequency-domain trajectory onto an equally spaced grid. Oversampling can be used to reduce the error introduced by this rounding. By analyzing the reconstruction errors of the fast algorithm, we know that the primary source of the errors is the trajectory gridding. A grid with higher resolution can reduce the errors, but it could make the reconstruction process much slower while also requiring a great deal more memory. An algorithm that can accurately and quickly evaluate Fourier samples is desirable. In this chapter, we discuss the implementation of the fast algorithms for evaluating Fourier transforms (FTs). We focus on 1-D FTs. 1-D FTs can be easily extended to multidimensional Fourier samples because of the separability of Fourier kernels.

3.1 Theory of NUFFT

3.1.1 Problem Statement

Let $\mathbf{x} = \{x_{-N/2}, \dots, x_{N/2-1}\}$ be a finite sequence of complex numbers. The discrete Fourier transform (DFT) is defined by the formula:

$$X_k = \sum_{n=-N/2}^{N/2-1} x_n e^{i \frac{2\pi}{N} kn} \quad (3.1)$$

where N is a positive even integer, $k = -N/2, \dots, N/2 - 1$. The frequency components $2\pi k/N$ are equally spaced, so (3.1) can be evaluated by an FFT, which requires $O(N \log N)$ operations.

Now, we extend this definition to nonuniformly spaced frequency components. $\boldsymbol{\omega} = \{\omega_0, \dots, \omega_{K-1}\}$ is a finite sequence of real numbers, and $\omega_k \in [-\pi, \pi]$ for $k = 0, \dots, K-1$. The Fourier transform of the finite sequence \mathbf{x} evaluated at the frequencies of $\boldsymbol{\omega}$ is given by:

$$X_k = \sum_{n=-N/2}^{N/2-1} x_n e^{in\omega_k} \quad (3.2)$$

The direct evaluation of (3.2) requires $O(NK)$ operations. Our goal is to design an algorithm that only needs computational complexity proportional to the FFT and meets a required accuracy.

3.1.2 Basic Concepts

[33] proved that any function of the form e^{icx} can be accurately represented on any finite interval on the real line using a small number of terms of the form $e^{bx^2} \cdot e^{ikx}$, and this number of terms is independent of the value of c .

Theorem 1 [33] *Let $b > \frac{1}{2}$, $c, d > 0$ be real numbers, and let $m \geq 2$, $q \geq 4b\pi$ be integers. Then, for any $x \in [-d, d]$,*

$$\left| e^{icx} - e^{b(x\pi/md)^2} \cdot \sum_{k=[cmd/\pi]-q/2}^{[cmd/\pi]+q/2} \rho_k e^{ikx\pi/md} \right| < e^{-b\pi^2(1-1/m^2)} \cdot (4b + 9) \quad (3.3)$$

where

$$\rho_k = \frac{1}{2\sqrt{b\pi}} e^{-(c-k)^2/4b} \quad (3.4)$$

This theorem can be written in a general form that is consistent with (3.2):

$$E_{n,k} = \left| e^{i\omega_k n} - s_n^{-1} \sum_{l=-\lfloor (J-1)/2 \rfloor}^{\lfloor (J-1)/2 \rfloor} g_l(\omega_k) e^{i2\pi(v_k+l)n/mN} \right| < \varepsilon \quad (3.5)$$

where s_n^{-1} is a function of n , $g_l(\omega_k)$ is a function ω_k , $v_k = \lfloor \omega_k mN/2\pi \rfloor$, integer $J \ll K$ and ε is a nonnegative real number.

With this approximation, one can evaluate (3.2) by an FFT and interpolation in the transform domain with two steps:

1. Compute an mN -point FFT of the weighted x_n .

$$Y_k = \sum_{n=-N/2}^{N/2-1} s_n^{-1} x_n e^{i\frac{2\pi}{mN}kn} \quad (3.6)$$

2. Approximate each X_m by a linear combination of Y_k 's.

$$X_k \approx \hat{X}_k = \sum_{l=-\lfloor (J-1)/2 \rfloor}^{\lfloor (J-1)/2 \rfloor} g_l(\omega_k) Y_{v_k+l} \quad (3.7)$$

The computational complexity of this algorithm is $O(mN \log mN + JK)$. If we choose constant scaling factor $\mathbf{s} = \{s_{-N/2}, \dots, s_{N/2-1}\}$ and $J = K$, this method exactly computes X_m , but there is no computational gain. The performance of this approximation is determined by \mathbf{s} and the weighting coefficients $\mathbf{g}(\omega_k)$.

[34–36] proposed different methods to compute \mathbf{s} and \mathbf{g} based on different criteria. All of the methods first optimize \mathbf{g} , then compute \mathbf{s} using the optimized \mathbf{g} . We present an algorithm that simultaneously optimizes \mathbf{s} and \mathbf{g} by least-squares approximation.

If the Fourier transform of a set of certain frequencies is only evaluated once, it not worth using the NUFFT scheme because of the computational complexity of optimizing the scaling factor and weighting coefficients. In some applications, such as iterative reconstruction of MRI, the same set of frequencies is used for each iteration. The same k -space trajectory (spatial frequencies) could also be used for different MRI experiments. In both

scenarios, the additional computational cost of precomputations of NUFFT can be afforded. Because of the periodicity of $g_l(\omega_k)$, g_l only needs to be precomputed for several ω_k in one period. The precomputed g_l are then used to interpolate the g_l for the new set of frequencies. The linear interpolation of K frequencies requires $2JK$ operations.

3.2 Least-Squares Optimization

For a given sequence x_n , the NUFFT approximation error at is expressed by:

$$\begin{aligned} \left| X_k - \hat{X}_k \right| &= \left| \sum_{n=-N/2}^{N/2-1} x_n e^{jn\omega_k} - \sum_{l=-\lfloor (J-1)/2 \rfloor}^{\lfloor (J-1)/2 \rfloor} g_l(\omega_k) \sum_{n=-N/2}^{N/2-1} s_n^{-1} x_n e^{j\frac{2\pi}{mN}kn} \right| \\ &= \left| \sum_{n=-N/2}^{N/2-1} x_n \left(e^{jn\omega_k} - s_n^{-1} \sum_{l=-\lfloor (J-1)/2 \rfloor}^{\lfloor (J-1)/2 \rfloor} g_l(\omega_k) e^{j\frac{2\pi}{mN}kn} \right) \right| \end{aligned} \quad (3.8)$$

By Cauchy-Schwarz inequality [34], we have:

$$\left| X_k - \hat{X}_k \right|^2 \leq \sum_{n=-N/2}^{N/2-1} |x_n|^2 \sum_{n=-N/2}^{N/2-1} \left| e^{jn\omega_k} - s_n^{-1} \sum_{l=-\lfloor (J-1)/2 \rfloor}^{\lfloor (J-1)/2 \rfloor} g_l(\omega_k) e^{j\frac{2\pi}{mN}kn} \right|^2 \quad (3.9)$$

For all possible sequences x_n with norm 1, the maximum error is:

$$\sum_{n=-N/2}^{N/2-1} E_{n,k}^2 \quad (3.10)$$

where $E_{n,k}$ is defined in (3.5). The total error for all ω_k is:

$$\varepsilon = \sum_{k=0}^{K-1} \sum_{n=-N/2}^{N/2-1} E_{n,k}^2 \quad (3.11)$$

Our goal is to minimize ε with respect to s_n and $g_l(\omega_k)$. This minimization problem can be formulated in a matrix form:

$$\operatorname{argmin}_{\mathbf{S}, \mathbf{G}} \|\mathbf{B} - \mathbf{S}^{-1} \mathbf{A} \mathbf{G}\|_2^2 \quad (3.12)$$

where \mathbf{A} is an $N \times J$ matrix, \mathbf{G} is a $J \times K$ matrix vector, \mathbf{S} is an $N \times N$ diagonal matrix, and \mathbf{B} is an $N \times K$ matrix. These are defined by:

$$\begin{aligned} A_{nl} &= e^{i2\pi nl/mN} \\ S_{nn} &= s_n \\ B_n &= e^{i\omega n} \cdot e^{-i2\pi(v-q/2)n/mN} \end{aligned}$$

where $n = -N/2, \dots, N/2 - 1$, $l = 0, \dots, J - 1$, and K is the length of $\boldsymbol{\omega}$.

(3.12) is a nonlinear problem. It can be approximated by a linear minimization problem:

$$\operatorname{argmin}_{\mathbf{S}, \mathbf{G}} \|\mathbf{S} \mathbf{B} - \mathbf{A} \mathbf{G}\|_2^2 \quad (3.13)$$

Obviously, $\mathbf{S} = \mathbf{0}$, $\mathbf{G} = \mathbf{0}$ is a solution to this problem. We can use $s_0 = 1$ to avoid this solution. With this constraint, it can be shown that (3.13) is equivalent to the standard linear minimization problem.

We write \mathbf{G} as a column vector \mathbf{g} with $G_{m,n} = g_{(n-1)J+m}$. Let \mathbf{b}_i denote the i th column of \mathbf{B} . $\mathbf{d}\mathbf{b}_i$ is a diagonal matrix with the elements of \mathbf{b}_i on its diagonal. We define a sparse matrix as:

$$\mathbf{F} = \begin{pmatrix} -\mathbf{d}\mathbf{b}_1 & \mathbf{A} & \mathbf{0} & & \\ -\mathbf{d}\mathbf{b}_2 & & \mathbf{A} & & \\ \vdots & \mathbf{0} & & \ddots & \\ -\mathbf{d}\mathbf{b}_K & & & & \mathbf{A} \end{pmatrix} \quad (3.14)$$

We define column vector \mathbf{s} that is composed of s_n . Now we have:

$$\mathbf{SB} - \mathbf{AG} = \mathbf{F} \begin{pmatrix} \mathbf{s} \\ \mathbf{g} \end{pmatrix} \quad (3.15)$$

Let $s_0 = 1$, and $-\mathbf{y}$ be the $(N/2 + 1)$ th column of \mathbf{F} . We remove $-\mathbf{y}$ from the matrix \mathbf{F} to form a new matrix \mathbb{A} . Column vector \mathbf{x} is a stack of \mathbf{s} and \mathbf{g} without s_1 . Now, (3.13) is converted to a standard linear minimization problem:

$$\underset{\mathbf{x}}{\operatorname{argmin}} \|\mathbb{A}\mathbf{x} - \mathbf{y}\|_2^2 \quad (3.16)$$

In Figures 3.1 and 3.2, we compare the performance of this “direct” solving method with min-max, the best available method. The maximum error is defined as:

$$\varepsilon_{\max} = \max_k \left(\frac{\sum_{n=-N/2}^{N/2-1} E_{n,k}^2}{N} \right)^{1/2} \quad (3.17)$$

We can further improve the NUFFT accuracy. We initialize \mathbf{s} with the results of direct solving, Kaiser-Bessel window, or Gaussian function, then we solve \mathbf{G} by:

$$\mathbf{G} = (\mathbf{A}^H \mathbf{A})^{-1} \mathbf{A}^H \mathbf{SB} \quad (3.18)$$

We use \mathbf{G} to optimize \mathbf{s} :

$$\mathbf{s} = (\mathbf{C}^H \mathbf{C})^{-1} \mathbf{C}^H \mathbf{Z} \quad (3.19)$$

where \mathbf{Z} is an $NK \times 1$ column vector from \mathbf{AG} , and $\mathbf{C} = [\mathbf{db}_1, \dots, \mathbf{db}_K]^T$.

If necessary, we can use the updated \mathbf{s} to find the optimal \mathbf{G} . This method is efficient in reducing the maximum error. The maximum error of this method is compared with that of min-max in Figure 3.3

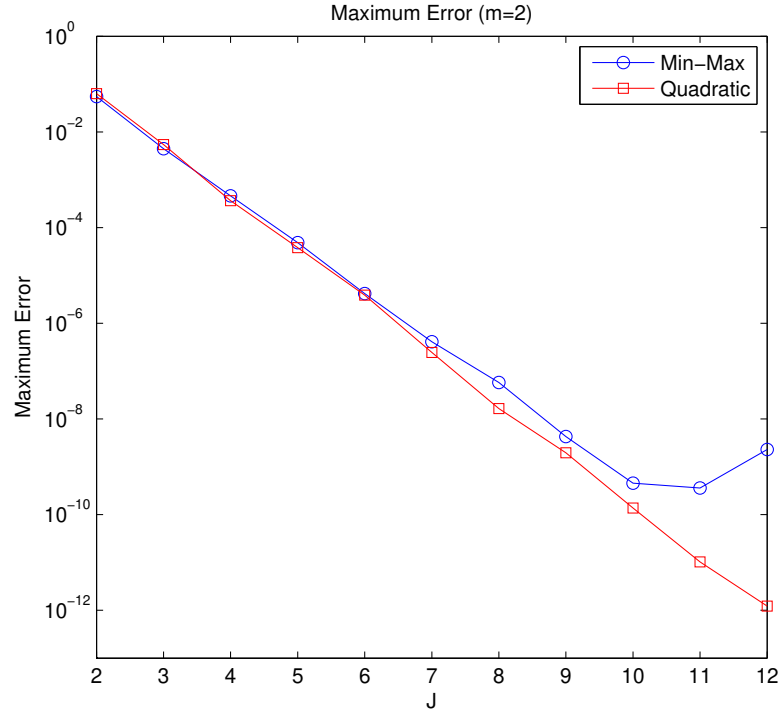


Figure 3.1: Maximum Error

3.3 Interpolations

In 3.2, we developed the approximation for a set of specific frequencies. This approximation gives higher accuracy than other methods. In some applications, one can use the precomputed $g_l(\omega_k)$ to find the g_l for given frequencies by interpolations. In this section, we analyze the errors for two kinds of interpolations, linear and cubic convolution.

Let f be a real number with $|f| \leq 1/m$, and $\omega = 2\pi f/N$.

$$e^{i2\pi n f/N} \approx s_n^{-1} \sum_{l=-\lfloor (J-1)/2 \rfloor}^{\lfloor (J-1)/2 \rfloor} g_l(f) e^{i2\pi n l/mN} \quad (3.20)$$

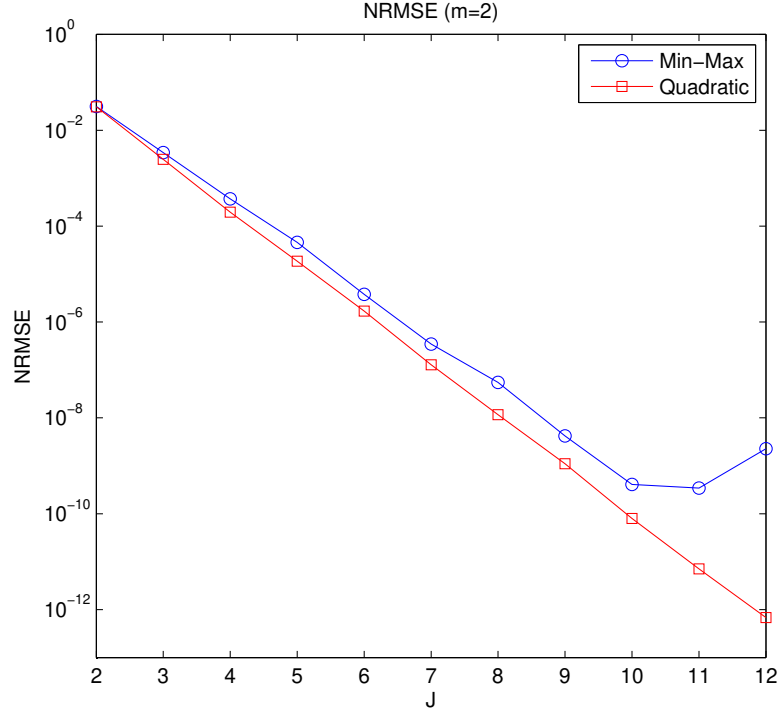


Figure 3.2: NRMS Error

It can be shown that $g_l(f)$ is a periodic function with period $1/m$:

$$\begin{aligned}
 e^{i2\pi n(f+k/m)/N} &\approx s_n^{-1} e^{i2\pi n k/mN} \sum_{l=-\lfloor (J-1)/2 \rfloor}^{\lfloor (J-1)/2 \rfloor} g_l(f) e^{i2\pi n l/mN} \\
 &= s_n^{-1} \sum_{l=-\lfloor (J-1)/2 \rfloor}^{\lfloor (J-1)/2 \rfloor} g_l(f) e^{i2\pi n(l+k)/mN}
 \end{aligned} \tag{3.21}$$

where k is an integer. With this property, we only need to study the NUFFT within one period.

We use the precomputed $g_l(f_k)$ for a set of frequencies f_k to compute $g_l(x)$ of any other frequency x by interpolation:

$$g_l(x) = \sum_k g_l(f_k) u\left(\frac{x}{h} - k\right) \tag{3.22}$$

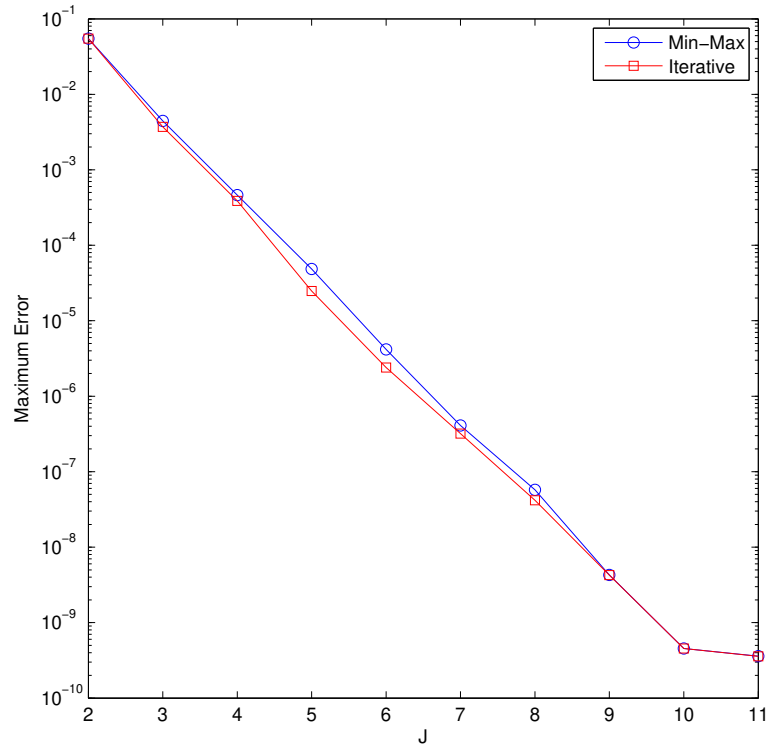


Figure 3.3: Maximum Error

where $u(x)$ is the interpolation kernel.

There are several candidates for the interpolation kernel. We use the linear spline and cubic convolution as examples. The linear kernel (3.23) and cubic kernel (3.24) are plotted in Figures 3.4 and 3.5, respectively.

$$u(x) = \begin{cases} 1 - |x|, & |x| < 1 \\ 0, & \text{otherwise} \end{cases} \quad (3.23)$$

$$u(x) = \begin{cases} \frac{3}{2}|x|^3 - \frac{5}{2}|x|^2 + 1, & 0 \leq |x| < 1 \\ -\frac{1}{2}|x|^3 + \frac{5}{2}|x|^2 - 4|x| + 1, & 1 \leq |x| < 2 \\ 0 & 2 \leq |x| \end{cases} \quad (3.24)$$

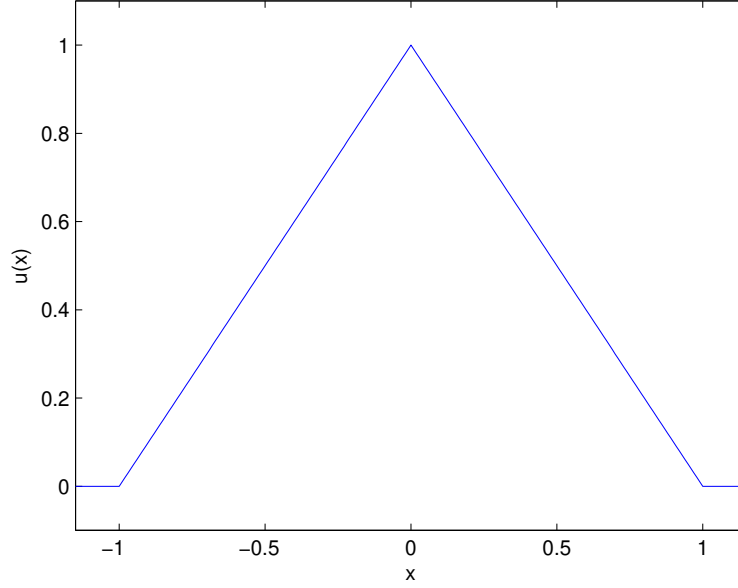


Figure 3.4: Linear Interpolation Kernel

Let K be a positive integer, J be an odd number, and $h = 1/mK$. We choose the following frequency set:

$$\mathbf{f} = \left\{ f_k = -\frac{1}{2m} + kh, \quad k = -1, 0, \dots, K + 1 \right\}$$

so there are $K + 3$ elements in \mathbf{f} . We compute the interpolator coefficients $\mathbf{G}(\mathbf{f})$ and the corresponding cubic convolution coefficients $c_l(k)$. For any frequency $x \in [-1/2m, 1/2m]$, we use cubic convolution interpolation to compute $g_l(x)$.

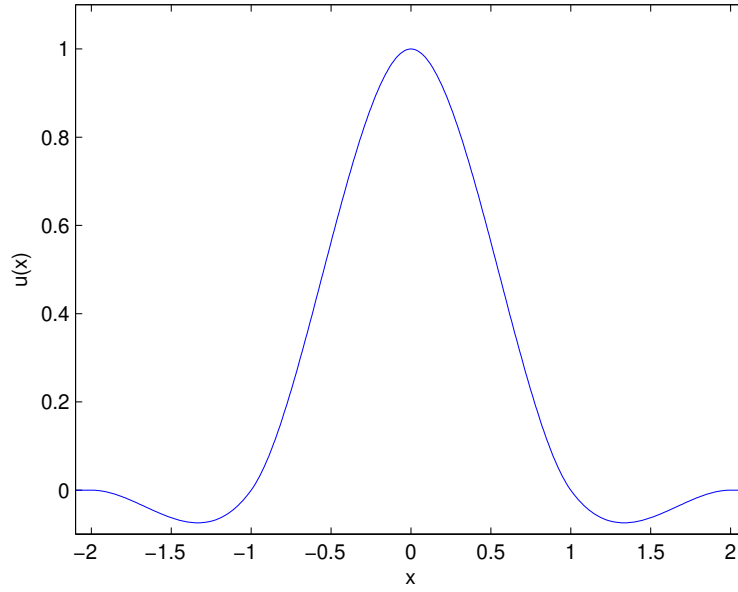


Figure 3.5: Cubic Convolution Interpolation Kernel

For even J , we choose a different \mathbf{f} to make $g_l(x)$ continuous:

$$\mathbf{f} = \{f_k = kh, \quad k = -1, 0, \dots, K + 1\}$$

In both cases, we set $v_k = 0$ for all k .

For linear interpolation, we choose a slightly different \mathbf{f} :

$$\mathbf{f} = \left\{ f_k = -\frac{1}{2m} + kh, \quad k = 0, \dots, K \right\}$$

for odd J , and

$$\mathbf{f} = \{f_k = kh, \quad k = 0, \dots, K\}$$

for even J .

3.4 Error Analysis of the Interpolation

For odd J , the normalized root mean square error (NRMSE) is computed by:

$$\begin{aligned}\varepsilon^2 &= \frac{m}{N} \sum_{n=-N/2}^{N/2-1} \int_{\mathbf{x}} \left| e^{i2\pi nx/N} - s_n^{-1} \sum_{l=-\lfloor (J-1)/2 \rfloor}^{\lfloor (J-1)/2 \rfloor} g_l(x) e^{i2\pi nl/mN} \right|^2 dx \\ &= \frac{m}{N} \sum_{n=-N/2}^{N/2-1} \sum_k \int_{f_k}^{f_{k+1}} \left| e^{i2\pi nx/N} - s_n^{-1} \sum_{l=-\lfloor (J-1)/2 \rfloor}^{\lfloor (J-1)/2 \rfloor} g_l(x) e^{i2\pi nl/mN} \right|^2 dx\end{aligned}\quad (3.25)$$

For odd J , the integral interval \mathbf{x} is $[-1/2m, 1/2m]$; for even J , \mathbf{x} is $[0, 1/m]$.

The error performance of linear and cubic convolution interpolations are illustrated in Figures 3.6, 3.7, 3.8 and 3.9 with $m = 2$. Figure 3.10 compares the performance of linear and cubic convolution interpolations.

For $J \geq 8$, the linear interpolation can not approach the accuracy of the LS optimization because the performance is dominated by the accuracy of the linear interpolator. For cubic convolution interpolation, the error of the LS optimization plays the major role, so the performance can approach the possible limit with more precomputed frequencies.

3.5 Inverse Fourier Transform

We use *inverse* to represent the Fourier transforms with uniform inputs and nonuniform outputs. The inverse FT is defined as:

$$x_n = \sum_{k=0}^{K-1} X_k e^{m\omega_k} \quad (3.26)$$

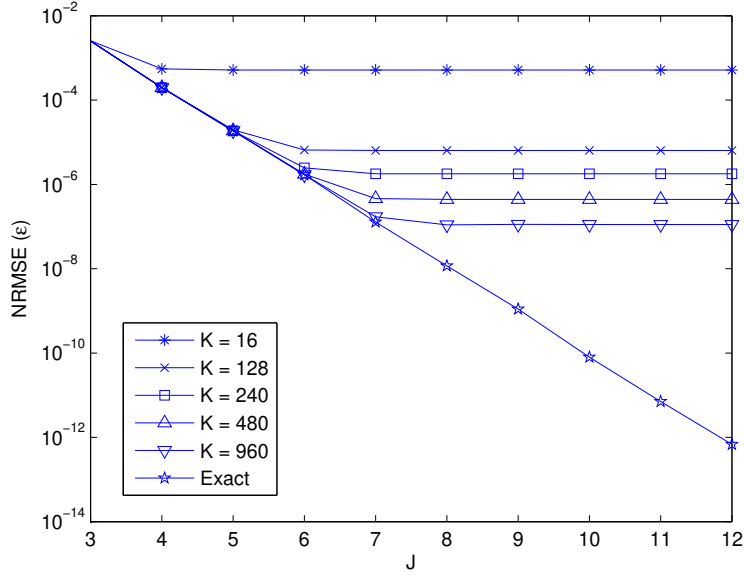


Figure 3.6: NRMSE for different J and the number of precomputed frequencies for linear interpolation. In this figure, NRMSEs are plotted as the functions of J 's for different numbers of the precomputed frequencies. The “Exact” is the NRMSE for the precomputed frequencies. The “Exact” is the accuracy limit of the method stated in this chapter.

An inverse FT can be approximated by

$$\begin{aligned}
 x_n &\approx \sum_{k=0}^{K-1} X_k s_n^{-1} \sum_{l=-\lfloor (J-1)/2 \rfloor}^{\lfloor (J-1)/2 \rfloor} g_l(\omega_k) e^{i2\pi n(v_k+l)/mN} \\
 &= s_n^{-1} \sum_{k=0}^{K-1} X_k \underbrace{\sum_{l=-\lfloor (J-1)/2 \rfloor}^{\lfloor (J-1)/2 \rfloor} g_l(\omega_k) e^{i2\pi nl/mN}}_{A_k} e^{i2\pi n v_k/mN}
 \end{aligned} \tag{3.27}$$

The procedure of the inverse NUFFT is summarized as following:

1. Compute A_k . This requires JK operations.

$$A_k = \sum_{l=-\lfloor (J-1)/2 \rfloor}^{\lfloor (J-1)/2 \rfloor} g_l(\omega_k) e^{i2\pi nl/mN}$$

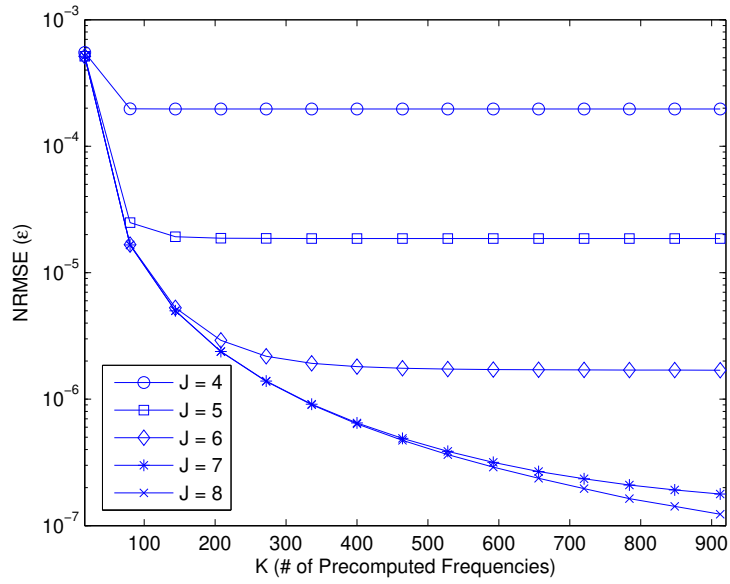


Figure 3.7: NRMSE for different J and the number of precomputed frequencies for linear interpolation. In this figure, NRMSEs are plotted as the functions of the numbers of the precomputed frequencies for different J 's.

2. Weight X_k by A_k .

$$B_{k-N/2} = X_{v_k} A_{v_k}, \quad k = 0, \dots, K-1$$

3. Compute an mN -point FFT.

$$y_n = \sum_{k=-N/2}^{N/2-1} B_k e^{i2\pi nk/mN}$$

4. Weight y_n by s_n^{-1}

$$x_n = s_n^{-1} y_n$$

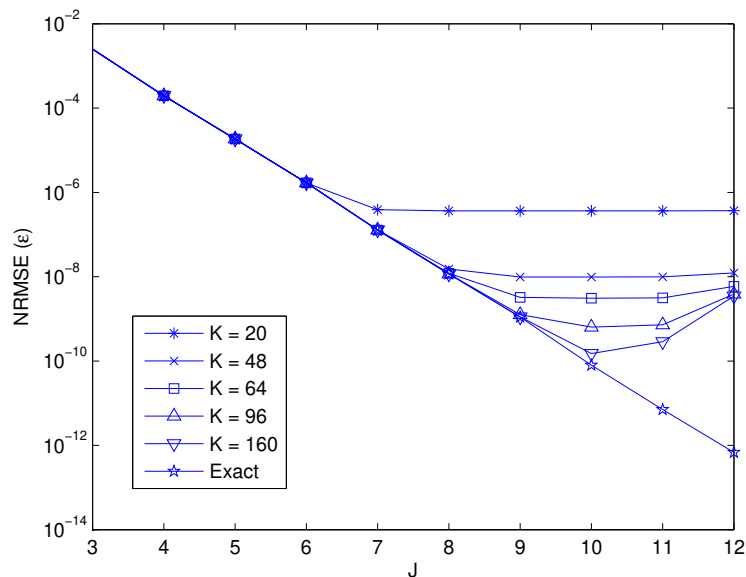


Figure 3.8: NRMSE for different J and the number of precomputed frequencies for cubic convolution interpolation. In this figure, NRMSEs are plotted as the functions of J 's for different numbers of the precomputed frequencies. The “Exact” is the NRMSE for the precomputed frequencies. The “Exact” is the accuracy limit of the method stated in this chapter.

3.6 Discussion

For a given set of K frequencies, it requires $2JNM$ operations are required to compute g_l and s_n for an N -point FFT. So it is not economical to do this for a set of frequencies that are repeatedly used. Once we have g_l and s_n , the Fourier transform requires $O(mN \log mN + JM)$ operations.

With precomputed g_l and s_n , one can use linear or cubic interpolation to evaluate g_l for the given K frequencies. Linear interpolation requires $2JM$ operations to compute g_l for the given frequencies. The total computational complexity is $O(mN \log mN) + 2JM$. This method requires less computations than cubic interpolation. The disadvantage of linear interpolation is that its NRMSE reaches the lower limit of about 10^{-7} due to interpolation error. For hardware implementation, the storage of the precomputed data of a larger set

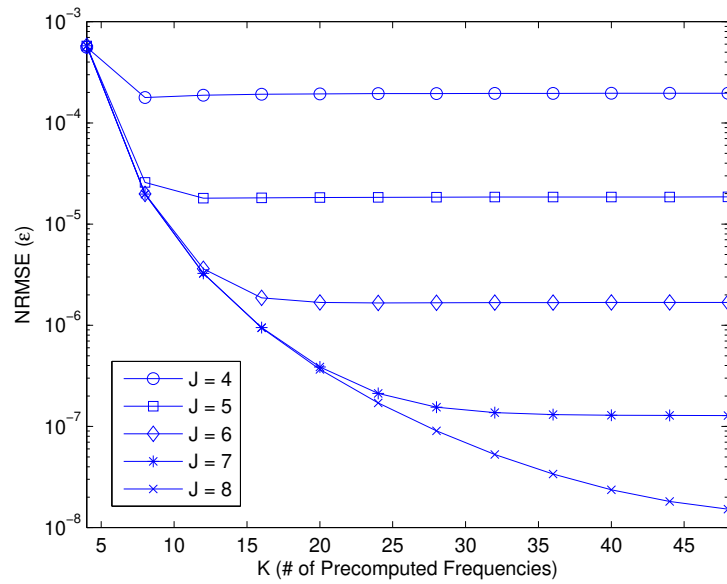


Figure 3.9: NRMSE for different J and the number of precomputed frequencies for cubic convolution interpolation. In this figure, NRMSEs are plotted as the functions of the numbers of the precomputed frequencies for different J 's.

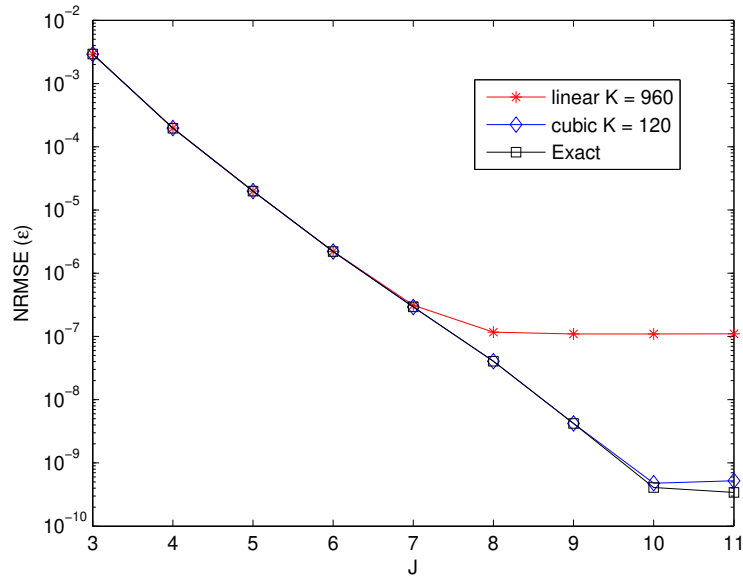


Figure 3.10: Comparison of the performance of linear and cubic convolution interpolations. The “Exact” is the accuracy limit of the method stated in this chapter.

of frequencies is also a possible problem. Its advantage is for $J \leq 5$, since about 100 precomputed frequencies can reach the best possible performance.

The cubic convolution interpolation requires more computations. The interpolation needs $4JM$ operations, so the total number is $O(mN \log mN) + 4JM$. The cubic algorithm can provide much higher accuracy than the linear algorithm. It also requires much less storage because fewer precomputed points are required for the same accuracy. This feature is useful for some hardware implementations. This is also possibly useful for some software applications even if there is enough memory because memory access could be the bottleneck.

CHAPTER 4
RECONSTRUCTION OF PARALLEL MRI

4.1 Introduction

The concept of parallel MRI was first suggested by Carlson [37], but his work was unknown until 2004 [38]. The introduction of simultaneous acquisition of spatial harmonics (SMASH) [39] started the age of parallel MRI.

The conventional Fourier MRI is modeled by

$$y(t) = \int M(\mathbf{x})e^{i\mathbf{k}(t)\cdot\mathbf{x}} d\mathbf{x}$$

There is more than one RF coil in a parallel MRI system. Each coil has a different receiving property that is called localized sensitivity. Let $C_k(\mathbf{x})$ be the localized sensitivity of the k th coil, $k = 1, \dots, K$. The received signal at the k th coil can be modeled by

$$y_k(t) = \int C_k(\mathbf{x})M(\mathbf{x})e^{i\mathbf{k}(t)\cdot\mathbf{x}} d\mathbf{x} + \varepsilon_k(t) \tag{4.1}$$

where $\varepsilon_k(t)$ is additive white Gaussian noise with zero mean and σ_ε^2 variance.

[40] summarized the advantages of parallel imaging:

- faster imaging.
- higher spatial resolution.
- improved image quality of single-shot or turbo-spin-echo or echo-planar by shortening the echo train whenever it is severely affected by signal decay and field inhomogeneities.
- complement for the increased SNR and compensation for the growing specific absorption rate and increasing geometric distortions for high and ultra-high field MRI.

The SNR (signal-to-noise ratio) can be increased with array coils in the same imaging time. The array coils can also be used for partially parallel acquisition (PPA) [41]. In this chapter, we extend the parallel MRI model (4.1) with the concept of SS-PARSE.

In current reconstruction algorithms, the coil sensitivities $C_k(\mathbf{x})$ are found by putting an known object in a parallel MRI system and measuring the spatial sensitivities directly. This method is convenient, but it is inaccurate because different objects may have different coil sensitivities due to the fact that each object has its own properties that interact with the coil responses. We can bring the concept of SS-PARSE into parallel MRI. We call this extension single-shot parallel PARSE (SS-pPARSE). The received signal in the k th coil is modeled by:

$$y_k(t) = \int C_k(\mathbf{x})M_0(\mathbf{x})e^{[R_2^*(\mathbf{x})+\omega(\mathbf{x})]t}e^{i\mathbf{k}(t)\cdot\mathbf{x}}d\mathbf{x} + \varepsilon_k(t) \quad (4.2)$$

The goal of PSSPARSE is to reconstruct $C_k(\mathbf{x})$, $M_0(\mathbf{x})$, $R_2^*(\mathbf{x})$ and $\omega(\mathbf{x})$ from the observed signals $y_k(t)$ for all $k = 1, \dots, K$.

4.2 Reconstruction

4.2.1 Extension of SS-PARSE

By discretizing (4.2) on the spatial (x, y) grid indexed by i , we have

$$y_k(n) = \underbrace{\sum_i C_{k,i}M_{0i}e^{nW_i}e^{i\mathbf{k}_n\cdot\mathbf{x}_i}}_{\hat{y}_k} + \varepsilon_k(n) \quad (4.3)$$

where $n = 1, \dots, N$, $W_i = -[R_{2i}^* + \omega_i] \Delta t$, $\mathbf{k}_n = \mathbf{k}(n\Delta t)$, and Δt is the sampling interval.

We use the method discussed in Chapter 2 to simultaneously solve C_k , M_0 and W . We use iterative conjugate-gradient algorithm to minimize the cost function:

$$J(\mathbf{z}) = \sum_{k=1}^K \|\mathbf{y}_k - \hat{\mathbf{y}}_k(\mathbf{z})\|^2 \quad (4.4)$$

with respect to \mathbf{z} , where $\mathbf{z} = \{\mathbf{C}_k, \mathbf{M}_0, \mathbf{W}, k = 1, \dots, K\}$.

The gradient $\nabla_{\mathbf{z}} J$ computations include three parts:

$$\frac{\partial J}{\partial \mathbf{M}_0} = \sum_{k=1}^K \mathbf{C}_k \sum_{n=1}^N f_k(n) e^{n\mathbf{W}} e^{i\mathbf{k}_n \cdot \mathbf{x}} \quad (4.5)$$

$$\frac{\partial J}{\partial \mathbf{W}} = \mathbf{M}_0 \sum_{k=1}^K \mathbf{C}_k \sum_{n=1}^N n f_k(n) e^{n\mathbf{W}} e^{i\mathbf{k}_n \cdot \mathbf{x}} \quad (4.6)$$

$$\frac{\partial J}{\partial \mathbf{C}_k} = \mathbf{M}_0 \sum_{n=1}^N f_k(n) e^{n\mathbf{W}} e^{i\mathbf{k}_n \cdot \mathbf{x}} \quad (4.7)$$

where $f_k(n) = [\hat{y}_l(n) - y_k(n)]^*$.

We apply the polynomial approximation of the exponential time function in Chapter 2 to compute the cost function and gradient for parallel MRI.

$$y_k(n) \approx e^{jn\omega_0} \sum_{l=0}^{L-1} n^l \sum_{i=1}^K C_{k,i} M_{0i} Z_i(l) e^{i\mathbf{k}_n \cdot \mathbf{x}^{(i)}} \quad (4.8)$$

$$\frac{\partial J}{\partial \mathbf{M}_0} \approx \sum_{k=1}^K \mathbf{C}_k \sum_{l=0}^{L-1} \mathbf{Z}(l) \sum_{n=1}^N f_k(n) e^{in\omega_0} n^l e^{i\mathbf{k}_n \cdot \mathbf{x}} \quad (4.9)$$

$$\frac{\partial J}{\partial \mathbf{W}} \approx \mathbf{M}_0 \sum_{k=1}^K \mathbf{C}_k \sum_{l=1}^L \mathbf{Z}(l) \sum_{n=1}^N f_k(n) e^{in\omega_0} n^l e^{i\mathbf{k}_n \cdot \mathbf{x}} \quad (4.10)$$

$$\frac{\partial J}{\partial \mathbf{C}_k} \approx \sum_{l=0}^{L-1} \mathbf{Z}(l) \sum_{n=1}^N f_k(n) e^{in\omega_0} n^l e^{i\mathbf{k}_n \cdot \mathbf{x}} \quad (4.11)$$

\mathbf{Z} and ω_0 are defined in chapter 2.

The reconstruction algorithm based on cubic interpolation can also be applied to the reconstruction in parallel MRI.

4.2.2 Initialization

The first step in the reconstruction of PSSPARSE is to find the initial values of $C_k(\mathbf{x})$, $M_0(\mathbf{x})$, $R_2^*(\mathbf{x})$ and $\omega(\mathbf{x})$ for the conjugate-gradients algorithms described above. We use a different mathematical model to find the initial values. We assume that there are K different

M_0 maps — M_1, \dots, M_K — the magnitude. Based on this assumption, y_k is modeled by:

$$y_k(n) = \underbrace{\sum_i M_{k,i} e^{nW_i} e^{i\mathbf{k}_n \cdot \mathbf{x}_i}}_{\hat{y}_k} + \varepsilon_k(n) \quad (4.12)$$

In the cost function (4.4), the unknown \mathbf{z} is defined as $\mathbf{z} = \{\mathbf{M}_k, \mathbf{W}, k = 1, \dots, K\}$.

The gradients are computed by:

$$\frac{\partial J}{\partial \mathbf{M}_k} = \sum_{n=1}^N f_k(n) e^{n\mathbf{W}} e^{i\mathbf{k}_n \cdot \mathbf{x}} \quad (4.13)$$

$$\frac{\partial J}{\partial \mathbf{W}} = \sum_{k=1}^K \mathbf{M}_k \sum_{n=1}^N n f_k(n) e^{n\mathbf{W}} e^{i\mathbf{k}_n \cdot \mathbf{x}} \quad (4.14)$$

With polynomial approximation, the estimated signals and and gradients are evaluated by:

$$y_k(n) \approx e^{jn\omega_0} \sum_{l=0}^{L-1} n^l \sum_{i=1}^K M_{k,i} Z_i(l) e^{i\mathbf{k}_n \cdot \mathbf{x}^{(i)}} \quad (4.15)$$

$$\frac{\partial J}{\partial \mathbf{M}_k} \approx \sum_{l=0}^{L-1} \mathbf{z}(l) \sum_{n=1}^N f_k(n) e^{jn\omega_0} n^l e^{i\mathbf{k}_n \cdot \mathbf{x}} \quad (4.16)$$

$$\frac{\partial J}{\partial \mathbf{W}} \approx \sum_{k=1}^K \mathbf{M}_k \sum_{l=1}^L \mathbf{z}(l) \sum_{n=1}^N f_k(n) e^{jn\omega_0} n^l e^{i\mathbf{k}_n \cdot \mathbf{x}} \quad (4.17)$$

After finding \mathbf{M}_k , we use the root mean square of \mathbf{M}_k as the initial values of \mathbf{M}_0 :

$$\mathbf{M}_0 = \sqrt{\frac{\sum_{k=1}^K |\mathbf{M}_k|^2}{K}} \quad (4.18)$$

and the coil sensitivities are computed by:

$$\mathbf{C}_k = \frac{\mathbf{M}_k}{\mathbf{M}_0}, \quad k = 1, \dots, K \quad (4.19)$$

We also apply the interpolation method to compute the initial conditions. Because of the use of interpolation, the algorithm stated in 4.2.1 is initialized with the interpolation coefficients other than \mathbf{C}_k , \mathbf{M}_k and \mathbf{W} . We use the interpolation coefficients that are associated with the reconstructed \mathbf{M}_k , \mathbf{C}_k and \mathbf{W} to initialize the reconstruction algorithm

4.2.3 Regularization

We use regularization to improve the reconstruction performance. The regularization operation is defined as:

$$R(\mathbf{x}) = \mathbf{H} * \mathbf{x} * \mathbf{H}^T \quad (4.20)$$

where $*$ denotes a convolution operation. The regularization kernel \mathbf{H} is:

$$\mathbf{H} = \begin{bmatrix} 0 & 0 & 0 \\ -1 & 2 & -1 \\ 0 & 0 & 0 \end{bmatrix} \quad (4.21)$$

With regularization terms, the cost function (4.4) is given by:

$$\begin{aligned} J(\mathbf{z}) = & \sum_{k=1}^K \|\mathbf{y}_k - \hat{\mathbf{y}}_k(\mathbf{z})\|^2 \\ & + \alpha \|R(\mathbf{M}_0)\|^2 + \beta \sum_{k=1}^K \|R(\mathbf{C}_k)\|^2 + \gamma_R \|R(\mathbf{R}_2^*)\|^2 + \gamma_I \|R(\boldsymbol{\omega})\|^2 \end{aligned} \quad (4.22)$$

where α , β , γ_R and γ_I are all nonnegative real numbers.

The corresponding gradients ∇J includes terms of ∇R :

$$\frac{1}{2} \nabla \|R(\mathbf{x})\|^2 = \mathbf{A} * \mathbf{x} \quad (4.23)$$

where

$$\mathbf{A} = \begin{bmatrix} 0 & 0 & 1 & 0 & 0 \\ 0 & 0 & -4 & 0 & 0 \\ 1 & -4 & 12 & -4 & 1 \\ 0 & 0 & -4 & 0 & 0 \\ 0 & 0 & 1 & 0 & 0 \end{bmatrix} \quad (4.24)$$

4.3 Simulation

We synthesized the simulation data from the images in Figure 4.1 and 4.2. Eq. (4.3) was used to generate the synthesized data. The image resolution for the synthesis was 1024.

It is assumed that the FOV is 12.8cm. Both x -axis and y -axis are defined on $[-6.4, 6.4]$. Four receiving coils are placed at the four corners of the FOV. The coil sensitivities are described by (4.25).

$$C(x, y) = [(x \pm x_0)^2 + (y \pm y_0)^2]^{-\alpha} \quad (4.25)$$

In the simulation, $x_0 = y_0 = 6.8$ and $\alpha = 1/4$.

The SNR is defined as:

$$\text{SNR} = \frac{\sum_{k=1}^K \|\hat{\mathbf{Y}}_k\|^2}{MN\sigma_\varepsilon^2} \quad (4.26)$$

4.3.1 Interpolation of Coil Sensitivity

In all of the simulations, 128×128 was used as the image resolution. We used $2 \times$ interpolation for the computation of the initial conditions. That is, the coefficients of \mathbf{M}_k and \mathbf{W} were 64×64 . In the joint reconstruction of \mathbf{M}_0 , \mathbf{W} and \mathbf{C}_k , 64×64 resolution was also used for the coefficients of \mathbf{M}_0 and \mathbf{W} . Since the \mathbf{C}_k 's are very spatially smooth, we use

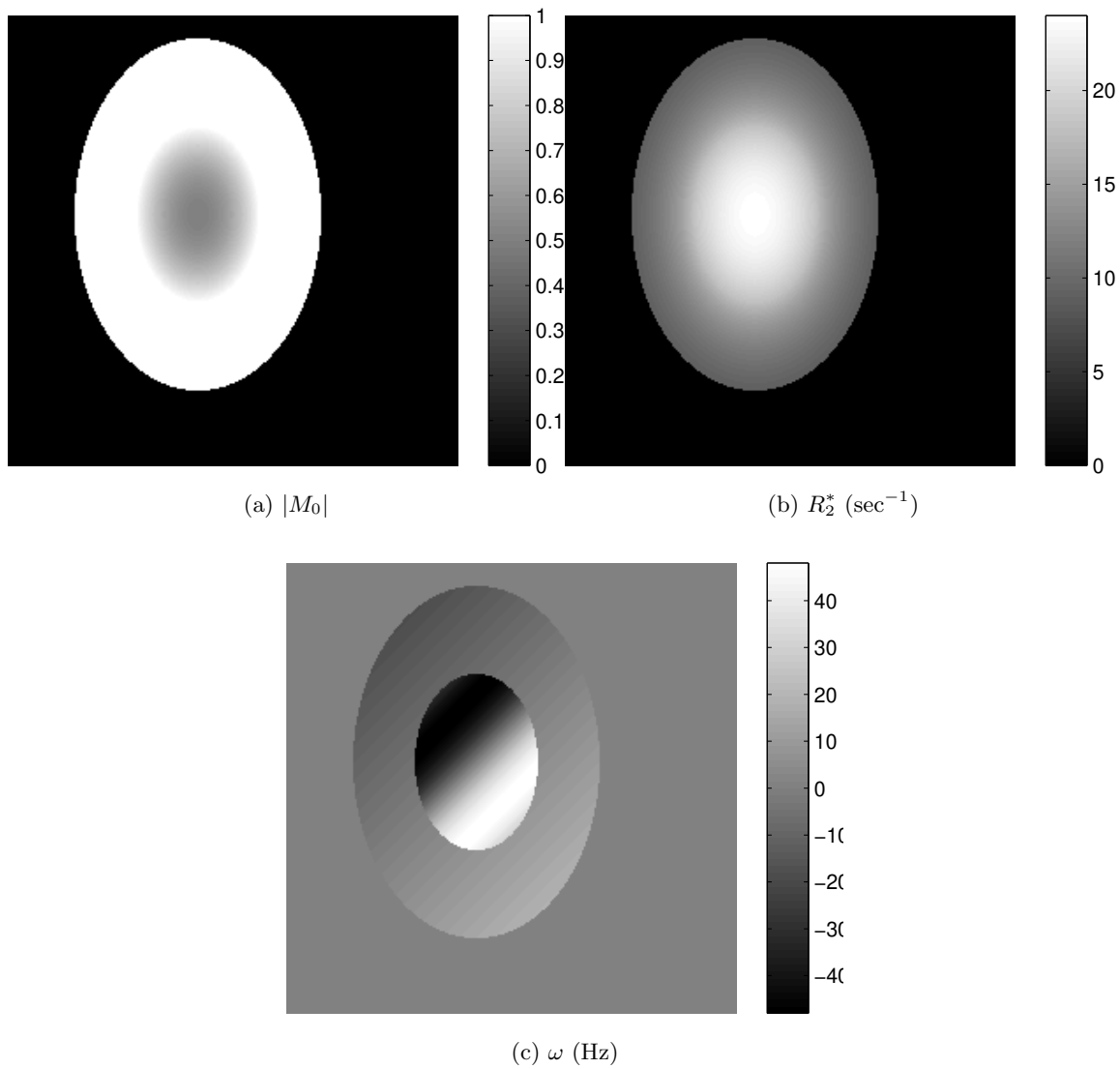


Figure 4.1: The magnitude, decay and field map used to synthesize simulation data. All images are displayed with 256×256 resolution. M_0 is normalized to 1.

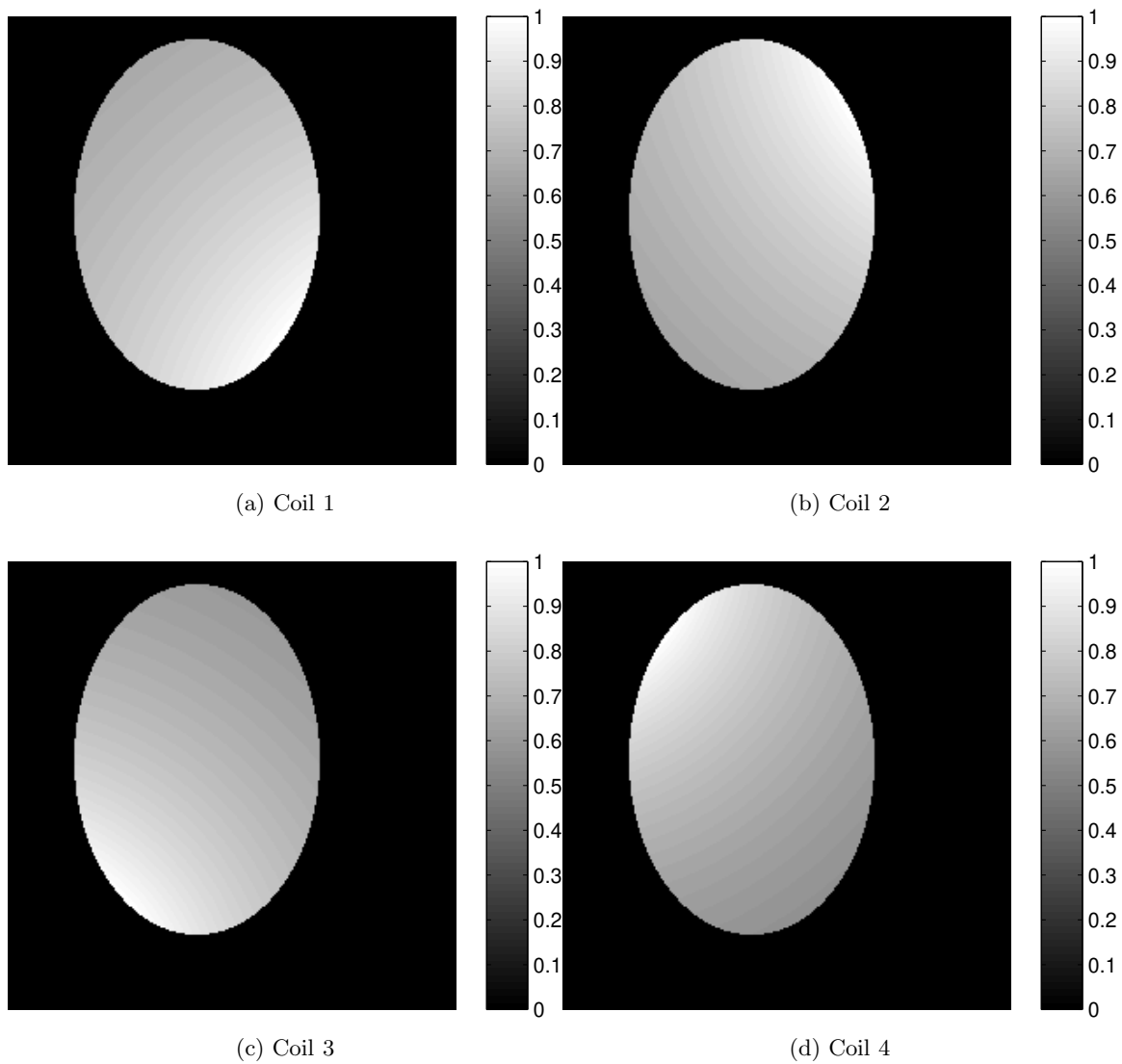


Figure 4.2: The coil sensitivity maps used to synthesize simulation data. All images are displayed with 256×256 resolution. The unconstrained area in which M_0 is zero are displayed with zero. All maps are normalized to 1.

a lower resolution for the coefficients of \mathbf{C}_k 's — a larger interpolation factor. We used the cubic convolution interpolation for all of the estimated parameters. For $I \times$ interpolation, the sampling interval is $h = 1/I$. The 1-D interpolation vector of $I \times$ interpolation is:

$$u(\pm nh), \quad n = 0, \pm h, \dots, \pm(3/h - 1)h \quad (4.27)$$

where $u(x)$ is defined by (2.9).

We experimentally compared the reconstruction accuracies of different interpolation factors of the coil sensitivity in Table 4.1. In this comparison, we used signals with 30 dB SNR.

Table 4.1: NRMSE (%) of Different Coil Sensitivity Interpolations

Interpolation	C_1	C_2	C_3	C_4	M_0	R_2^*	ω
2×	29.2	36.8	36.6	30.3	29.8	14.4	17.9
4×	8.7	8.7	7.5	7.2	28.3	14.4	17.9
8×	6.9	8.3	7.5	6.7	29.5	14.4	17.9
16×	10.7	10.4	6.9	7.2	30.2	14.4	17.9

The reconstructed C_1 from the different interpolation factors are illustrated in Figure 4.3.

4.3.2 Regularized Reconstruction

We applied regularization to this reconstruction. Because the field map ω is not spatially smooth enough, the experiments show that the regularization does not improve the reconstruction accuracy of ω . We empirically selected the regularization parameters α , β and γ_R . Table 4.2 compares the reconstruction performance for different combinations of regularization coefficients. The interpolation factor for the coil sensitivity used here was 8. The interpolation factors of M_0 , R_2^* and ω were all 2. A set of coil sensitivities and images from regularized reconstruction are displayed in Figure 4.6 and 4.7. Table 4.2 shows that the selection of the regularization parameter for one set of variables has little impact on the

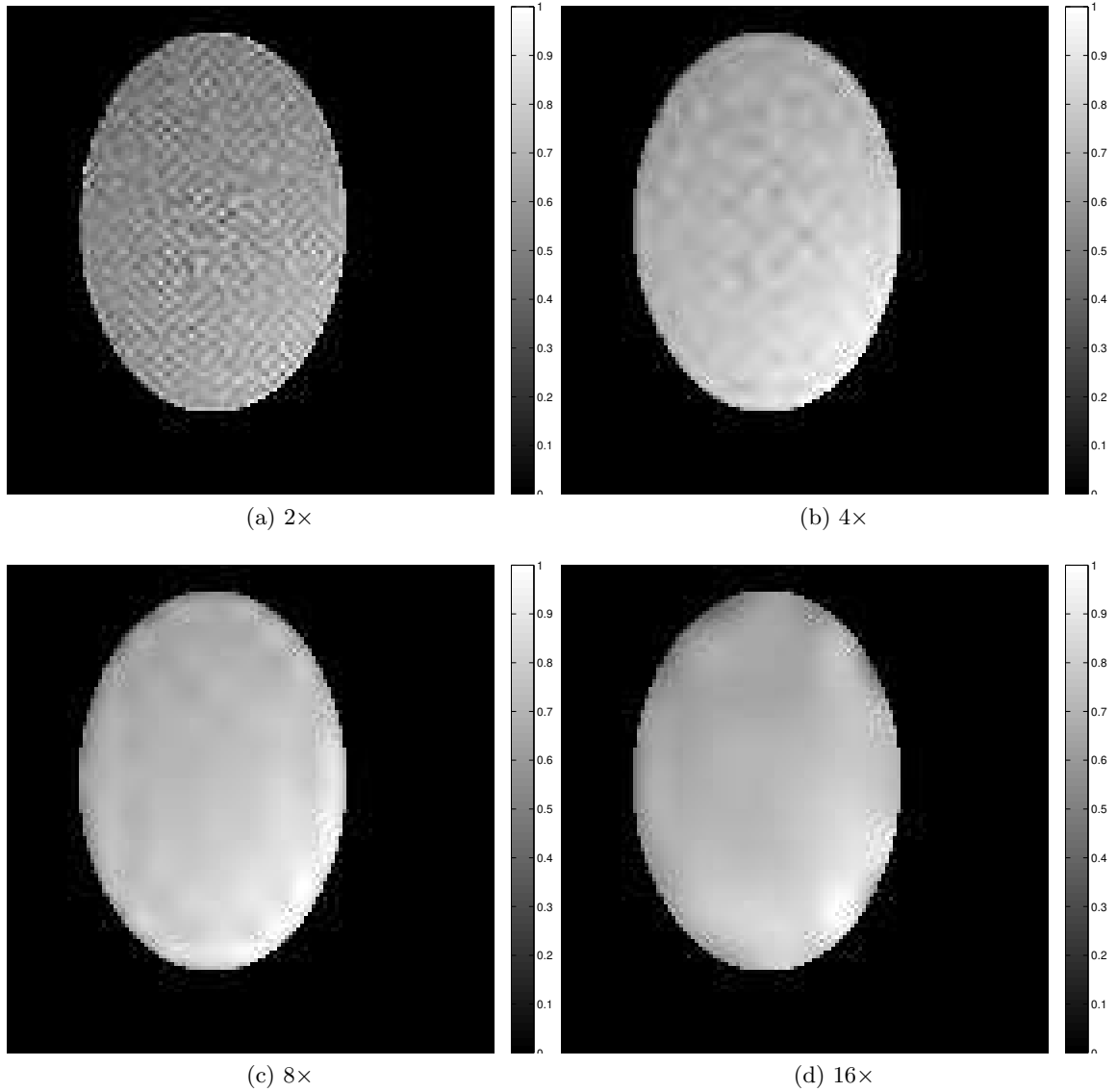


Figure 4.3: The coil sensitivity C_1 reconstructed from different interpolation factors. All images are displayed with 128×128 resolution. The artifacts in the unconstrained area in which M_0 is zero are removed. All maps are normalized to 1. No regularization is used.

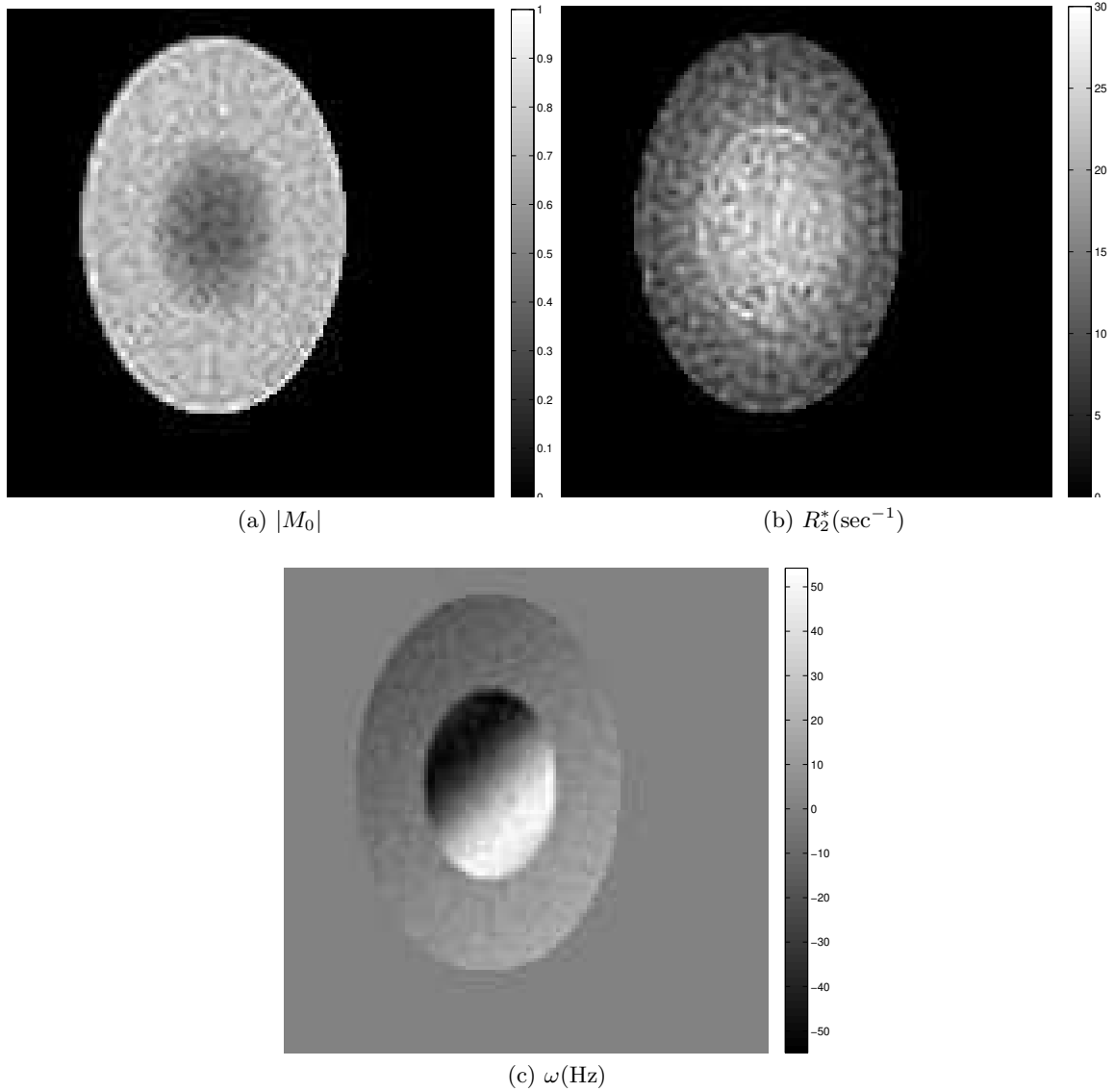


Figure 4.4: The magnitude, decay and field map reconstructed from signals with 30dB SNR. All images are displayed with 128×128 resolution. The artifacts in the unconstrained area in which M_0 is zero are removed. M_0 is normalized to 1. No regularization is used.

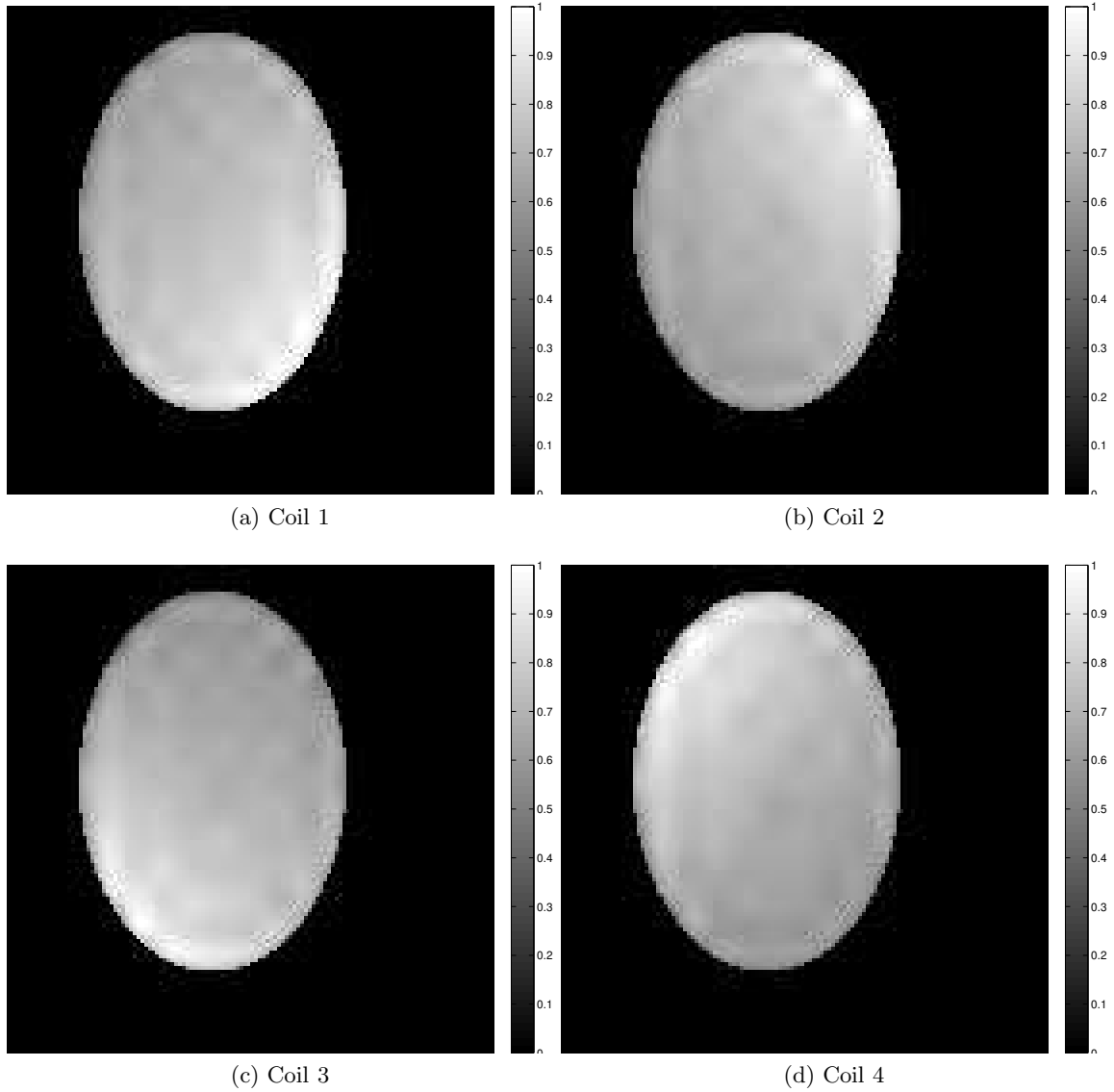


Figure 4.5: The coil sensitivity maps reconstructed from signals with 30dB SNR. All images are displayed with 128×128 resolution. The artifacts in the unconstrained area in which M_0 is zero are removed. All maps are normalized to 1. No regularization is used.

reconstruction accuracy of the other sets of variables. For example, the selection of α , the regularization parameter of M_0 , is almost unrelated to the reconstruction accuracy of R_2^* and ω .

Table 4.2: NRMSE (%) of Different Regularization Coefficients

α	γ_R	β	C_1	C_2	C_3	C_4	M_0	R_2^*	ω
0	0	0	7.0	8.3	7.5	6.7	29.5	14.4	17.9
0	0	1.09×10^6	7.7	7.9	6.9	7.6	29.0	14.4	17.9
0	1.75×10^8	0	8.6	6.8	6.7	9.3	28.7	4.6	17.9
0	1.75×10^8	1.09×10^6	10.6	8.9	8.2	8.5	28.8	5.5	17.9
5.5×10^7	0	0	10.8	8.5	6.4	9.6	13.7	14.4	17.9
5.5×10^7	0	1.09×10^6	9.4	8.4	6.4	9.8	13.6	14.4	17.9
5.5×10^7	1.75×10^8	0	11.5	8.9	6.6	9.5	13.7	4.0	17.9
5.5×10^7	1.75×10^8	1.09×10^6	9.5	8.4	6.5	9.5	13.6	3.9	17.9

4.4 Human Experiment

We applied the reconstruction method to human brain data. A Siemens Tim Trio 3T MRI system was used in this experiment. The system is located at the Department of Neuroscience of the Brown University. The major parameters of this experiment are listed in Table 4.3. The rosette trajectory used in the experiment is plotted in Figure. 4.8.

Table 4.3: Experiment Parameters of Human Experiment

Parameter	Value	Unit
sampling interval (Δt)	5.0	μs
FOV	22.0	cm
readout duration	56.8	ms
magnetic field	3.0	T
trajectory	rosette	-

In the reconstruction, we used the signals from two coils. Since the simulation experiments show that $4\times$ and $8\times$ interpolation for the coil sensitivities give similar results, we

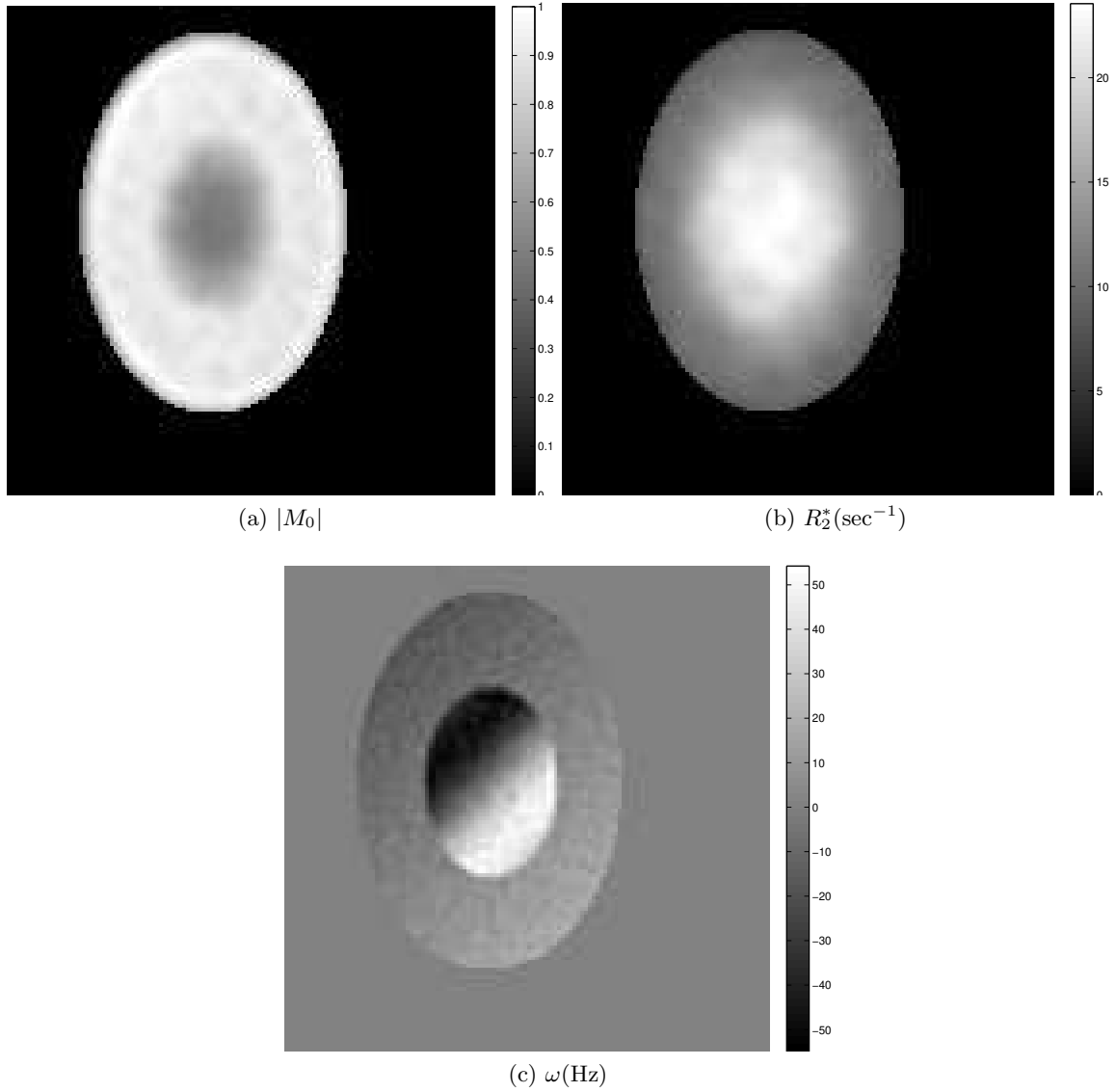


Figure 4.6: The magnitude, decay and field map reconstructed from signals with 30dB SNR. The regularization parameters $\alpha = 5.5 \times 10^7$, $\gamma_R = 1.75 \times 10^8$ and $\gamma_I = 0$. All images are displayed with 128×128 resolution. The artifacts in the unconstrained area in which M_0 is zero are removed. M_0 is normalized to 1.

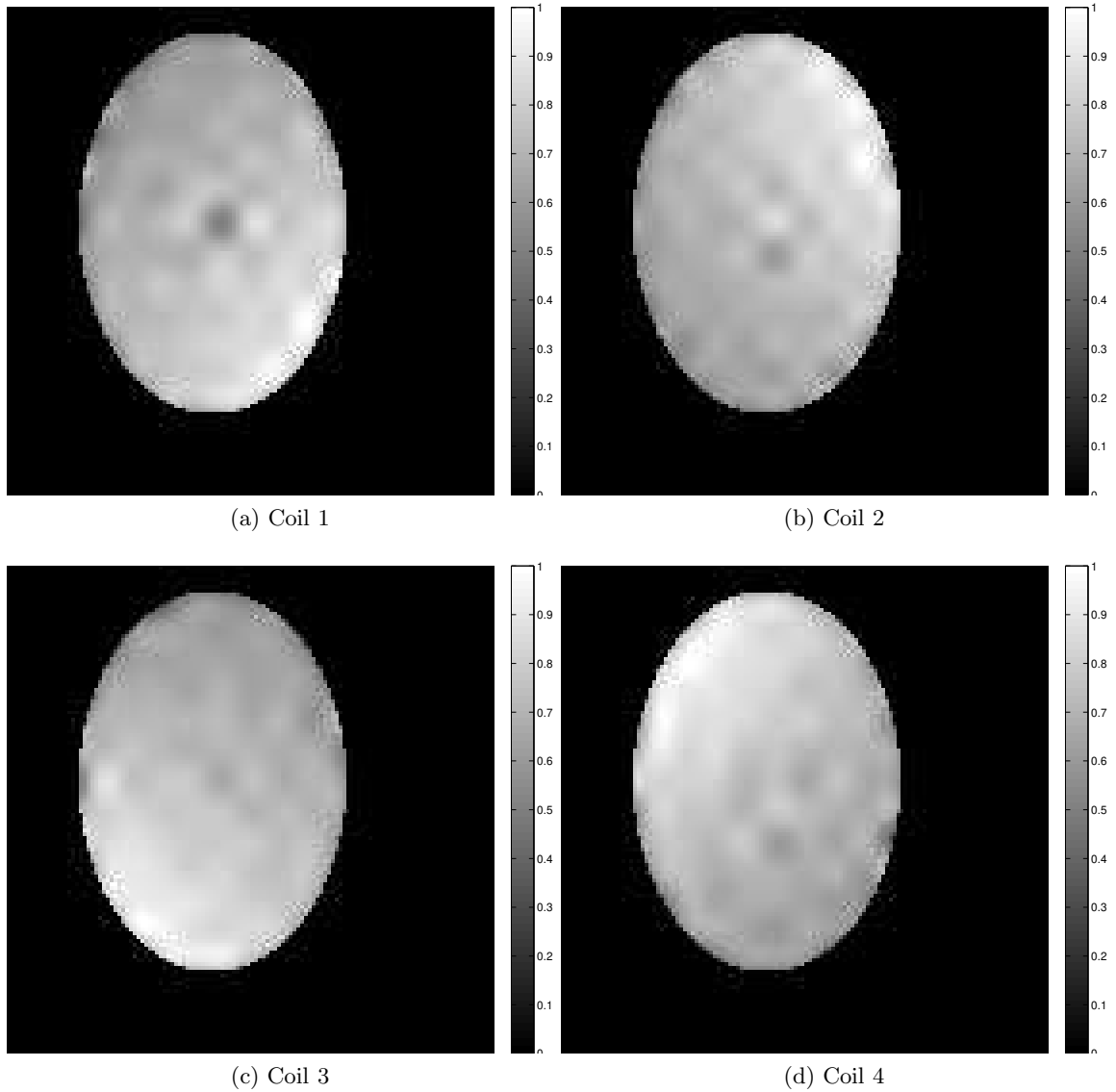


Figure 4.7: The coil sensitivity maps reconstructed from signals with 30dB SNR. The regularization parameters $\alpha = 1.09 \times 10^6$. All images are displayed with 128×128 resolution. The artifacts in the unconstrained area in which M_0 is zero are removed. All maps are normalized to 1.

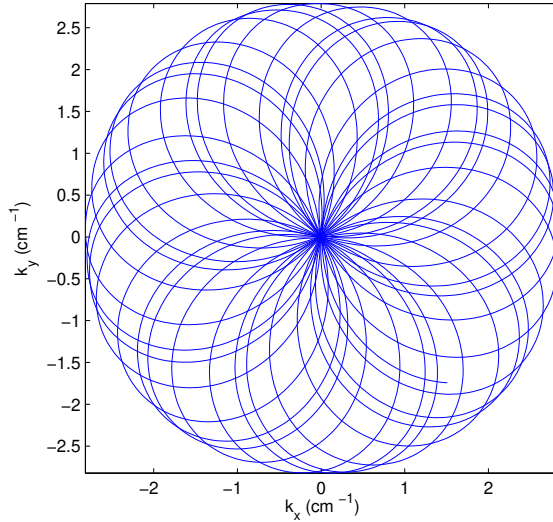


Figure 4.8: Rosette trajectory used in human experiment. Only the first half of the trajectory is plotted.

applied these two levels of interpolation. For both cases, M_0 , R_2^* and ω were reconstructed with $2\times$ interpolation. The recovered images are shown in Figure 4.9 and 4.10.

We also interpolated coil sensitivity with a cubic spline function. The magnitude, decay and field map were still interpolated by a cubic convolution function because of its advantage for the exponential time function demonstrated in Chapter 2. The results are in Figure 4.11 and 4.12.

The reconstructed images show that the proposed algorithm can produce realistic results. The artifacts on the edges of the coil sensitivity maps, R_2^* and ω are caused by the zero or near zero M_0 values at that locations.

$4\times$ and $8\times$ coil sensitivity interpolation reconstructed similar M_0 , R_2^* and ω , but the the coil sensitivity maps from $8\times$ interpolation are better. We see some artifacts at the left upper and lower corners. The artifacts may be caused by the locations of the receiving coils because the two coils were located at the right upper and lower corners. Two more coils at the left upper and lower corners may correct this problem. Another possible reason for the

artifacts is system bias. By tuning the reconstruction parameters, the system bias can be removed.

4.5 Conclusion

In this chapter, we extended the cubic convolution interpolation, quadratic line search, polynomial approximation of the exponential time function and nonuniform FFT from single-coil SS-PARSE to the multiple-coil SS-PARSE.

Because the reconstruction complexity is proportional to the number of receiving coils, the computational speed improvement of the fast approach stated in Chapter 2 is more significant in the reconstruction of the multiple-coil system.

The experiments in our simulations show that regularization can improve the reconstruction performance of some of the parameters. Our simulations show that the frequency map is insensitive to regularization. The best results were from the reconstruction that regularized M_0 , R_2^* and C_k . Because we lack the gold standard of human brain experiment, we did not use regularization for the human experiment.

We applied both cubic convolution interpolation and cubic spline interpolation for the coils sensitivity model. We see similar results for the human experiment. But in our simulation, the spline model can not reach the minimum error using the quadratic line search, so we have to resort to golden section search that takes much longer time. Even though we did not observe this phenomenon in the human experiment, we still believe it is safer to use cubic convolution.

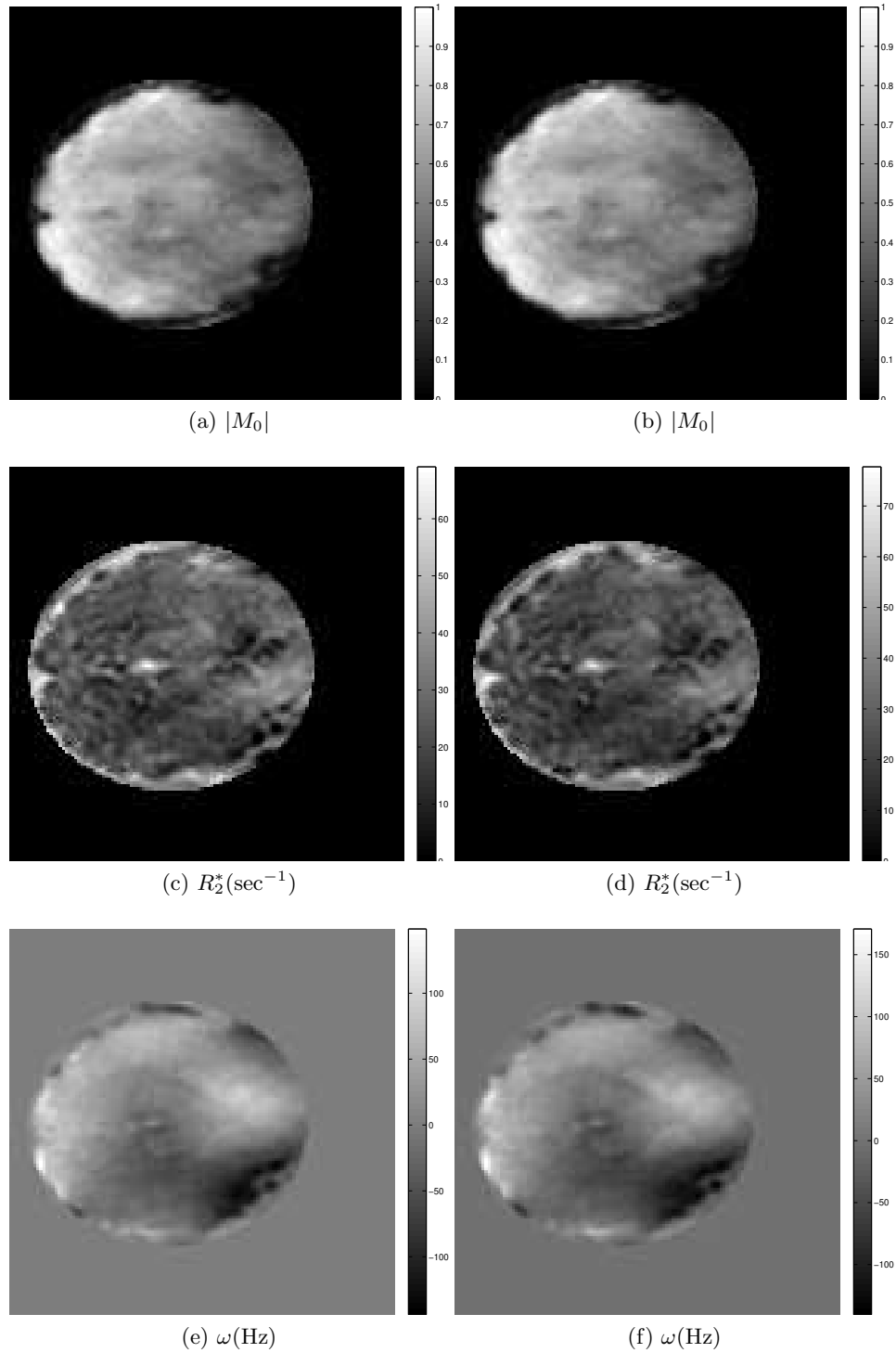


Figure 4.9: The magnitude, decay and field map reconstructed from the human brain experiment. Cubic convolution interpolation was used to model the coil sensitivity. All images are displayed with 128×128 resolution. (a) (c) (e) are from $4\times$ interpolation for coil sensitivity. (b) (d) (f) are from $8\times$ interpolation for coil sensitivity. M_0 is normalized to 1. Most of the artifacts outside of the head were removed. No regularization was used.

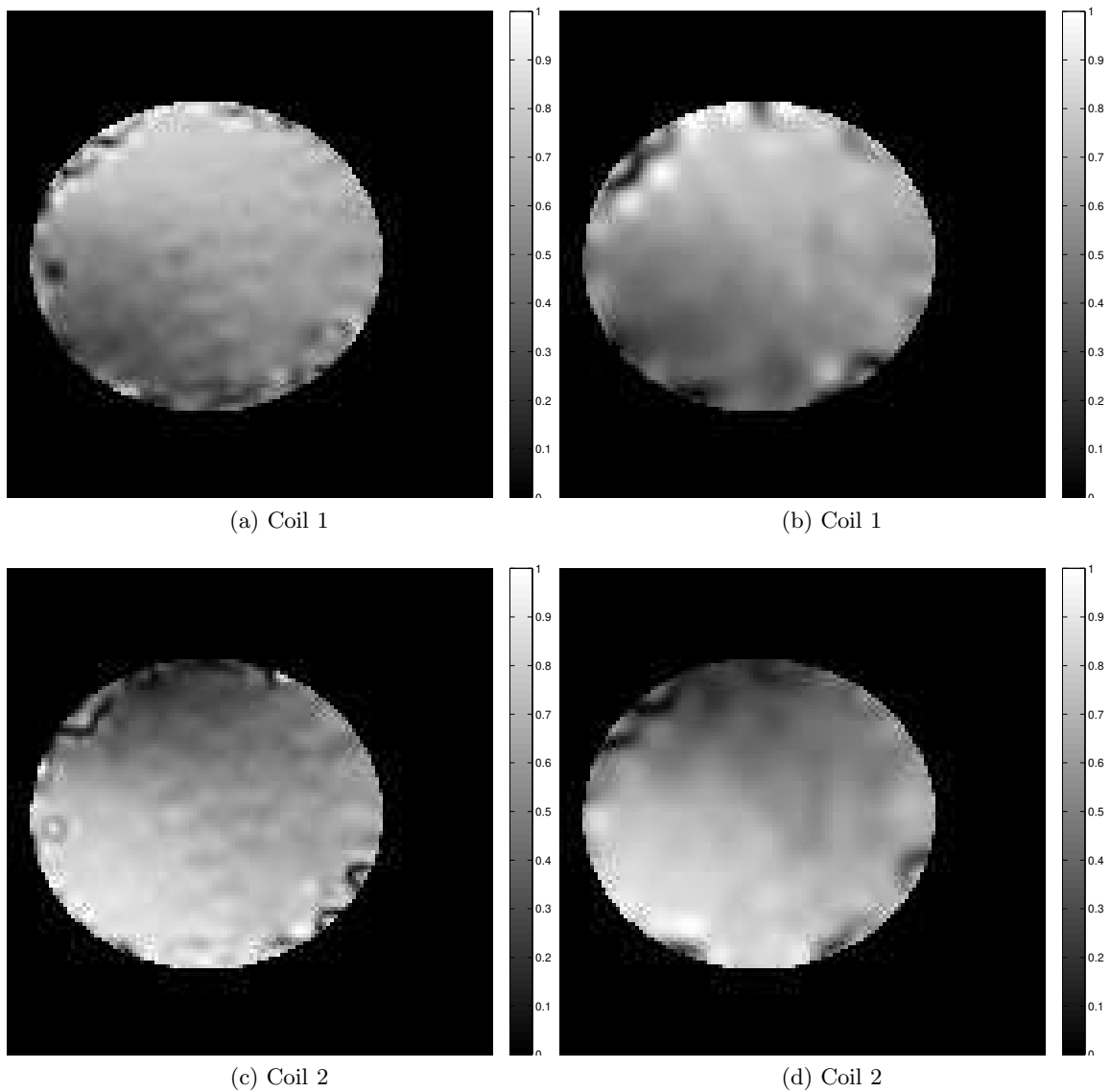


Figure 4.10: The coil sensitivity maps reconstructed from the human brain experiment. Cubic convolution interpolation was used to model the coil sensitivity. All images are displayed with 128×128 resolution. (a) (c) are from $4\times$ interpolation. (b) (d) are from $8\times$ interpolation. Most of the artifacts outside of the head are removed. All maps are normalized to 1. No regularization was used.

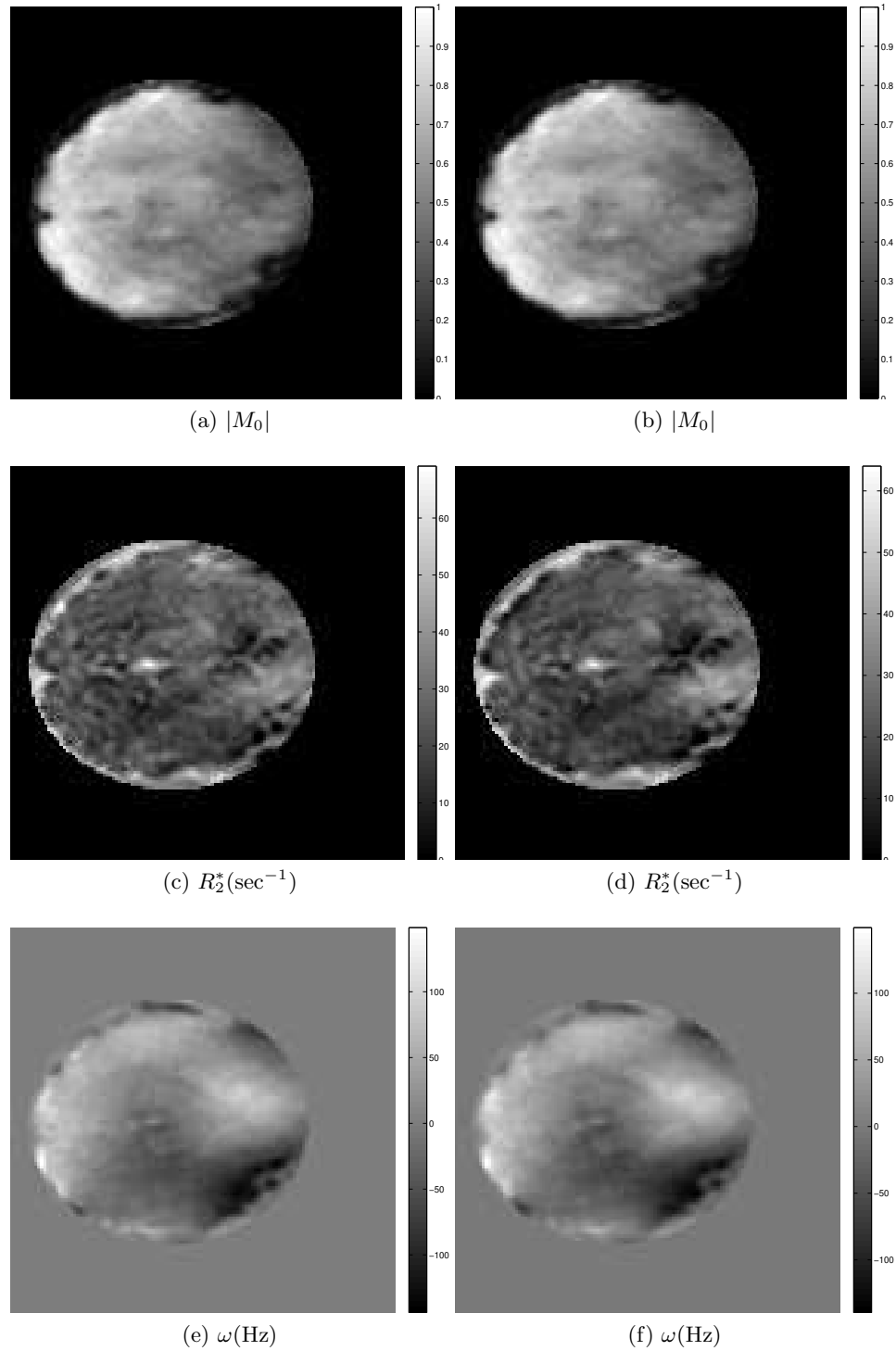


Figure 4.11: The magnitude, decay and field map reconstructed from the human brain experiment. Cubic spline interpolation was used to model the coil sensitivity. All images are displayed with 128×128 resolution. (a) (c) (e) are from $4\times$ interpolation for coil sensitivity. (b) (d) (f) are from $8\times$ interpolation for coil sensitivity. Most of the artifacts outside of the head were removed. M_0 is normalized to 1. No regularization was used.

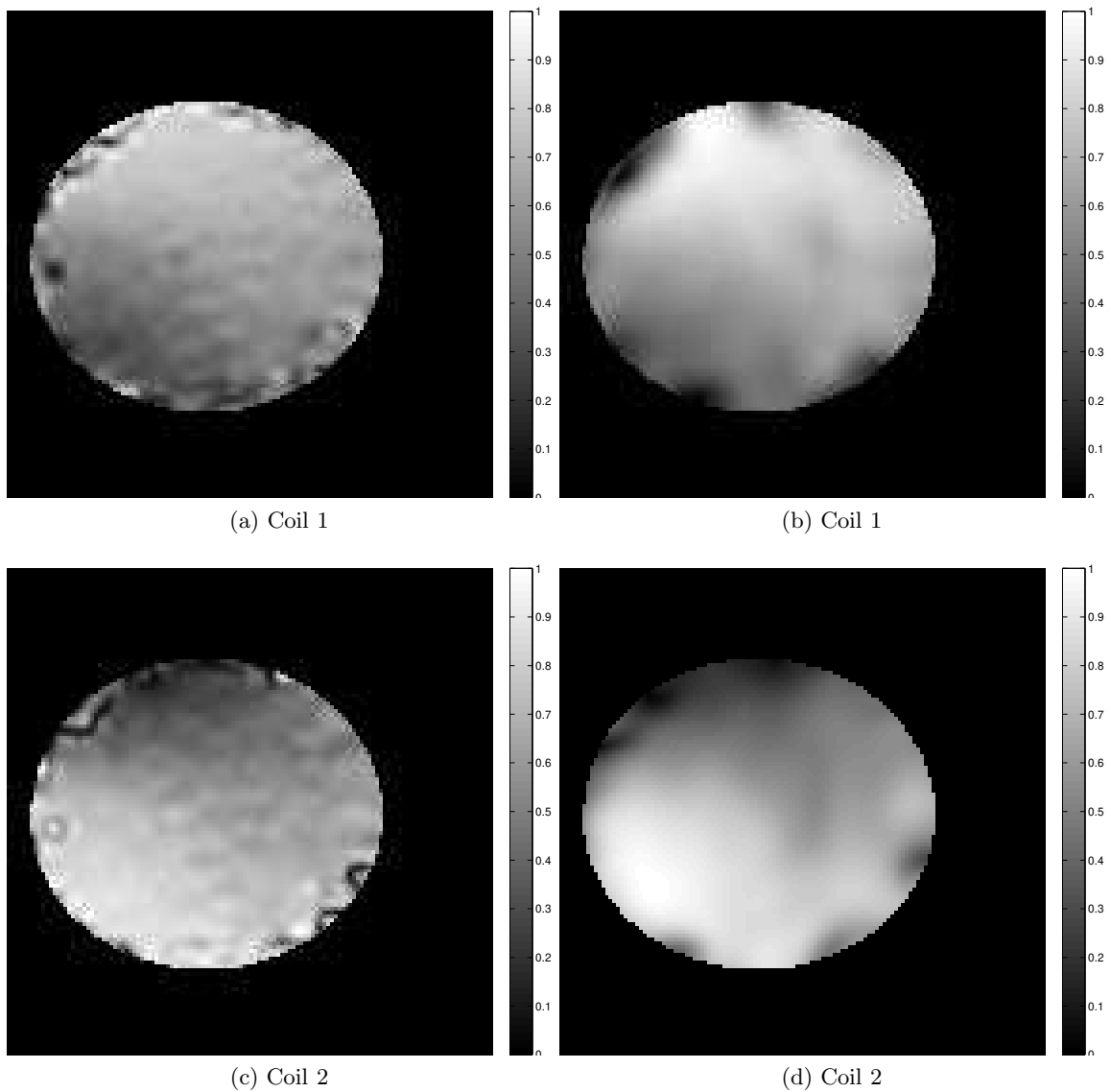


Figure 4.12: The coil sensitivity maps reconstructed from the human brain experiment. Cubic spline interpolation was used to model the coil sensitivity. All images are displayed with 128×128 resolution. (a) (c) are from $4\times$ interpolation. (b) (d) are from $8\times$ interpolation. Most of the artifacts outside of the head were removed. All maps are normalized to 1. No regularization was used.

5.1 Summary of the Contributions of this Thesis

In this thesis, a new approach is suggested for SS-PARSE reconstruction. The major parts of this approach are:

1. The interpolated reconstruction method is proposed. This method can reconstruct higher-resolution images that show higher-frequency features while the reconstruction is still well constrained. A phantom experiment showed that the interpolated reconstruction is much better than the non-interpolated reconstruction in a larger field inhomogeneity environment. This could be also useful for high-field MRI because the field inhomogeneity of high-field MRI is more serious.
2. The cubic convolution interpolator yields significantly less blurred R_2^* than the cubic spline interpolator because of its zero-crossing at neighboring sample locations.
3. The polynomial approximation of the exponential time function was used to linearize the reconstruction. This approximation is convenient for the dynamic estimation of R_2^* and field map because the optimized polynomial coefficients need not be changed for updated R_2^* and field map. Using this approximation, the reconstruction is converted to the form of Fourier transforms so that the FFT can be used.
4. The quadratic approximation of the line search was implemented. This method greatly reduces the computation of the line search.

Motivated by non-Cartesian trajectories used by SS-PARSE, we also improved the nonuniform FFT (NUFFT). The pre-weight scaling factor and interpolation coefficients are two critical issues in the NUFFT. The existing methods first optimize the interpolation, then compute the scaling factor based on the optimized interpolation. We linearized this

problem so that optimal solutions of the scaling factor and interpolation coefficients are simultaneously found. This method improved the precision of the NUFFT.

This framework was extended to parallel imaging. We validated this method with simulated data. We also applied the proposed method to a human brain experiment.

5.2 Future Works

In Chapter 4, we observed that regularization can further improve the reconstruction performance. We empirically choose the regularization parameter and kernel. We need a mathematical method to optimize the parameter and kernel. The generalized cross-validation [42] is a possible candidate for this issue. We tentatively tried this method, but we did not have satisfactory results. We need to refine this work or choose a different method.

The proposed methods were mathematically validated by simulated data. Validation by human and animal experiments is needed. The methods suggested in this dissertation reconstructed realistic images from these experiments, but we do not have a quantitative error analysis because of the lack of “gold standard”. With a gold standard from a human experiment, we would be able to refine some reconstruction parameters.

We tested the cubic convolution and cubic spline interpolations. Other interpolations may be better suited for this problem. With the interpolation, we have a continuous model instead of a discrete model. Because of the insurmountable computation obstacle we can only solve this problem with a higher discrete resolution. A possible future work is to find a continuous reconstruction algorithm that is within the capability of today’s computing technology. The core of this algorithm is still how to deal with the problematic exponential time function.

In the NUFFT, we compute an mN -point FFT. $m = 2$ is the best compromise. Using two scaling factors instead of one may give a better approximation. Optimization of the NUFFT approximation requires the solution of an overdetermined problem. For given set of K frequencies, we have NK equations, but we only have $JK + N$ variables. With two

scaling factors, we may have an additional N variables. More degrees of freedoms could produce a more accurate results.

BIBLIOGRAPHY

- [1] J. Hennig, O. Speck, M. A. Koch, and C. Weiller, “Functional Magnetic Resonance Imaging: A Review of Methodological Aspects and Clinical Applications,” *J Mag. Reson. Imaging*, vol. 18, pp. 1–15, Jul 2003.
- [2] S. Ogawa, T. Lee, A. Nayak, and P. Glynn, “Oxygenation-Sensitive Contrast in Magnetic Resonance Image of Rodent Brain at High Magnetic Fields,” *Mag. Reson. Med.*, vol. 14, no. 1, pp. 68–78, 1990.
- [3] K. Kwong, J. Belliveau, D. Chesler, I. Goldberg, R. Weisskoff, B. Poncelet, D. Kennedy, B. Hoppel, M. Cohen, R. Turner, *et al.*, “Dynamic Magnetic Resonance Imaging of Human Brain Activity During Primary Sensory Stimulation,” *Proceedings of the National Academy of Sciences*, vol. 89, no. 12, pp. 5675–5679, 1992.
- [4] F. Bloch, W. Hansen, and M. Packard, “Nuclear Induction,” *Physical Review*, vol. 70, no. 7-8, pp. 460–474, 1946.
- [5] E. Purcell, H. Torrey, and R. Pound, “Resonance Absorption by Nuclear Magnetic Moments in a Solid,” *Physical Review*, vol. 69, no. 1-2, pp. 37–38, 1946.
- [6] R. Damadian, “Tumor Detection by Nuclear Magnetic Resonance,” *Science*, vol. 171, no. 3976, pp. 1151–1153, 1971.
- [7] P. Lauterbur, “Image Formation by Induced Local Interactions: Examples Employing Nuclear Magnetic Resonance,” *Nature*, vol. 242, no. 5394, pp. 190–191, 1973.
- [8] E. Haacke, R. Brown, M. Thompson, and R. Venkatesan, “Magnetic Resonance Imaging: Physical Principles and Sequence Design,” 1999.
- [9] D. Twieg, “The k-Trajectory Formulation of the NMR Imaging Process with Applications in Analysis and Synthesis of Imaging Methods,” *Medical Physics*, vol. 10, p. 610, 1983.
- [10] A. Elster and J. Burdette, *Questions and Answers in Magnetic Resonance Imaging*. Mosby St. Louis, MO, 2001.
- [11] D. Twieg, “Parsing Local Signal Evolution Directly from A Single-Shot MRI Signal: A New Approach for fMRI,” *Mag. Reson. Med.*, vol. 50, pp. 1043–1052, Nov 2003.
- [12] S. Ljunggren, “A Simple Graphical Representation of Fourier-Based Imaging Methods,” *J Mag. Reson.*, vol. 54, no. 2, pp. 338–343, 1983.

- [13] S. Ogawa, D. Tank, R. Menon, J. Ellermann, S. Kim, H. Merkle, and K. Ugurbil, "Intrinsic Signal Changes Accompanying Sensory Stimulation: Functional Brain Mapping with Magnetic Resonance Imaging," *Proceedings of the National Academy of Sciences*, vol. 89, no. 13, pp. 5951–5955, 1992.
- [14] R. Buxton, *Introduction to Functional Magnetic Resonance Imaging*. Cambridge University Press, 2002.
- [15] R. Menon, S. Ogawa, D. Tank, and K. Ugurbil, "4 Tesla Gradient Recalled-Echo Characteristics of Photic Stimulation-Induced Signal Changes in the Human Primary Visual Cortex," *Mag. Reson. Med.*, vol. 30, no. 3, pp. 380–386, 1993.
- [16] G. Glover, S. Lemieux, M. Dragova, and J. Pauly, "Decomposition of Inflow and Blood Oxygen Level-Dependent (BOLD) Effects with Dual-Echo Spiral Gradient-Recalled Echo (GRE) fMRI," *Mag. Reson. Med.*, vol. 35, no. 3, pp. 299–308, 1996.
- [17] O. Speck and J. Hennig, "Functional Imaging by I_0 - and T_2^* -Parameter Mapping Using Multi-Image EPI," *Mag. Reson. Med.*, vol. 40, no. 2, pp. 243–8, 1998.
- [18] S. Posse, S. Wiese, D. Gembris, K. Mathiak, C. Kessler, M. Grosse-Ruyken, B. Elghahwagi, T. Richards, S. Dager, and V. Kiselev, "Enhancement of BOLD-Contrast Sensitivity by Single-Shot Multi-Echo Functional MR Imaging," *Mag. Reson. Med.*, vol. 42, pp. 87–97, 1999.
- [19] K. S. Nayak and D. G. Nishimura, "Automatic Field Map Generation and Off-Resonance Correction for Projection Reconstruction Imaging," *Mag. Reson. Med.*, vol. 43, pp. 151–154, Jan 2000.
- [20] A. Schulte, O. Speck, C. Oesterle, and J. Hennig, "Separation and Quantification of Perfusion and BOLD Effects by Simultaneous Acquisition of Functional I_0 - and T_2^* -Parameter Maps," *Mag. Reson. Med.*, vol. 45, no. 5, pp. 811–6, 2001.
- [21] B. Sutton, D. Noll, and J. Fessler, "Fast, Iterative Image Reconstruction for MRI in the Presence of Field Inhomogeneities," *Medical Imaging, IEEE Trans. on*, vol. 22, no. 2, pp. 178–188, 2003.
- [22] J. Fessler, S. Lee, V. Olafsson, H. Shi, and D. Noll, "Toeplitz-Based Iterative Image Reconstruction for MRI With Correction for Magnetic Field Inhomogeneity," *Signal Processing, IEEE Trans. on*, vol. 53, pp. 3393–3402, Sept. 2005.
- [23] A. Funai, J. Fessler, D. Yeo, V. Olafsson, and D. Noll, "Regularized Field Map Estimation in MRI," *Medical Imaging, IEEE Trans. on*, vol. 27, pp. 1484–1494, Oct. 2008.
- [24] V. Olafsson, D. Noll, and J. Fessler, "Fast Joint Reconstruction of Dynamic R_2^* and Field Maps in Functional MRI," *Medical Imaging, IEEE Trans. on*, vol. 27, pp. 1177–1188, Sept. 2008.

- [25] T. Knopp, H. Eggers, H. Dahnke, J. Prestin, and J. Senegas, "Iterative Off-Resonance and Signal Decay Estimation and Correction for Multi-Echo MRI," *Medical Imaging, IEEE Trans. on*, vol. 28, pp. 394–404, March 2009.
- [26] H. Nguyen, B. Sutton, R. Morrison Jr, and M. Do, "Joint Estimation and Correction of Geometric Distortions for EPI functional MRI using Harmonic Retrieval," *Medical Imaging, IEEE Trans. on*, vol. 28, pp. 423–434, March 2009.
- [27] T. Harshbarger and D. Twieg, "Iterative Reconstruction of Single-Shot Spiral MRI with Off Resonance," *Medical Imaging, IEEE Trans. on*, vol. 18, pp. 196–205, March 1999.
- [28] E. Chong and S. Zak, *An Introduction to Optimization Theory*. John Wiley & Sons, Inc., 2001.
- [29] M. Unser, "Splines: A Perfect Fit for Signal and Image Processing," *Signal Processing Magazine, IEEE*, vol. 16, pp. 22–38, Nov 1999.
- [30] R. Keys, "Cubic Convolution Interpolation for Digital Image Processing," *Acoustics, Speech, and Signal Processing, IEEE Trans. on*, vol. 29, no. 6, pp. 1153–1160, 1981.
- [31] W. Tang, S. Reeves, and D. Twieg, "Fast Joint Estimation of Local Magnitude, Decay, and Frequency from Single-Shot MRI," in *Proceedings of SPIE*, vol. 6498, p. 649818, SPIE, 2007.
- [32] D. C. Noll, "Multishot Rosette Trajectories for Spectrally Selective MR Imaging," *Medical Imaging, IEEE Trans. on*, vol. 16, pp. 372–377, Aug 1997.
- [33] A. Dutt and V. Rokhlin, "Fast Fourier Transforms for Nonequispaced Data," *SIAM Journal on Scientific Computing*, vol. 14, p. 1368, 1993.
- [34] J. Fessler and B. Sutton, "Nonuniform Fast Fourier Transforms Using Min-Max Interpolation," *Signal Processing, IEEE Trans. on*, vol. 51, pp. 560–574, Feb 2003.
- [35] Q. Liu and N. Nguyen, "An Accurate Algorithm for Nonuniform Fast Fourier Transforms (NUFFT's)," *Microwave and Guided Wave Letters, IEEE*, vol. 8, pp. 18–20, Jan 1998.
- [36] M. Jacob, "Optimized Least-Square Nonuniform Fast Fourier Transform," *Signal Processing, IEEE Transactions on*, vol. 57, pp. 2165–2177, June 2009.
- [37] J. Carlson, "An Algorithm for NMR Imaging Reconstruction Based on Multiple RF Receiver Coils," *J Mag. Reson.*, vol. 74, pp. 376–380, 1987.
- [38] M. Griswold, "Basic Reconstruction Algorithms for Parallel Imaging," *Parallel Imaging in Clinical MR Applications*, p. 19, 2007.
- [39] D. Sodickson and C. McKenzie, "A Generalized Approach to Parallel Magnetic Resonance Imaging," *Medical Physics*, vol. 28, p. 1629, 2001.

- [40] O. Dietrich, “General Advantages of Parallel Imaging,” *Parallel Imaging in Clinical MR Applications*, p. 173, 2007.
- [41] M. Griswold, P. Jakob, M. Nittka, J. Goldfarb, and A. Haase, “Partially Parallel Imaging with Localized Sensitivities(PILS),” *Mag. Reson. Med.*, vol. 44, no. 4, pp. 602–609, 2000.
- [42] S. Reeves and R. Mersereau, “Blur Identification by the Method of Generalized Cross-Validation,” *Image Processing, IEEE Trans. on*, vol. 1, no. 3, pp. 301–311, 1992.

APPENDIX A

DERIVATION OF NRMSE OF NUFFT WITH LINEAR INTERPOLATION

With linear interpolation, $g_l(x)$ on the interval $[x_k, x_{k+1}]$ is represented by:

$$g_l(x) = \frac{g_l(x_{k+1}) - g_l(x_k)}{h} (x - x_k) + g_l(x_k) \quad (\text{A.1})$$

where $h = x_{k+1} - x_k$.

The total error on the interval $[x_k, x_{k+1}]$ is:

$$\begin{aligned} R(n, k) &= \int_{x_k}^{x_{k+1}} \left| e^{i\frac{2\pi n}{N}x} - s_n^{-1} \sum_{l=-\lfloor (J-1)/2 \rfloor}^{\lceil (J-1)/2 \rceil} \left[\frac{g_l(x_{k+1}) - g_l(x_k)}{h} (x - x_k) + g_l(x_k) \right] e^{i\frac{2\pi n}{mN}l} \right|^2 dx \\ &= \int_0^h \left| e^{i\frac{2\pi n}{N}x_k} e^{i\frac{2\pi n}{N}x} - s_n^{-1} \sum_{l=-\lfloor (J-1)/2 \rfloor}^{\lceil (J-1)/2 \rceil} \left[\frac{g_l(x_{k+1}) - g_l(x_k)}{h} x + g_l(x_k) \right] e^{i\frac{2\pi n}{mN}l} \right|^2 dx \end{aligned} \quad (\text{A.2})$$

Let

$$\begin{aligned} A_{nk} &= e^{i\frac{2\pi n}{N}x_k} \\ B_{nk} &= -s_n^{-1} \sum_{l=-\lfloor (J-1)/2 \rfloor}^{\lceil (J-1)/2 \rceil} \frac{g_l(x_{k+1}) - g_l(x_k)}{h} e^{i\frac{2\pi n}{mN}l} \\ C_{nk} &= -s_n^{-1} \sum_{l=-\lfloor (J-1)/2 \rfloor}^{\lceil (J-1)/2 \rceil} g_l(x_k) e^{i\frac{2\pi n}{mN}l} \end{aligned}$$

then,

$$\begin{aligned}
R(n, k) &= \int_0^h \left| A_{nk} e^{i \frac{2\pi n}{N} x} + B_{nk} x + C_{nk} \right|^2 dx \\
&= h + I_1(n, k) + I_2(n, k) + I_3(n, k)
\end{aligned} \tag{A.3}$$

where

$$\begin{aligned}
I_1(n, k) &= 2\text{Re} \left\{ A_{nk} B_{nk}^* \int_0^h x e^{i \frac{2\pi n}{N} x} dx \right\} \\
I_2(n, k) &= 2\text{Re} \left\{ A_{nk} C_{nk}^* \int_0^h e^{i \frac{2\pi n}{N} x} dx \right\} \\
I_3(n, k) &= \frac{1}{3} \|B\|^2 h^3 + \text{Re} \{ B_{nk} C_{nk}^* \} h^2 + \|C\|^2
\end{aligned}$$

For $\alpha \neq 0$,

$$\begin{aligned}
\int_0^h x e^{\alpha x} dx &= \frac{h}{\alpha} e^{\alpha h} - \frac{1}{\alpha^2} (e^{\alpha h} - 1) \\
\int_0^h e^{\alpha x} dx &= \frac{1}{\alpha} (e^{\alpha h} - 1)
\end{aligned}$$